AD A050156

AFAPL-TR-77-47

COHERENT ANTI-STOKES RAMAN SCATTERING OF MOLECULAR GASES

RESEARCH APPLICATIONS DIVISION
SYSTEMS RESEARCH LABORATORIES, INC.
2800 INDIAN RIPPLE ROAD
DAYTON, OHIO 45440

AUGUST 1977

D D C

FEB 17 1978

F

TECHNICAL REPORT AFAPL-TR-77-47
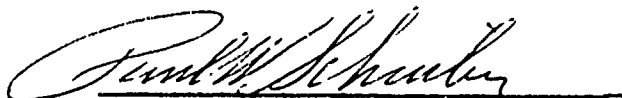Final Report for Period 1 March 1975 — 30 April 1977

AIR FORCE AERO PROPULSION LABORATORY
AIR FORCE WRIGHT AERONAUTICAL LABORATORIES
AIR FORCE SYSTEMS COMMAND
WRIGHT-PATTERSON AIR FORCE BASE, OHIO 45433
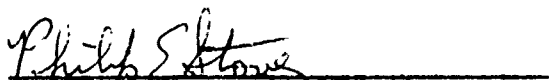
This technical report has been reviewed and is approved for publication.

PAUL W. SCHREIBER
Project Engineer

FOR THE COMMANDER

PHILIP E. STOVER
Chief, High Power Branch

REPORT DOCUMENTATION PAGE	READ INSTRUCTIONS BEFORE COMPLETING FORM

1. REPORT NUMBER	2. GOVT ACCESSION NO.	3. RECIPIENT'S CATALOG NUMBER
AFAPL-TR-77-47		

4. TITLE (and subtitle)	5. TYPE OF REPORT & PERIOD COVERED
COHERENT ANTI-STOKES RAMAN SCATTERING OF MOLECULAR GASES.	Final rept. 1 March 1975 - 30 April 1977
	6. PERFORMING ORG. REPORT NUMBER 6856 Final SRL-6856

7. AUTHOR(s)	8. CONTRACT OR GRANT NUMBER(s)
Won B. Roh	F33615-75-C-1116 (new)

9. PERFORMING ORGANIZATION NAME AND ADDRESS	10. PROGRAM ELEMENT, PROJECT, TASK AREA & WORK UNIT NUMBERS
Systems Research Laboratories, Inc. 2800 Indian Ripple Road Dayton, Ohio 45440	Project 2301 Task S1 Work Unit 62

11. CONTROLLING OFFICE NAME AND ADDRESS	12. REPORT DATE
	Aug 1977
	13. NUMBER OF PAGES 117 106 p.

14. MONITORING AGENCY NAME & ADDRESS(If different from Controlling Office)	15. SECURITY CLASS. (of this report)
Air Force Aero Propulsion Laboratory (AFAPL/PO) Wright-Patterson Air Force Base, OH 45433	UNCLASSIFIED
	15a. DECLASSIFICATION/DOWNGRADING SCHEDULE

16. DISTRIBUTION STATEMENT (of this Report)

Approved for public release; distribution unlimited.

17. DISTRIBUTION STATEMENT (of the abstract entered in Block 20, if different from Report)

18. SUPPLEMENTARY NOTES

19. KEY WORDS (Continue on reverse side if necessary and identify by block number)

Coherent Anti-Stokes Raman Scattering (CARS)
Molecular Gases
Species-Concentration Measurement
Real-Time Temperature Measurement
Application of Ruby and Infrared Dye Lasers
Combustion Diagnostics
Media-Turbulence Effect

20. ABSTRACT (Continue on reverse side if necessary and identify by block number)

An experimental system based upon a single-mode ruby laser and a ruby-pumped dye laser has been developed to investigate coherent anti-Stokes Raman scattering (CARS) of molecular gases. The CARS system is capable of both broad- and narrow-band operation. Theoretical and experimental results obtained using this system for such gases as H_2, HF, CO, N_2, and CH_4 are given. In particular, real-time CARS spectra of these gases have been obtained for rotational temperature estimations and the pressure dependence of integrated CARS intensity has been determined. In addition, the effect

DD FORM 1473 1 JAN 73   EDITION OF 1 NOV 65 IS OBSOLETE

409171

of media turbulence upon laser-beam propagation and upon the CARS process has been investigated. Results of CARS measurements on a laboratory rocket-engine plume are also presented.

FOREWORD

This final report was prepared by the Research Applications Division of Systems Research Laboratories, Inc. (SRL), 2800 Indian Ripple Road, Dayton, Ohio 45440, under Contract No. F33615-75-C-1116, Project 2301, Task S1, Work Unit 62, with Mr. Paul W. Schreiber (AFAPL/POD-2) as Government Project Monitor.

The report describes the results of theoretical and experimental investigations of coherent anti-Stokes Raman scattering of molecular gases during the period 1 March 1975 through 30 April 1977. Dr. Won B. Roh was the Principal Investigator during the entire course of this research, and he is the author of this technical report. The author submitted this report for Air Force review on 8 July 1977.

We wish to acknowledge the cooperation and assistance of the following colleagues during the course of this research: Mr. Carl Meyers who constructed and operated the experimental equipment, Mr. Robert A. Olson who managed the contract during the early stages, and Mrs. Marian Whitaker and Mrs. Sandra Ehlers for their editorial and typographical assistance.

Furthermore, helpful discussions with Mr. Paul Schreiber, Dr. Alan Garscadden and Mr. David Beard of the Air Force Aero Propulsion Laboratory are also gratefully acknowledged.

iii

TABLE OF CONTENTS

TABLE OF CONTENTS (Continued)

LIST OF ILLUSTRATIONS

SECTION I

INTRODUCTION

This report describes the results of theoretical and experimental investigations of the coherent anti-Stokes Raman scattering (CARS) process of molecular gases which were conducted under USAF Contract F33615-75-C-1116.

The objective of this contract was to investigate the CARS process by developing an experimental system and to further explore the possibility of applying the CARS technique to combustion diagnostics for the purpose of making spatially and temporally resolved gas-species-concentration and temperature measurements. Development of new combustion-diagnostic techniques such as CARS is important to the Air Force in connection with its desire for cleaner and more efficient jet engines.

Coherent anti-Stokes Raman scattering is a nonlinear optical mixing process in which a radiation corresponding to the anti-Stokes component of a molecule is generated when two radiation fields emanating from two high-power lasers such as a ruby and a dye laser are simultaneously focused into a medium. This process was first observed [1] more than a decade ago and was used for making measurements of the third-order susceptibility for solids and liquids [2] and for gases [3]. However, the general application of this technique to other areas of scientific endeavor was hampered by a lack of suitable sources of tunable radiation.

Interest in this process was rekindled following the suggestion that the process be used for gas diagnostics [4,5]. The technique was indeed used to probe laboratory flames [6,7] and electric discharges [8]. In addition, cw CARS was first observed in methane using low-power lasers [9], as was rotational CARS in the hydrogen molecule [10]. Potentially useful is the enhancement in CARS conversion efficiency which is achievable in waveguides [11]. With the development of high-power tunable dye lasers, the utility of the technique was greatly enhanced, and its application in other areas such as basic spectroscopy and analytic chemistry is expanding at a rapid rate [12].

As a diagnostic tool, CARS offers a number of attractive features over
other diagnostic techniques. For example, being an optical technique, it
is nonintruding, thus introducing no disturbances into the medium under
investigation. It permits spatially resolved measurements of gas species
concentration and temperature. Although the spatial resolution along the
optical axis is somewhat limited, in transverse directions it is quite high
(typically tens of microns). Furthermore, with the CARS technique truly
real-time measurements of these parameters are possible due to the superior
signal intensity achievable within an extremely short time period (typically
tens of nanoseconds). In comparison with the spontaneous Raman technique,
to which a substant.al portion of the R&D effort on remote diagnostic
techniques has been directed, CARS offers a signal-conversion efficiency
which is superior by several orders of magnitude.

One of the problems associated with the CARS technique is that it
suffers from the interference of the nonresonant background signal. Because
of this interference, the application of CARS to trace analysis is somewhat
limited at the present time. Although several techniques have been proposed
for reducing the interference effect through the manipulation of the
relative polarizations of the laser beams [13] or through manipulation of
double resonance interferences [14,15], these techniques are applicable
only to a limited number of situations and, therefore, they are not practical
for diagnostics application.

In Section II, an extended theory of CARS which includes broad-band
excitation of the CARS process is presented. In addition to such standard
topics as nonlinear polarizations, susceptibility, and the solution of
the coupled-wave equations, an expression for the integrated CARS intensity
of Q-branch lines is derived, whereby the contributions of the resonant
Raman, off-resonant Raman, and pure electronic components to the integrated
intensity are clearly shown.

In Section III, the experimental CARS system developed is described in
detail, and the modes of its operation are discussed. (Readers not interested
in the details of the experimental apparatus may skip this section without
loss of continuity.)

In Section IV, experimental techniques and results are discussed. Included in this discussion are: 1) the single-pulse CARS technique by which real-time measurements of gas temperature were made; 2) the pressure dependence of the integrated CARS intensity for such gases as N_2, CH_4, CO, and H_2; 3) development of a two-wavelength dye laser and the simultaneous detection of two different gas species; 4) effects of media turbulence upon the laser beam propagation and the CARS process; and 5) the results of some preliminary CARS measurements on the plume of a laboratory rocket engine.

In Section V, a summary of the results obtained during this program along with suggestions for possible future research efforts are presented.

SECTION II

THEORY

In this section, the theory of the Coherent Anti-Stokes Raman Scattering Process is developed. The basic approach used parallels that of other investigators [16,17], but the present development contains a significant extension of existing theories as well.

Initially, a general expression for the nonlinear polarization responsible for CARS radiation is derived in terms of third-order susceptibility. This nonlinear polarization is used in Maxwell's equations to generate a set of coupled-wave equations involving the pump, Stokes, and anti-Stokes waves. The wave equations are solved for the coherent anti-Stokes radiation intensity. An explicit expression for the third-order susceptibility responsible for anti-Stokes generation is derived both classically and quantum mechanically. The vibration-rotational structure of the CARS spectra is analyzed, and the effect of linewidth upon integrated CARS intensity is evaluated.

1. NONLINEAR POLARIZATION

The response of a dielectric medium to electromagnetic waves may be characterized by induced polarization, which can be written, quite generally, as [18]

$$P(t) = P^{(1)}(t) + [P^{(2)}(t)...+...P^{(r)}(t) + ...]$$

$$= P^{L}(t) + P^{NL}(t)$$

(1)

where $P^{(1)}(t)$ is linear in the electric field, $P^{(2)}(t)$ is quadratic, and so on. $P^{(1)}(t)$ can be classified as a linear polarization $[P^{L}(t)]$ and all higher-order polarizations as nonlinear $[P^{NL}(t)]$. By invoking the time-invariance principle, Butcher [18] has shown that $P^{(r)}(t)$ can be expressed as

$$P^{(r)}(t) = \int \chi^{(r)}(\omega',\omega'',...\omega^r)E(\omega')E(\omega'')...E(\omega^r)\exp[-i(\omega'+\omega''+...+\omega^r)t]$$

$$d\omega'd\omega''...d\omega^r$$

(2)

4

where $\chi^{(r)}(\omega', \omega'', \ldots \omega^r)$ is the r-th order susceptibility of the medium and $E(\omega)$ is the Fourier component of the electric field $E(t)$ and is defined by

$$E(\omega) = \frac{1}{2\pi} \int E(t) e^{i\omega t} dt$$

and

$$E(t) = \int E(\omega) e^{-i\omega t} d\omega \qquad \qquad (3)$$

The Fourier components of polarization are defined in a similar manner. For the third-order polarization, for example, the Fourier transform of Eq. (2) for $r = 3$ yields the Fourier component of $P^{(3)}(t)$.

$$P^{(3)}(\omega) = \iint \chi^{(3)}(\omega', \omega'', \omega - \omega' - \omega'') E(\omega') E(\omega'') E(\omega - \omega' - \omega'') d\omega' d\omega'' \qquad (4)$$

A number of special cases will now be examined in greater detail. First, let us consider the case of an incident electromagnetic wave consisting of two frequency components, each having a finite bandwidth

$$E(\omega) = E_p(\omega) + E_s(\omega) \qquad (5)$$

where the subscripts p and s refer to the pump and Stokes components, respectively. The reality of $E(t)$ requires that

$$E_p(-\omega) = E_p^*(\omega)$$

$$\qquad (6)$$

and

$$E_s(-\omega) = E_s^*(\omega)$$

The most significant term of the third-order polarization at the anti-Stokes frequency induced by this incident wave can be expressed as

$$P_a^{(3)}(\omega) = \int E_p(\omega') d\omega' \int 3\chi^{(3)}(\omega', \omega'', \omega - \omega' - \omega'') E_p(\omega'') E_s^*(\omega' + \omega'' - \omega) d\omega'' \qquad (7)$$

where subscript a was used to signify the polarization component at the anti-Stokes frequency.

5

In particular, if the pump wave is monochromatic, the expression is simplified considerably, yielding

$$P_a^{(3)}(\omega) = 3\chi^{(3)}(\omega_p,\omega_p, \omega-2\omega_p)|E_{po}|^2 E_s^*(2\omega_p-\omega) \qquad (8)$$

or, in a more recognizable notation,

$$P_a^{(3)}(\omega_a+\delta) = 3\chi^{(3)}(\omega_p,\omega_p,-\omega_s+\delta)|E_{po}|^2 E_s^*(\omega_s-\delta) \qquad (9)$$

where ω_a is the center frequency of the anti-Stokes and is given by $2\omega_p-\omega_s$, E_{po} is the amplitude of the pump, and δ is a small frequency variation from ω_s, an arbitrarily chosen center frequency of the Stokes wave. This is an important result since Eq. (9) establishes a one-to-one correspondence between each spectral component of the Stokes wave and that of the anti-Stokes polarization. Furthermore, if both the pump and the Stokes components are monochromatic at ω_p and ω_s, respectively, then the polarization becomes even simpler, yielding

$$P_a^{(3)}(\omega_a) = 3\chi^{(3)}(\omega_p,\omega_p,-\omega_s)|E_{po}|^2 E_s^*(\omega_s) \qquad (10)$$

which is the expression obtained by other investigators [2,17].

The polarization represented by Eq. (9) is the coupling term responsible for the generation of coherent anti-Stokes Raman radiation in the presence of a monochromatic pump and a broad-band Stokes beam. Polarizations at the pump and the Stokes frequencies obtained in a similar manner are

$$P_p^{(3)}(\omega_p) = \int 3\chi^{(3)}(\omega_p,\omega',-\omega')E_{po}E_s(\omega')E_s^*(\omega')d\omega' \qquad (11)$$

and

$$P_s^{(3)}(-\omega_s+\delta) = 3\chi^{(3)}(\omega_p,-\omega_p,-\omega_s+\delta)|E_{po}|^2 E_s^*(\omega_s-\delta) \qquad (12)$$

where only the most significant term was retained for each polarization component.

2. GENERATION OF THE ANTI-STOKES WAVE

The propagation of electromagnetic waves is governed by Maxwell's equations, which for a lossless, nonmagnetic homogeneous medium can be written (in Gaussian units) as

$$\left(\nabla^2 - \frac{n^2}{c^2} \frac{\partial^2}{\partial t^2}\right) E(t) = \frac{4\pi}{c^2} \frac{\partial^2}{\partial t^2} P^{NL}(t) \tag{13}$$

where n is the linear refractive index of the medium $\left(= \sqrt{1+4\pi\chi^{(1)}}\right)$ and $P^{NL}(t)$ is the induced nonlinear polarization defined in Eq. (1).

Introduction of the Fourier transform defined in Eq. (3) to Eq. (13) yields Maxwell's equations in the frequency domain

$$\left(\nabla^2 + \frac{n^2\omega^2}{c^2}\right) E(\omega) = - \frac{4\pi\omega^2}{c^2} P^{NL}(\omega) \tag{14}$$

In the discussions to follow, the incident waves are assumed to consist of a plane monochromatic pump beam at ω_p and a Stokes wave of finite bandwidth centered at ω_s, all traveling along the x-axis. Equation (14) then can be broken up into the following three coupled-wave equations involving the pump, the Stokes and the anti-Stokes components:

$$\left(\frac{\partial^2}{\partial x^2} + \frac{n_a^2 \omega_a^2}{c^2}\right) E_a(\omega_a+\delta) = - \frac{4\pi\omega_a^2}{c^2} P_a^{(3)}(\omega_a+\delta) \tag{15a}$$

$$\left(\frac{\partial^2}{\partial x^2} + \frac{n_p^2\omega_p^2}{c^2}\right) E_p(\omega_p) = - \frac{4\pi\omega_p^2}{c^2} P_p^{(3)}(\omega_p) \tag{15b}$$

$$\left(\frac{\partial^2}{\partial x^2} + \frac{n_s^2 \omega^2}{c^2}\right) E_s^*(\omega_s-\delta) = - \frac{4\pi\omega_s^2}{c^2} P_s^{(3)}(-\omega_s+\delta) \tag{15c}$$

where $P_a^{(3)}$, $P_p^{(3)}$, and $P_s^{(3)}$ are given by Eqs. (9), (11), and (12), respectively.

Since the polarizations contain products of electric-field amplitudes, these equations form a set of coupled equations which cannot be solved in closed form without some simplifying assumptions. A common approach to this type of problem is to assume a "weak interaction" whereby the pump depletion through the interaction is neglected. Moreover, in the case of CARS, the change in the Stokes component can also be neglected as long $\varepsilon E_a \ll E_s$; therefore, the anti-Stokes wave equation (15a) can be solved by itself in such cases.

Assume a solution of the form

$$E_a(\omega) = A_a(\omega) e^{ik_a x} \tag{16}$$

for the anti-Stokes and similarly for the pump and the Stokes waves, where the plane-wave nature of $E_a(\omega)$ is explicitly shown. Substitution of Eq. (16) into Eq. (15a) along with the assumption of the "slowly varying amplitude," i.e.,

$$\frac{\partial^2 A_a}{\partial x^2} \ll k_a \frac{\partial A_a}{\partial x} \quad ,$$

yields

$$\frac{\partial A_a}{\partial x}(\omega_a + \delta) = \frac{2\pi i \omega_a}{n_a c} \, 3\chi^{(3)}(\omega_p, \omega_p, -\omega_s + \delta)|A_{po}|^2 A_s^*(\omega_s - \delta) e^{i\Delta k x} \tag{17}$$

where Δk is the phase mismatch given by

$$\Delta k = 2k_p(\omega_p) - k_s(\omega_s - \delta) - k_a(\omega_a + \delta) \tag{18}$$

where $k_p(\omega_p)$ $(= n_p \omega_p / c)$, k_s and k_a are the propagation constants for the pump, Stokes and anti-Stokes waves, respectively. Equation (17) can be integrated easily to yield

$$A_a(\omega_a + \delta) = \frac{2\pi i \omega_a}{n_a c} \int 3\chi^{(3)}(\omega_p, \omega_p, -\omega_s + \delta)|A_{po}|^2 A_s^*(\omega_s - \delta) e^{i\Delta k x} dx \tag{19}$$

8

The intensity of this anti-Stokes wave is

$$I_a(\omega_a+\delta) = \frac{n_a^2}{2\pi} \frac{c}{n_a} \left| A_a(\omega_a+\delta)\right|^2 \tag{20}$$

$$= \left(\frac{4\pi^2\omega_a}{n_a^2 c^2}\right)^2 I_p^2 I_s(\omega_s-\delta) \left|3\chi^{(3)}(\omega_p,\omega_p,-\omega_s+\delta)\right|^2 L^2 \left[\frac{\sin\left(\frac{\Delta kL}{2}\right)}{\frac{\Delta kL}{2}}\right]^2$$

where L is the interaction length. In terms of coherence length, L_c, this becomes

$$I_a(\omega_a+\delta) = \left(\frac{4\pi^2\omega_a}{n_a^2 c^2}\right)^2 I_p^2 I_s(\omega_s-\delta) \left|3\chi^{(3)}(\omega_p,\omega_p,-\omega_s+\delta)\right|^2$$

$$\cdot 2\left(\frac{L_c}{\pi}\right)^2 \left[1-\cos\left(\pi\,\frac{L}{L_c}\right)\right] \tag{21}$$

where $L_c = \frac{\pi}{\Delta k}$. This equation shows the sinusoidal dependence of intensity upon interaction length, with the first maximum occurring at $L = L_c$. For the case of phase-matched interaction, as is approximately the case for colinear beams interacting in gases, the intensity becomes

$$I_a(\omega_a+\delta) = \left(\frac{4\pi^2\omega_a}{n_a^2 c^2}\right)^2 I_p^2 I_s(\omega_s-\delta) \left|3\chi^{(3)}(\omega_p,\omega_p,-\omega_s+\delta)\right|^2 L^2 \tag{22}$$

In the case of focused Gaussian beams, which more closely represent practical laser beams, an extension of equation (22) is possible. Since the CARS intensity is proportional to the cube of the laser-power density, the CARS generation can be approximated to occur within a focal volume defined rather arbitrarily by a cylinder having the radius of the beam-spot size (w_o = 1.22λf/d) and the length of the confocal parameter ($b = 2\pi w_o^2/\lambda$). Since the intensity is P/S (where P is the power and S is the cross-sectional area of the beam spot), Eq. (22) becomes

$$P_a(\omega_a+\delta) = \left(\frac{4\pi\omega_p\omega_a}{n_a^2 c}\right)^2 \left|3\chi^{(3)}(\omega_p,\omega_p,-\omega_s+\delta)\right|^2 P_p^2 P_s(-\omega_s+\delta) \tag{23}$$

9

An interesting consequence of this simple calculation is that the total anti-Stokes power generated by focused Gaussian beams is independent of the focal length of the lens used to focus the beams. However, it has been shown that the anti-Stokes power decreases slightly as the focal length of the lens is increased, when a more rigorous treatment of the Gaussian waves within the focal zone is made [16].

3. SUSCEPTIBILITY

In this subsection an explicit expression for the third-order suscepti-bility which contributes directly to anti-Stokes generation will be derived. A number of different approaches may be taken in order to obtain the susceptibility. A review of these various approaches has been given by DeWitt, et al. [17]. In this report, a classical approach based upon the polarizability theory of Placzek [19] and a quantum-mechanical approach based upon a time-dependent perturbation technique are presented.

A. Classical Susceptibility

The interaction energy between a molecular medium and electromagnetic waves propagating through the medium can be written as

$$H_I = - \frac{1}{2} P \cdot E = - \frac{1}{2} N (\alpha_c + \frac{\partial \alpha}{\partial q} q) E \cdot E \qquad (24)$$

where N is the molecular number density and α is the molecular polarizability which may be expanded in a power series in normal coordinates. E is given by

$$E = E_p e^{i(k_p x - \omega_p t)} + E_s e^{i(k_s x - \omega_s t)} + c \cdot c \qquad (25)$$

where (as before) subscripts p and s refer to the pump and Stokes components, respectively. The nonlinear polarization responsible for CARS is given by

$$P^{NL} = - \frac{\partial H_I}{\partial E} = N \frac{\partial \alpha}{\partial q} q E \qquad (26)$$

and the molecular driving force is

$$F_{mol} = - \frac{1}{N} \frac{\partial H_I}{\partial q} = \frac{1}{2} \frac{\partial \alpha}{\partial q} E^2 \qquad (27)$$

10

The molecular vibration driven by this force is

$$\frac{\partial^2 q}{\partial t^2} + \Gamma \frac{\partial q}{\partial t} + \omega_v^2 q = \frac{F_{mol}}{m} = \frac{1}{2m} \frac{\partial \alpha}{\partial q} E^2 \qquad (28)$$

where ω_v and m are the natural vibration frequency and the reduced mass of the molecules, respectively, and Γ is the damping constant of the vibration. Substitution of a solution of the form

$$q = Q \exp \left\{ i[(k_p - k_s)x - (\omega_p - \omega_s)t] \right\} + c.c. \qquad (29)$$

into Eq. (28) yields

$$q = \frac{1}{2m} \frac{\partial \alpha}{\partial q} 2E_p E_s^* \frac{1}{\omega_v^2 - (\omega_p - \omega_s)^2 - i(\omega_p - \omega_s)\Gamma} \exp \left\{ i[(k_p - k_s)x - (\omega_p - \omega_s)t] \right\}$$
$$+ c.c. \qquad (30)$$

Substitution of Eq. (30), in turn, into Eq. (26) gives, for the anti-Stokes frequency component,

$$P^{NL}_{(2\omega_p - \omega_s)} = \frac{N}{2m} \left(\frac{\partial \alpha}{\partial q}\right)^2 2E_p^2 E_s^* \frac{1}{\omega_v^2 - (\omega_p - \omega_s)^2 - i(\omega_p - \omega_s)\Gamma} e^{i(2k_p - k_s)x} \qquad (31)$$

$$\equiv 3\chi^{(3)} E_p^2 E_s^* e^{i(2k_p - k_s)x}$$

where

$$\chi^{(3)} = \frac{N}{3m} \left(\frac{\partial \alpha}{\partial q}\right)^2 \frac{1}{\omega_v^2 - (\omega_p - \omega_s)^2 - i(\omega_p - \omega_s)\Gamma} \qquad (32)$$

Since the Raman differential cross section is related to the polarizability by [20],

$$\left(\frac{d\alpha}{d\Omega}\right)_v = \frac{\omega_s^4}{c^4} |<v| \frac{\partial \alpha}{\partial q} q |v+1>|^2 \qquad (33)$$

11

$$= \frac{\omega_s^4}{c^4} \frac{\hbar}{2m\omega_v} \left| \frac{\partial \alpha}{\partial q} \right|^2 (v+1)$$

which yields

$$\left(\frac{\partial \alpha}{\partial q} \right)^2 = \frac{c^4}{\omega_s^4} \frac{2m\omega_v}{\hbar(v+1)} \left(\frac{d\sigma}{d\Omega} \right)_v$$

$$= \frac{c^4}{\omega_s^4} \frac{2m\omega_v}{\hbar} \left(\frac{d\sigma}{d\Omega} \right)_o$$

(34)

where

$$\left(\frac{d\sigma}{d\Omega} \right)_v = (v+1) \left(\frac{d\sigma}{d\Omega} \right)_o$$

(35)

Thus,

$$\chi^{(3)} = \frac{2Nc^4}{3\hbar\omega_s^4} \left(\frac{d\sigma}{d\Omega} \right)_o \frac{\omega_v}{\omega_v^2 - \omega^2 - i\omega\Gamma}$$

(36)

where $\omega = \omega_p - \omega_s$. It is important to note that in the above derivation the differential cross section for the ground vibrational state enters the susceptibility expression for all vibrational levels and, therefore, the susceptibility is independent of the vibrational quantum number. This point has thus far been overlooked by all investigators, the erroneous statement having been made that the CARS susceptibility is proportional to (v+1) through the differential cross section when, in fact, the factor (v+1) drops out of the expression when the cross section for the ground vibrational state is used. In light of this error, the estimates of vibrational temperatures for a flame [6] and for an electrical discharge [8] should be revised accordingly.

B. Quantum-Mechanical Susceptibility

The susceptibility responsible for the generation of anti-Stokes radiation can also be derived quantum mechanically using the third-order

12

time-dependent perturbation calculation of the density operator. For the
purpose of this derivation, it is sufficient to begin with a general formula
obtained by Butcher [18]

$$
\chi^{(3)}_{\mu\alpha\beta\gamma}(\omega_1,\omega_2,\omega_3) = -S \; \frac{N}{6\hbar^3} \; \sum_{abcd} \rho^o_{aa} \left[\frac{R^{\mu}_{ab} R^{\alpha}_{bc} R^{\beta}_{cd} R^{\gamma}_{da}}{(\omega_{ab}+\omega_1+\omega_2+\omega_3)(\omega_{ac}+\omega_2+\omega_3)(\omega_{ad}+\omega_3)} \right.
$$

$$
+ \frac{R^{\alpha}_{ab} R^{\mu}_{bc} R^{\beta}_{cd} R^{\gamma}_{da}}{(\omega_{ab}-\omega_1)(\omega_{ac}+\omega_2+\omega_2)(\omega_{ad}+\omega_3)}
$$

$$
+ \frac{R^{\alpha}_{ab} R^{\beta}_{bc} R^{\mu}_{cd} R^{\gamma}_{da}}{(\omega_{ab}-\omega_1)(\omega_{ac}-\omega_1-\omega_2)(\omega_{ad}+\omega_3)} \tag{37}
$$

$$
+ \left. \frac{R^{\alpha}_{ab} R^{\beta}_{bc} R^{\gamma}_{cd} R^{\mu}_{da}}{(\omega_{ab}-\omega_1)(\omega_{ac}-\omega_1-\omega_2)(\omega_{ad}-\omega_1-\omega_2-\omega_3)} \right]
$$

where N is the total molecular number density; a, b, c, and d denote the
states of the molecular system; ρ^o_{aa} is the unperturbed density matrix
element for state a; R^{μ}_{ab} is the μ-component of the matrix element of the
dipole moment between states a and b; ω_{ab} is the energy difference between
states a and b in circular frequency units; and S is the symmetrizing
operator by which the expression which follows it is to be summed over all
six possible permutations of the pairs $\alpha\omega_1$, $\beta\omega_2$, and $\gamma\omega_3$.

For the CARS process ω_p, ω_p and $-\omega_s$ should be substituted for ω_1, ω_2, and
ω_3, respectively. In addition, the molecular system is assumed to be in its
ground state where the energy is taken to be zero--i.e., $\omega_a = 0$. Then $\omega_{ab} =$
$-\omega_b$, $\omega_{ac} = -\omega_c$, and $\omega_{ad} = -\omega_d$. When these substitutions are made into Eq. (37)
and the symmetrizing operation is carried out, the equation yields altogether
24 terms, only eight of which contain a resonant denominator involving the
difference frequency of the pump and the Stokes ($\omega = \omega_p - \omega_s$) components. Since
the other terms are nonresonant in ω, they will be collected together in
a term γ^E which signifies the electronic nature of the contribution to the

susceptibility. (It should be pointed out that terms in χ^E have a resonant denominator in frequencies such as ω_p, ω_s, ω_{as}, and $2\omega_p$.) Thus,

$$\chi^{(3)}_{\mu\alpha\beta\gamma}(\omega_p,\omega_p,-\omega_s) = \chi^E + \frac{N}{6\hbar^3} \sum_{b,c,d} \frac{1}{(\omega_c-\omega)}\left[\frac{1}{(\omega_b-\omega_{as})} \left\{ \frac{A}{(\omega_d+\omega_s)} + \frac{B}{(\omega_d-\omega_p)} \right\} \right.$$

$$\left. + \frac{1}{(\omega_b+\omega_p)} \left\{ \frac{C}{(\omega_d+\omega_s)} + \frac{D}{(\omega_d-\omega_p)} \right\} \right]$$

(38)

where $\omega_{as} = 2\omega_p-\omega_s$,

$$A = R^\mu_{ab}R^\alpha_{bc}R^\beta_{cd}R^\gamma_{da} + R^\mu_{ab}R^\beta_{bc}R^\alpha_{cd}R^\gamma_{da},$$

$$B = R^\mu_{ab}R^\alpha_{bc}R^\gamma_{cd}R^\beta_{da} + R^\mu_{ab}R^\beta_{bc}R^\gamma_{cd}R^\alpha_{da},$$

$$C = R^\alpha_{ab}R^\mu_{bc}R^\beta_{cd}R^\gamma_{da} + R^\beta_{ab}R^\mu_{bc}R^\alpha_{cd}R^\gamma_{da},$$

and $$D = R^\alpha_{ab}R^\mu_{bc}R^\gamma_{cd}R^\beta_{da} + R^\beta_{ab}R^\mu_{bc}R^\gamma_{cd}R^\alpha_{da}.$$

Now, a molecular system is assumed where the intermediate state consists of a group of vibration-rotational levels, one of which is in resonance with ω. Then, the summation over the intermediate state c can be divided into two parts—one involving the resonant intermediate state (which will be denoted by J) and the other involving all the off-resonant intermediate states—to yield

$$\chi^{(3)}_{\mu\alpha\beta\gamma}(\omega_p,\omega_p,-\omega_s) = \chi^E + \frac{N}{6\hbar^3}\left[\frac{1}{\omega_J-\omega} + \sum_{c\neq J} \frac{1}{\omega_c-\omega} \right] \sum_{b,d}\left[\frac{1}{\omega_b-\omega_{as}} \right.$$

$$\left. \left\{ \frac{A}{\omega_d+\omega_s} + \frac{B}{\omega_d-\omega_p} \right\} + \frac{1}{\omega_b+\omega_p} \left\{ \frac{C}{\omega_d+\omega_s} + \frac{D}{\omega_d-\omega_p} \right\} \right]$$

$$\equiv \chi^E + \chi^{RR} + \chi^{OR}$$

(39)

14

where χ^{RR} and χ^{OR} are the resonant and off-resonant Raman components, respectively, of the susceptibility. χ^{OR} together with χ^E makes up χ^{NR} or the nonresonant susceptibility.

Since in most molecular systems, the denominators involving the vibrational frequencies are roughly an order of magnitude smaller than those involving electronic frequencies--as long as no electronic resonances are present--the vibrational contribution (off-resonant) is far greater than the electronic contribution (i.e., $\chi^{OR} \gg \chi^E$). This is especially true for a CARS system employing visible and infrared lasers as the source of the pump radiation. It can be seen easily that resonances at ω_{as} and ω_p will help enhance the resonant CARS susceptibility but will also enhance both electronic and off-resonant components, the degree of relative enhancement depending upon the relative magnitude of the products of dipole moments in the numerator. For this reason, it would be advantageous to utilize any electronic resonances and two-photon absorption in addition to the vibrational resonance if a higher CARS conversion efficiency is desired. If trace detection of a sample molecular species is the objective of the measurement, however, one can still take advantage of electronic-resonance (but not two-photon absorption) enhancement, provided the electronic-resonance frequency of the sample gas does not lie near that of an absorption or emission frequency of the host gas.

4. ROTATIONAL STRUCTURE

The susceptibility, as given in Eq. (36), was calculated, ignoring the rotational motion of the molecules. If the molecules are distributed in a number of vibration-rotation levels, the sum over all the populated vibration-rotation levels must be taken. In addition, the molecular number density should be replaced by the difference in the population density between the levels connected by the scattering process [21]

$$\chi^{(3)} = \sum_J \frac{2N\Delta_J c^4}{3\hbar\omega_s^4} \left(\frac{d\sigma}{d\Omega}\right)_0 \frac{\omega_J}{\omega_J^2 - \omega^2 - i\omega\Gamma_J} \tag{40}$$

15

where
$$N\Delta_J = N_{v,J} - N_{v+1,J} \qquad (41)$$

and g_I a nuclear-spin degeneracy. From Eqs. (40) and (23), the following explicit formula relating the spectral power of individual vibration-rotation lines can be obtained:

$$P_a(v,J) = \left(\frac{8\pi N\omega_p\omega_a c^4}{3\hbar\omega_s^4 Q}\right)^2 \left(\frac{d\sigma}{d\Omega}\right)_o^2 \left[\frac{(2J+1)g_I}{\Gamma_J}\right]^2 \exp\left[-\frac{2hc}{k}\left(\frac{G(v)}{T_v}+\frac{F_v(J)}{T_r}\right)\right]$$
$$\cdot P_p^2 P_s \qquad (42)$$

where Q is the state sum (or partition function); k is Boltzmann's constant; v and J are the vibrational and rotational quantum numbers, respectively; $G(v)$ and $F_v(J)$ are the vibrational and rotational term values, respectively; and T_v and T_r are the vibrational and rotational temperatures, respectively. This equation forms the basis for the analyses of the CARS spectra. It should be pointed out that in deriving this equation, it was assumed that the off-resonant contributions from other vibration-rotational levels are negligibly small and that $N_{v,J} \gg N_{v+1,J}$. In situations where this condition does not hold--such as for the excited vibrational states of a molecule in a plasma--one must use a more rigorous expression which can be obtained from Eq. (40).

5. INTEGRATED INTENSITY

A real-time measurement of gas-species concentration and temperature in a random medium such as a combustion flame and a jet-engine exhaust requires that data acquisition be completed within a time period which is short compared to the period characteristic of media turbulence. Since the period characteristic of most turbulent media is in a µsec to msec regime, a CARS system based upon a spectral-scanning technique does not permit real-time diagnostics of such media. However, a CARS system which operates in the single-pulse mode (such as that to be described in subsequent sections) allows time-resolved gas diagnostics of the media. Basically, the single-pulse technique is based upon broad-band Stokes excitation of a molecular medium in conjunction with a single-mode (monochromatic) pump for simultaneous

generation of an entire Q-branch of an anti-Stokes radiation during a single laser pulse lasting ~ 20 nsec. The generated anti-Stokes radiation can be dispersed in a spectrograph and its spectrum recorded on an optical multichannel analyzer for subsequent spectral analyses. Alternatively, the anti-Stokes radiation can be detected, through a set of filters, by means of a photomultiplier which permits integrated intensity measurement of the entire Q-branch. The latter detection method is more convenient for gas-species-concentration measurements, whereas the former is better suited to gas-temperature measurements.

In order to calculate the integrated intensity of anti-Stokes lines, integration of Eq. (23) over frequency is required, which yields

$$I_t = \left(\frac{4\pi\omega_p\omega_a}{n_a^2 c} \right)^2 \int_0^\infty \left| 3\chi^{(3)}(\omega) \right|^2 P_p^2 \, P_s(\omega-\omega_p) \, d\omega \tag{43}$$

If the Stokes component is assumed to have a uniform spectral power density in the region of the anti-Stokes components--an assumption which is justified as long as the linewidth of the Stokes component is much greater than that of the Q-branch anti-Stokes lines--then the spectral power densities of the incident radiation can be taken outside the integral, leaving only the square modulus of the susceptibility in the integral:

$$I_t = \left(\frac{12\pi\omega_p\omega_a}{n_a^2 c} \right)^2 P_p^2 \, P_s \int_0^\infty \left| \chi^{(3)}(\omega) \right|^2 \, d\omega \tag{44}$$

The susceptibility can be broken up into the following three components--the resonant, off-resonant, and pure electronic--as was shown in Eq. (39):

$$\chi^{(3)} = \chi^{RR} + \chi^{OR} + \chi^E$$

with

$$\chi^{RR} = \sum_J \chi_J^{RR} = \sum_J K_J \frac{1}{\omega_J - \omega - i\Gamma} \tag{45}$$

17

and

$$\chi^{OR} = \sum_K \chi_K^{OR} = \sum_K K_K \frac{1}{\omega_K - \omega - i\Gamma}$$

where the subscripts J and K denote the molecular states of the resonant and off-resonant species, respectively. The constant K represents all frequency-insensitive factors including the nonresonant denominators in Eq. (39). In fact, invocation of equivalence of the classical and quantum-mechanical susceptibilities yields an explicit expression for K_J:

$$K_J = \frac{N\Delta_J c^4}{3\hbar\omega_s^4} \left(\frac{d\sigma}{d\Omega}\right)_0 \tag{46}$$

and similarly for K_K. Substitution of Eq. (45) into Eq. (44) yields the following self- and cross-product terms involving the resonant, off-resonant, and electronic components of susceptibility

$$\int_0^\infty |\chi^{(3)}|^2 \, d\omega = \int_0^\infty |\sum_J \chi_J^{RR} + \sum_K \chi_K^{OR} + \chi^E|^2 \, d\omega$$

$$= \int_0^\infty \{\sum_J |\chi_J^{RR}|^2 + 2\text{Re}[\sum_{J \neq J'} \sum (\chi_J^{RR})^* \chi_{J'}^{RR} + \sum_J \sum_K (\chi_J^{RR})^* \chi_K^{OR}$$

$$+ \sum_J \chi_J^{RR} \chi^E] + |\sum_K \chi_K^{OR} + \chi^E|^2 \} \, d\omega \tag{47}$$

The integral of these terms can be evaluated one by one using the contour integration technique. For example, the first term, representing the rotational sum of the resonant lines, becomes

$$\int_0^\infty \sum_J |\chi_J^{RR}|^2 \, d\omega = \sum_J K_J^2 \int_0^\infty \frac{d\omega}{(\omega_J - \omega)^2 + \Gamma^2} = \sum_J K_J^2 \frac{\pi}{\Gamma} \tag{48}$$

18

The second term, representing the interference between different resonant lines, yields

$$2\mathrm{Re} \sum_{J\neq J'} \int_0^{\infty} (\chi_J^{RR})^* \; \chi_{J'}^{RR} \; d\omega = \sum_{J\neq J'} \; 2K_J K_{J'} \int_0^{\infty} \frac{(\omega_J - \omega)(\omega_{J'} - \omega) + \Gamma^2}{[(\omega_J - \omega)^2 + \Gamma^2][(\omega_{J'} - \omega)^2 + \Gamma^2]} \; d\omega$$

$$= \sum_{J\neq J'} \frac{K_J K_{J'}}{(\omega_J - \omega_{J'})^2 + 4\Gamma^2} \; 8\pi\Gamma \tag{49}$$

Similarly, the third term representing the interference between the resonant and off-resonant Raman components becomes

$$2\mathrm{Re} \sum_J \sum_K \int_0^{\infty} (\chi_J^{RR})^* \; \chi_K^{OR} \; d\omega = \sum_J \sum_K \frac{K_J K_K 8\pi\Gamma}{(\omega_J - \omega_K)^2} \tag{50}$$

where the frequency difference between the resonant and off-resonant lines was assumed to be much larger than Γ.

The fourth term which is the interference between the resonant component and pure electronic component which has no such resonances (and can thus be assumed to be real) makes no contribution to the integrated intensity. The last term represents a constant nonresonant contribution from all off-resonant and electronic components.

It can be seen easily that the first two terms are proportional to the square of the number density of the resonant molecular species and that the third term is proportional to the product of the number densities of the resonant and off-resonant species. Thus, the integrated intensity can be written quite generally, as

$$I_t = K_1 \left\{ p_r^2 \left[\frac{F(T)}{\Gamma} + \sum_{J\neq J'} \frac{\Gamma G_{JJ'}(T)}{(\omega_J - \omega_{J'})^2 + 4\Gamma^2} \right] + p_r p_{or} \left[\sum_J \sum_K \frac{\Gamma H_{JK}(T)}{(\omega_J - \omega_K)^2} \right] + K_2 \right\} \tag{51}$$

where K_1 and K_2 are constants, p_r and p_{or} are the partial pressures of the resonant and off-resonant species, respectively, and $F(T)$, $G_{JJ'}(T)$, and $H_{JK}(T)$ are functions involving the products of the thermal-distribution functions of the molecular species in the medium.

A close examination of the interference term—the second term in the first square bracket in Eq. (51)—reveals that in situations where its contribution is important, it is inversely proportional to Γ as is the first term, and therefore, the two terms can be combined by means of a new parameter Γ_{eff}. Moreover, if the nonresonant contributions are negligible as in the case of a pure resonant gas, then the integrated intensity can be written as

$$I_t = K_1 p_r^2 \; \frac{F(T)}{\Gamma_{eff}} \tag{52}$$

with

$$\Gamma_{eff} = \frac{\Gamma}{1 + \dfrac{1}{F(T)} \displaystyle\sum_{J \neq J'} \sum \dfrac{\Gamma G_{JJ'}(T)}{(\omega_J - \omega_{J'})^2 + 4\Gamma^2}} \tag{53}$$

It should be noted that the effective linewidth, Γ_{eff}, approaches Γ as the interference between the resonant lines decreases. The decrease in the interference would result, for example, when the resonant lines are separated farther apart. Thus, for well-resolved Q-branch lines such as in the H_2 molecule, the effective linewidth would, in fact, correspond to the actual linewidth of the anti-Stokes lines. These results will be used for interpreting the experimental results in later sections.

EXPERIMENTAL APPARATUS

1. CARS SYSTEM

The CARS system is shown schematically in Fig. 1 and pictorially in Fig. 2. The system consists of a ruby-laser oscillator/amplifier, a ruby-pumped infrared dye laser, monochromator/detector and electronics, and various optics for guiding the beams. In addition, a He-Ne laser beam is used for aligning the entire CARS system. Basically, the system operates as follows: A single-mode (transverse and longitudinal) ruby-laser beam emanating from the ruby oscillator is amplified in the ruby amplifier and split into two parts by means of a beamsplitter (BS1). One part (70%) of the ruby beam is weakly focused and directed into the dye cell slightly off-axis for pumping the dye laser. The dye-laser output is combined colinearly with the other part of the ruby-laser beam and focused into a reference cell containing a nonresonant gas under high pressure (typically 30 atm). This colinear superposition of the pump and the Stokes beams satisfies the phase-matching conditions for coherent generation of anti-Stokes radiation in gases. The anti-Stokes signal generated in the reference cell is removed from the laser beams by means of a dichroic mirror (DM2), and the laser beams are refocused into the sample cell containing the medium under investigation. The ruby-laser power and pulse shape are continuously monitored by means of a PIN diode detector and a transient digitizer (Tektronix R 7912)(not shown in the figure). The anti-Stokes signals--one from the reference cell and the other from the sample cell--are detected and processed using either of the detection systems shown in Fig. 3, depending upon the particular experimental requirements. These two detection systems are discussed below along with their respective modes of operation.

1) <u>Broad-Band Operation</u>. This mode of operation is used for instantaneous generation of an entire Q-branch spectrum of anti-Stokes radiation in a light molecule such as H_2 and HF using a single laser pulse. For this
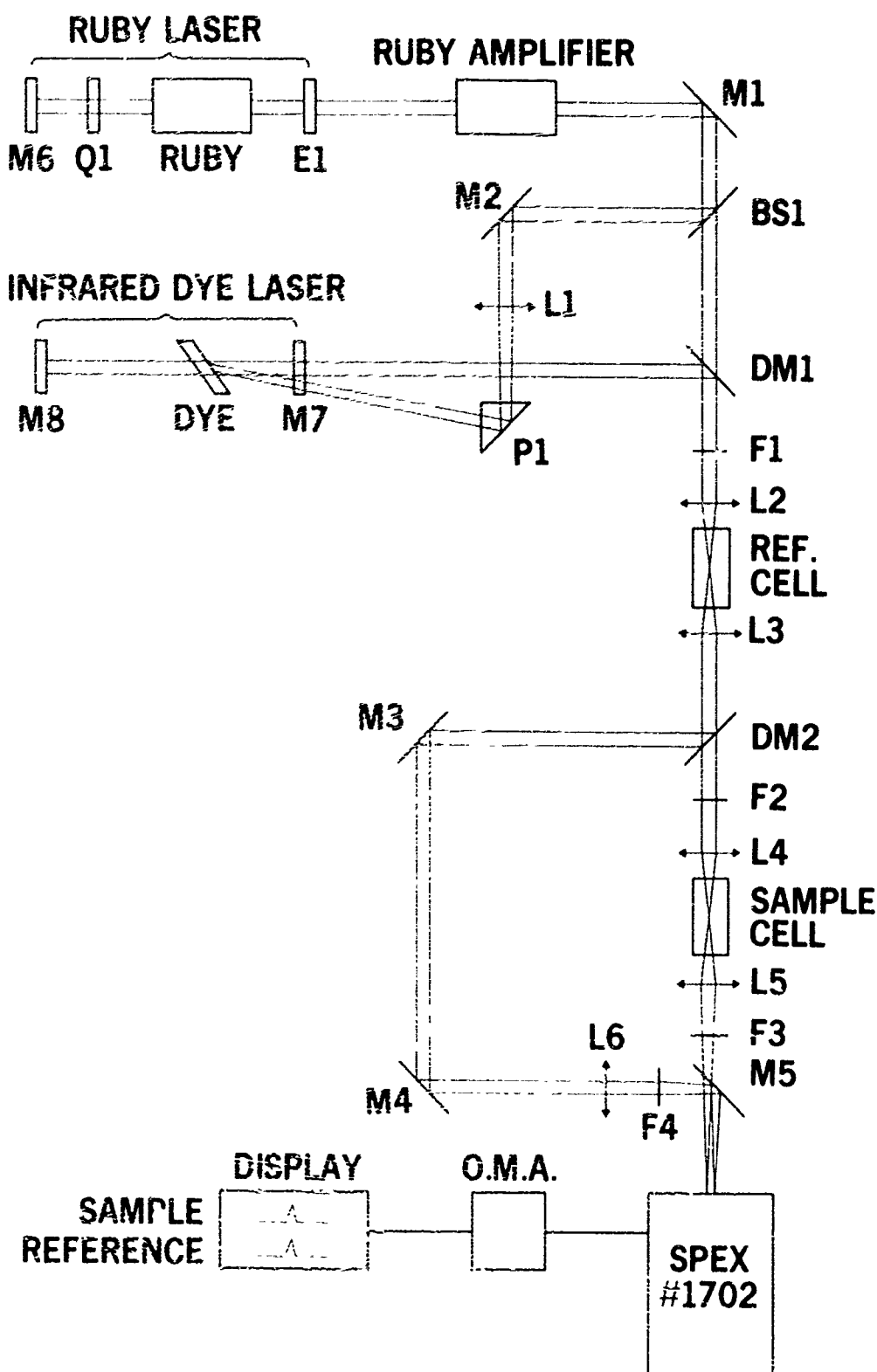
Figure 1. Schematic Diagram of the CARS System. The components are as follows: mirrors M1-M8; achromatic lenses L2-L4; simple lenses L1, L5-L6; filters F1-F4; dichroic mirrors DM1-DM2; beam splitter (70R/30T) BS1; prism P1; Q-switch Q1; output etalon E1; optical multichannel analyzer OMA.
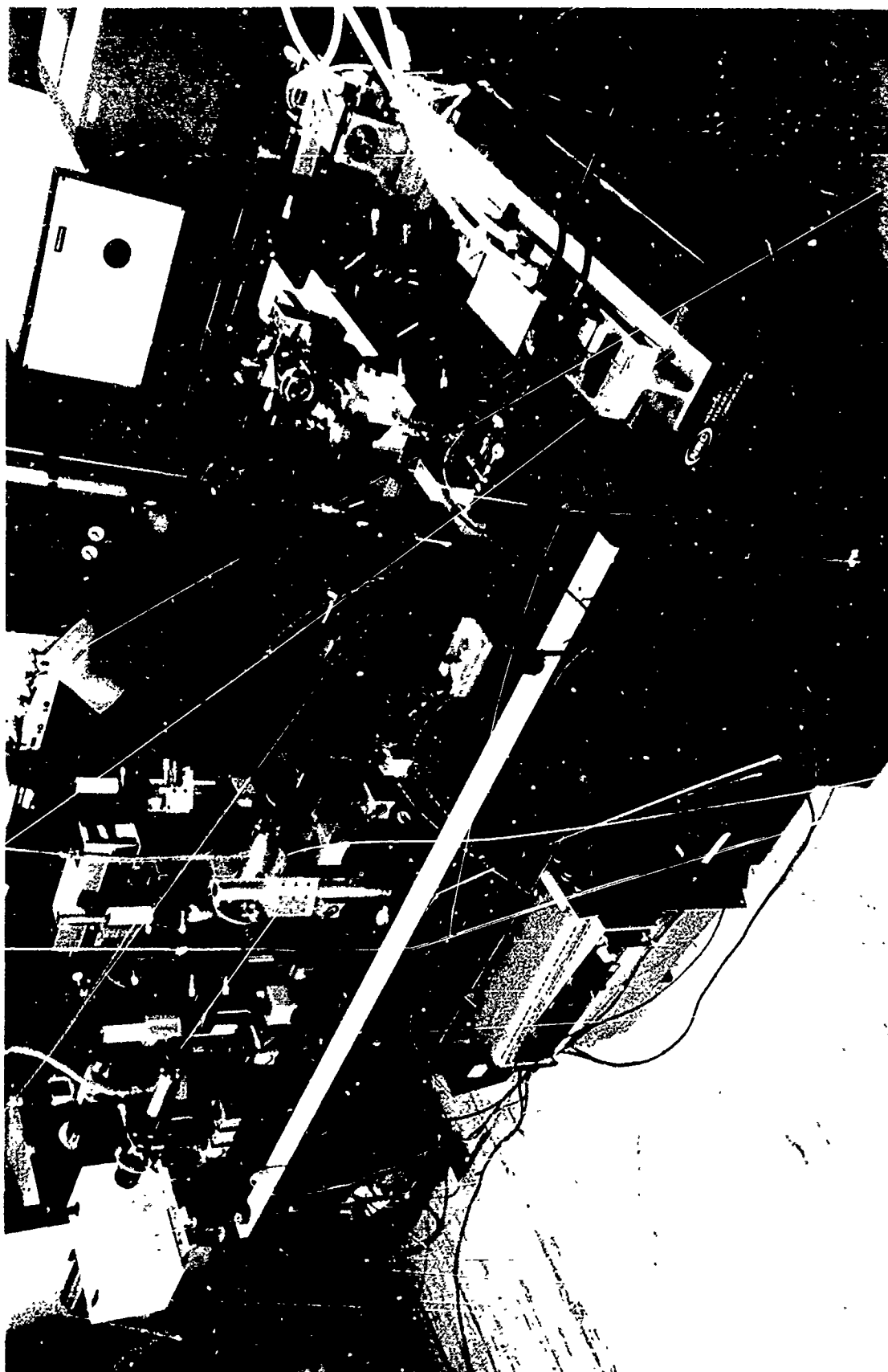
Figure 2. Photograph of the CARS System

(a) BROAD-BAND (SINGLE-PULSE) MEASUREMENT

(b) NARROW-BAND SIGNAL MEASUREMENT
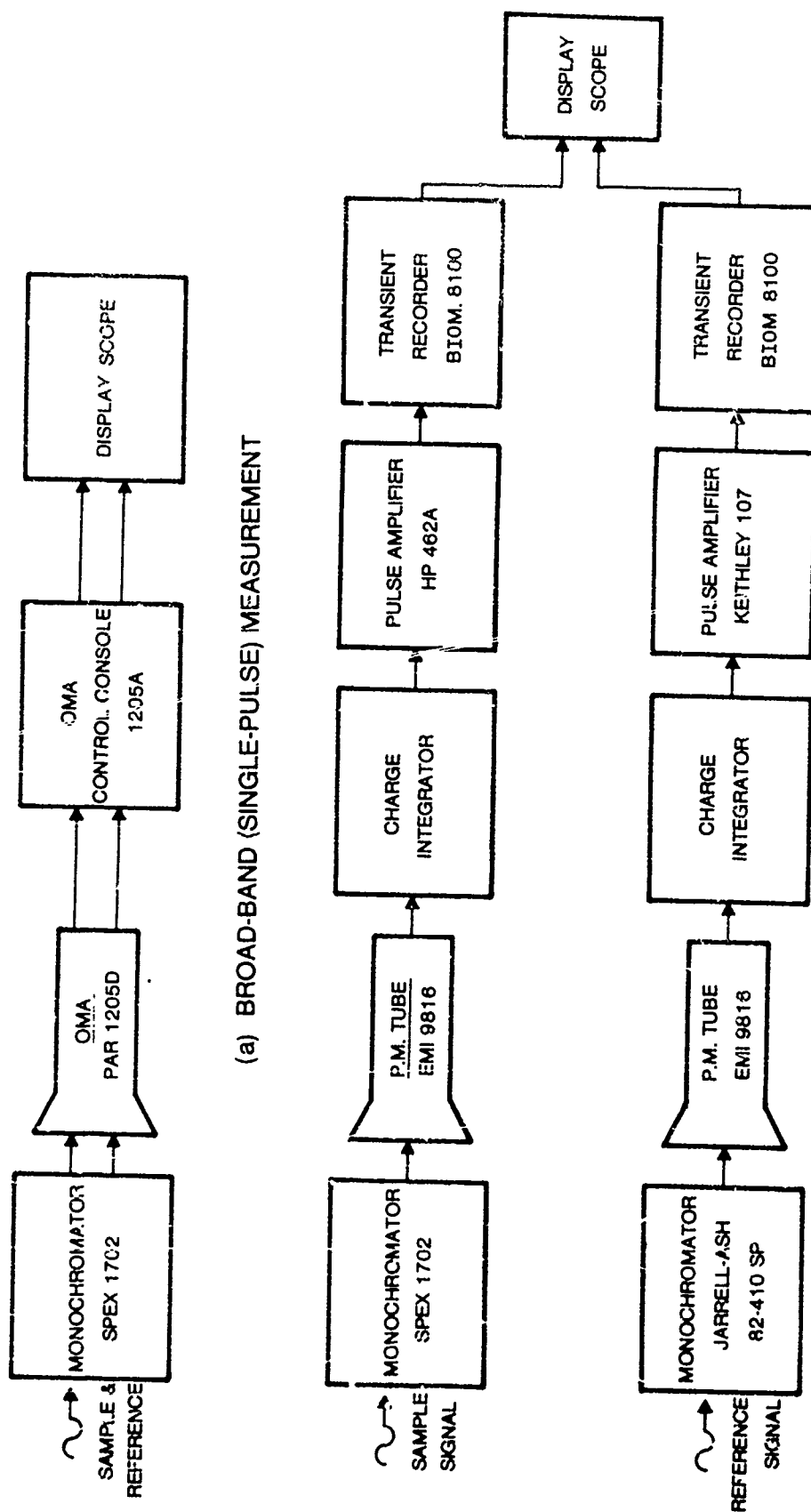
Figure 3. Block Diagram of Signal-Processing Electronics for CARS System

24

mode the dye laser is tuned broad-band (typically 100 cm^{-1} wide), and the generated anti-Stokes signals from the sample and reference cells are dispersed within a single monochromator and detected by a dual-spectrum optical multichannel analyzer (OMA). Separation of the two optical signals is accomplished by focusing the anti-Stokes beams on two different points on the entrance slit of the monochromator. Because of the instantaneous nature of the generation of the entire spectrum, this mode of operation is more desirable for real-time measurement of gas temperatures.

2) Narrow-Band Operation. This mode of operation is employed for generation of a point in the anti-Stokes spectrum of a gas utilizing a narrow-band dye-laser line (typically $\lesssim 0.2$ cm^{-1}). The anti-Stokes signals are dispersed in two separate monochromators and detected by photomultipliers. The photomultiplier-output pulses are integrated in an RC circuit and amplified before being stored in a transient recorder. The stored pulses are subsequently displayed on an oscilloscope for monitoring. Since the spectral power density of the narrow-band dye laser is generally much higher than that of the broad-band laser, the anti-Stokes intensity generated is higher with narrow-band operation. Furthermore, since photomultipliers are used in place of the OMA as shown in Fig. 1, the overall sensitivity is also much higher. However, in order to generate the spectrum of an entire band in this mode, hundreds of laser pulses scanning the Stokes region are required. For these reasons, this mode of operation is better suited to species-concentration measurements.

In the following subsections, the two lasers of the CARS system (i.e., ruby laser and dye laser) and the gas-handling system will be described in detail.

2. RUBY LASER

The ruby laser is a Korad K-1000 oscillator-amplifier system extensively modified for single-mode operation. Figure 4 is a photograph of the ruby oscillator. The oscillator consists of a two-element output etalon (Korad

Figure 4. Photograph of Ruby Oscillator

KLMS Mode Selector), a ruby head (K-1), a pin-hole aperture, a Q-switch--
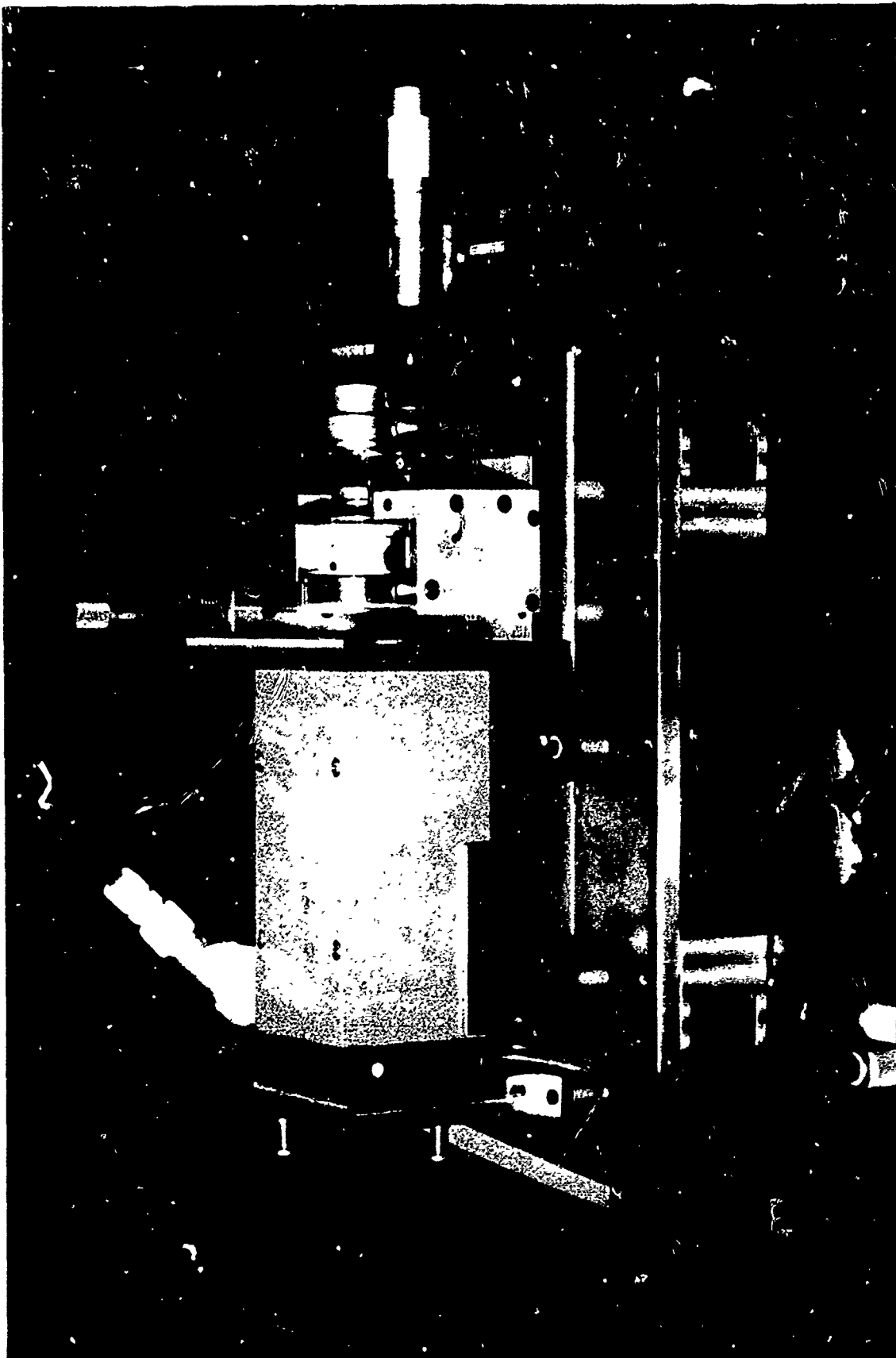either passive (a saturable dye) or active (a Pockels cell)--and a 100%
reflecting mirror. All optical components were mounted on a zero-expansion
glass plate (Cer-Vit) to provide thermal stability, and the cavity length
was minimized at 27 cm. (When the optical length of the ruby rod is taken
into account, this cavity takes on the longitudinal mode spacing of
~ 0.014 cm^{-1}). In addition, the output etalon and the ruby rod were
temperature-regulated by means of a heat exchanger (KWC7). The oscillator-
output beam was amplified by double-passing it through the amplifier using
a rooftop prism having an apex angle of 88° to permit beam crossing at the
center of the amplifier rod.

The output energy of the ruby-laser pulse was measured from time to
time using a Scientech laser-power meter (Model 3600). The power was
estimated by dividing pulse energy by pulse duration (typically 15-20 nsec)
as measured by a PIN diode and a transient digitizer (Tektronix R7912).
In general, the oscillator-output power was in the 0.5-1.0 MW range when
a 2-mm ϕ pin-hole aperture was used. The amplifier was used to increase
the power up to ~ 5 MW.

The linewidth of the ruby-laser beam was measured by means of a Fabry-
Perot interferometer (FSR = 0.28 cm^{-1}; finesse ≈ 50) and an optical multi-
channel analyzer. A small portion of the ruby beam was directed into the
interferometer through a short-focal-length lens, and the profile of the
interference fringes was recorded on an OMA. The interference fringes are
shown in Figs. 5 and 6. The linewidth (FWHM), measured for the passive
and active Q-switching oscillator configurations, was 0.034 and 0.047 cm^{-1},
respectively.

In order to facilitate the operation of the CARS system, an electronic
control unit for regulating the firing of the ruby laser and subsequent
data acquisition was fabricated and incorporated into the system. In
addition, allowing laboratory personnel to concentrate on other aspects
of the measurements during experiments, the control unit contributes to

27

Figure 5. Mode Structure of Passively Q-switched Ruby Laser Determined by Means of a Fabry-Perot interferometer (FSR = 0.28 cm^{-1}; Finesse $\approx$ 50) and an Optical Multichannel Analyzer
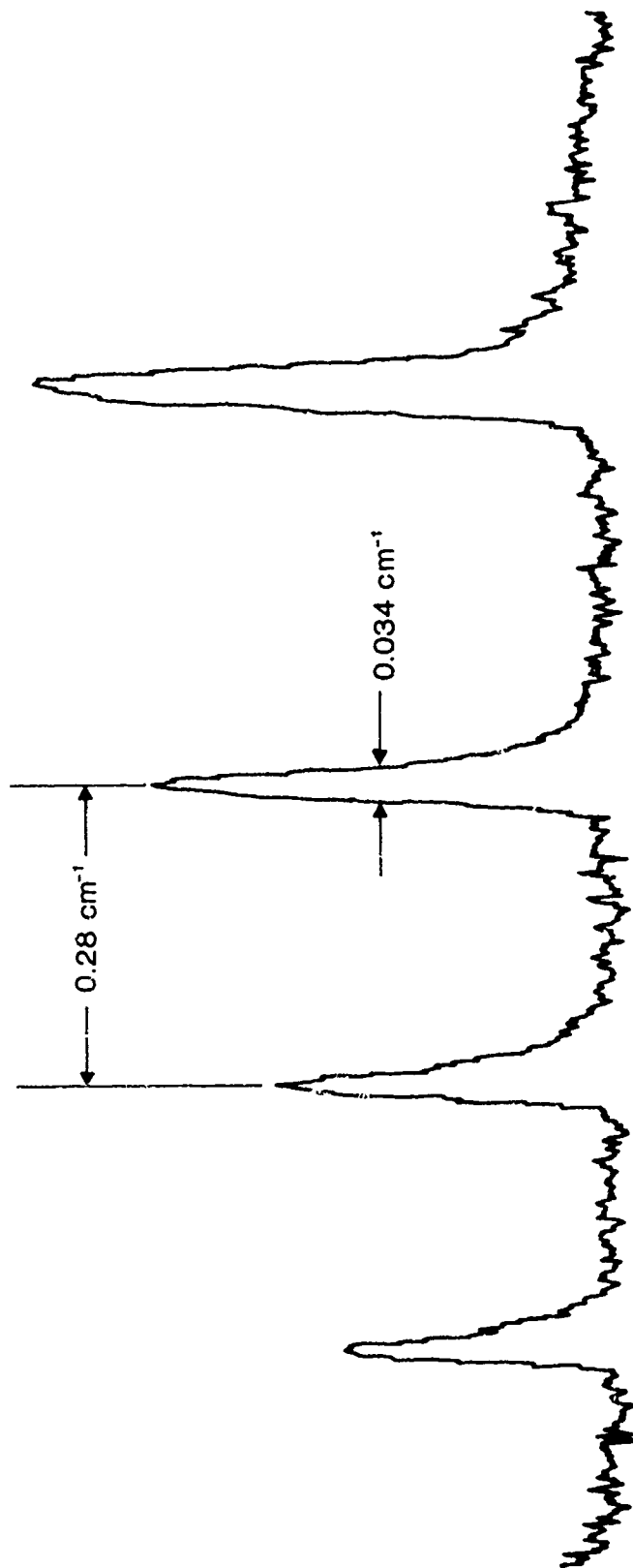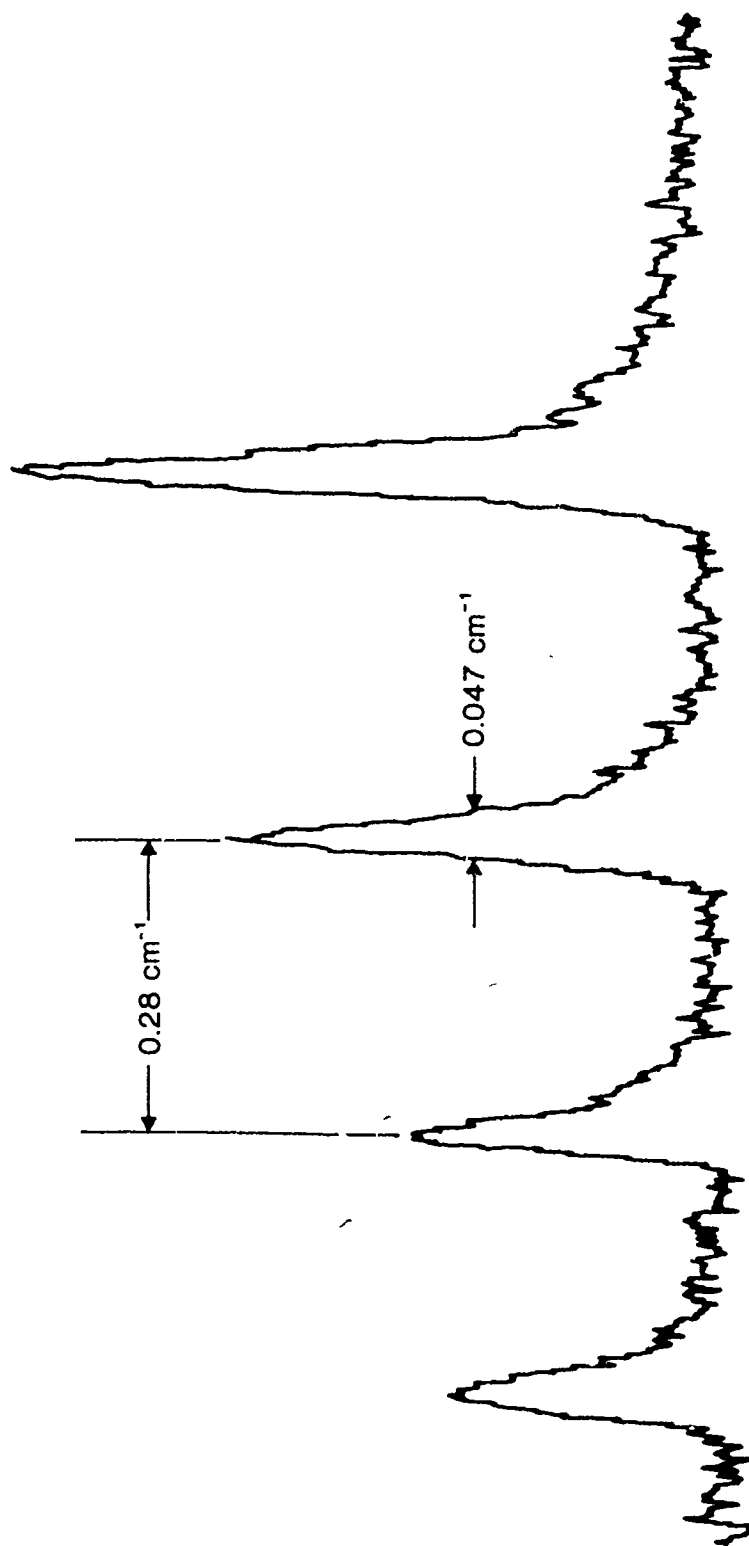
Figure 6. Mode Structure of Actively Q-switched Ruby Laser Determined by Means of a Fabry-Perot Interferometer (FSR = 0.28 cm^{-1}; Finesse ≈ 50) and an Optical Multichannel Analyzer

0.047 cm^{-1}

0.28 cm^{-1}

29

the improvement of the frequency stability of the laser system since the laser is fired automatically at regular intervals. The circuit diagram of this unit is given in Appendix A.

Although the oscillator/amplifier system was powered in most cases by two Korad K-1 power supplies, it was necessary at times to use a K-25 power supply (high-repetition-rate design) in conjunction with a K-1 unit (low-repetition-rate design). In such cases a suitable timing device was required for synchronizing the gain maxima in the ruby rods powered by different power supplies. For the K-25 power supply a delay of ~ 500 μsec for the fire-command pulse from the K-1 unit was found to be suitable for accomplishing this synchronization. A Korad Pockels-cell shutter control was employed as the variable time-delay unit. However, because of the impedance mismatch between the shutter control and the K-25 power supply, a direct interconnection could not be employed. An additional buffer network was designed and fabricated to overcome this difficulty. The circuit diagram of this network is also given in Appendix A. The delayed fire-command pulse from the shutter-control unit is first stretched in length to ~ 20 μsec and then amplified and impedance-matched for the K-25 power supply. The optimum delay for a maximum optical gain through the amplifier driven by the K-25 was found to be ~ 350 μsec.

3   DYE LASER

The basic dye laser consists of a 100% and a 35% reflecting flat mirror, a static dye cell, and a pin-hole aperture. This dye-laser configuration was used for broad-band applications such as single-pulse CARS experiments. For narrow-band operation, a rotatable intra-cavity interference filter (one of four narrow-band, high-peak-transmittance, Carl Zeiss filters having center wavelengths of 820, 867, 928, and 995 nm) and up to two solid Fabry-Perot etalons (0.1 and 1.0 mm thick) were incorporated into the cavity for tuning and line-narrowing purposes. With no dispersive element in the cavity, the dye laser operates with a linewidth of ~ 100 cm^{-1}. Insertion of an interference filter reduces the linewidth to ~ 15 cm^{-1}; addition of a thin etalon (0.1-mm unit) narrows it to ~ 2 cm^{-1}; and a second etalon narrows it further to 0.2 cm^{-1}. The dye laser is shown pictorially in Fig. 7.
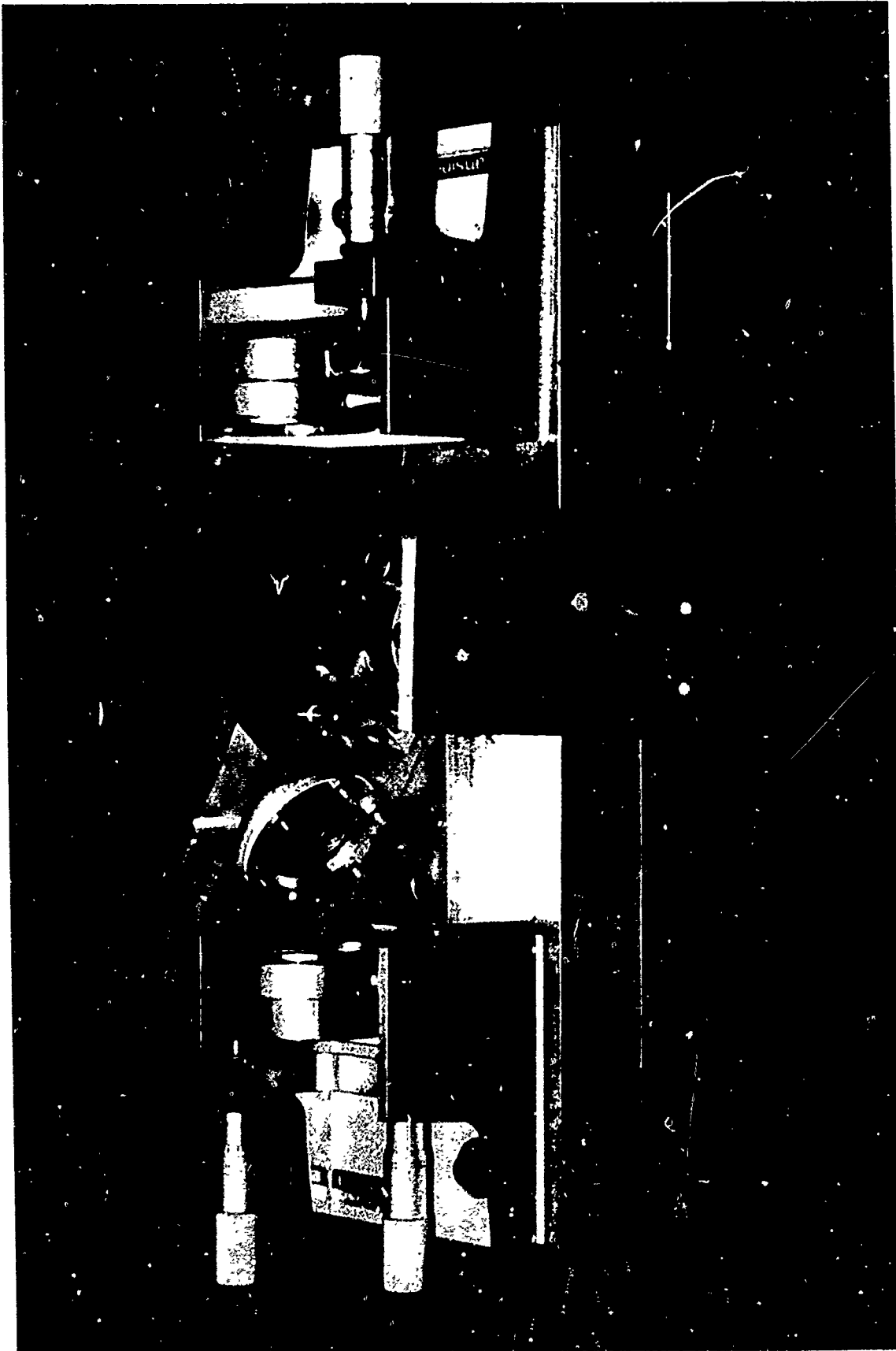
Figure 7. Photograph of Dye Laser

31

In CARS experiments employing a ruby laser as a pump, the dye laser operates in the 0.7 to 1.0 μ region for all molecular gases of interest as shown in Table 1. Several organic dyes are available which lase in this region when they are pumped by a ruby beam [22,23]. Figure 8 shows the lasing characteristics of a group of such dyes. It can be observed that all wavelengths pertinent to CARS can be generated through proper selection of dyes or dye mixtures. These dyes also lase with flash-lamp pumping, but at substantially longer wavelengths [24]; for example, Kodak dye IR132 lases at about 860 nm when pumped with a ruby beam as compared to 972 nm when pumped with a xenon flash lamp. Even with ruby-laser pumping, the lasing wavelength varies considerably and is dependent upon such parameters as dye concentration, solvent, cavity and pumping configuration, and pump power [23]. In fact, adjustment of dye concentration is an important technique for broad-band tuning of the dye laser.

All organic laser dyes exhibit chemical instability, which represents a grave problem in their use. Infrared dyes which cover some of the most useful spectral regions (especially those lasing at longer wavelengths) for CARS applications suffer most from this instability. In fact, the dyes No. 10 and No. 11 shown in Fig. 8 gradually deteriorate even during storage in a refrigerator. Since this deterioration manifests itself by reduction in power output as well as tuning range in addition to shift in lasing wavelength, it was increasingly difficult to maintain dye-laser performance for wavelengths beyond 0.9 μ using the batch of dyes on hand.

One of the complications associated with interference-filter tuning is the etalon-effect of the intra-cavity interference filters. Although interference filters had been used routinely for tuning purposes, their etalon-like behavior was neither suspected nor observed until a high-dispersion eschelle grating was incorporated into the spectrometer late in the program. Figure 9 is a high-resolution spectrum of the dye laser with a Carl Zeiss No. 995 interference filter in the cavity. A check on the mode spacing (~ 1.5 cm^{-1}) of this spectrum confirmed that the etalon was being formed between the two surfaces of the filter substrate. Initially this was quite surprising in view of the fact that the second surface of

32

TABLE 1. MOLECULAR VIBRATION FREQUENCIES, STOKES AND ANTI-STOKES
WAVELENGTHS CORRESPONDING TO RUBY LASER EXCITATION, AND
APPROPRIATE LASER DYES THAT MAY BE USED FOR GENERATING
THE STOKES COMPONENT

Species	Vibration Frequency (cm^{-1})	Stokes Wavelength (Å)	Anti-Stokes Wavelength (Å)	Appropriate Laser Dye*	Remarks
O_2	1556	7784	6266	No. 16	
CH_4	2914	8704	5775	IR 144	ν_1
N_2	2331	8284	5976	No. 17	
CO	2143	8157	6044	No. 17	
CO_2	1388	7683	6333	No. 16	($10^{o}0$)
	1286	7624	6374	No. 16	($02^{o}0$)
H_2O	3654	9304	5538	No. 10	
H_2	4160	9764	5387	No. 10 + No. 11	
NO	1877	7983	6143	No. 17	
OH	3569	9231	5564	No. 10	
HF	3962	9578	5445	No. 10 + No. 11	
HD	3627	9281	5546	No. 10	
DF	2906	8699	5777	IR 144	
CH	2920	8709	5772	IR 144	Average value
HCl	2885	8683	5784	IR 144	
D_2	2994	8766	5748	IR 144	

*Dye numbers are in reference to those used in Fig. 8,
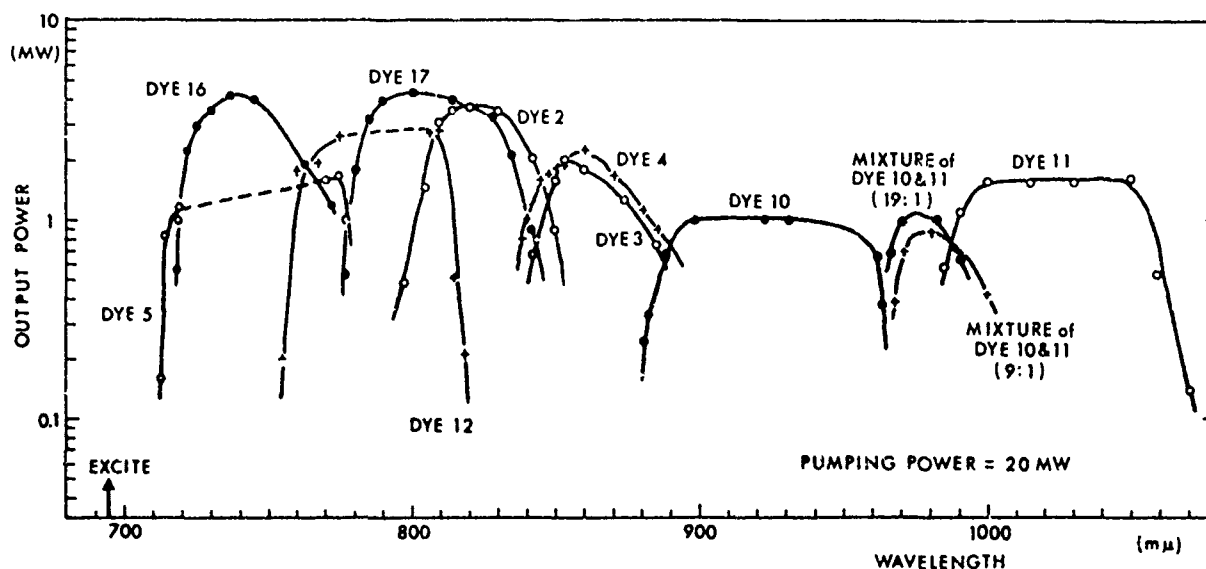except for IR 144 which is a Kodak designation.

Figure 8. Plot of Ruby-Pumped Dye Laser Output Peak Power as a Function of
Wavelength. Over the dotted lines, it is impossible to obtain
laser emission. Solvent: Glycerin (Dye 12), Methanol (Dye 17),
and Acetone (other dyes). The dyes are identified below:
(from Ref. 22)

| Dye |
| --- |
| (¹) Thiacarbocyanine |
| Dye 1 3, 3'-Diethyl-2, 2'-thiadicarbocyanine iodide |
| Dye 2 3, 3'-Diethyl-2, 2'-thiatricarbocyanine iodide |
| Dye 3 3, 3'-Diethyl-2, 2'-(5, 6, 5', 6'-tetramethoxy) thiatricarbocyanine iodide |
| Dye 4 3, 3'-Diethyl-2, 2'-(4, 5, 4', 5'-dibenzo) thiatricarbocyanine iodide |
| Dye 5 3, 3'-Diethyl-10-chloro-2, 2'-(4, 5, 4', 5'-dibenzo) thiadicarbocyanine iodide |
| Dye 6 3, 3'-Diethyl-10-chioro-2, 2'-(5, 6, 5', 6'-dibenzo) thiadicarbocyanine iodide |
| (2) Quinocarbocyanines |
| Dye 7 1, 1'-Diethyl-4, 4'-quinocarbocyanine iodide   (Cryptocyanine) |
| Dye 8 1, 1'-Dimethyl-4, 4'-quinocarbocyanine iodide |
| Dye 9 1, 1'-Diethyl-4, 4'-quinocarbocyanine bromide |
| Dye 10 1, 1'-Diethyl-2, 2'-quinotricarbocyanine iodide |
| Dye 11 1, 1'-Diethyl-4, 4'-quinotricarbocyanine iodide |
| Dye 12 1, 1'-Diethyl-11-bromo-2, 2'-quinodicarbocyanine iodide |
| Dye 13 1, 1'-Dimethyl-11-bromo-2, 2'-quinodicarbocyanine iodide |
| Dye 14 1, 1'-Diethyl-11-bromo-4, 4'-quinodicarbocyanine iodide |
| (3) Oxacarbocyanines |
| Dye 15 3, 3'-Diethyl-2, 2'-oxatricarbocyanine iodide |
| Dye 16 3, 3'-Dimethyl-2, 2'-oxatricarbocyanine iodide |
| (4) Indocarbocyanine |
| Dye 17 1, 3, 3, 1', 3', 3'-Hexamethyl-2, 2'-indotricarbocyanine iodide |
| (5) Selenacarbocyanine |
| Dye 18 3, 3'-Diethyl-2, 2'-selenatricarbocyanine iodide |
| (6) Thiazolinocarbocyanine |
| Dye 19 3, 3'-Diethyl-2, 2'-(5, 5'-dimethyl) thiazolinotricarbocyanine iodide |

34
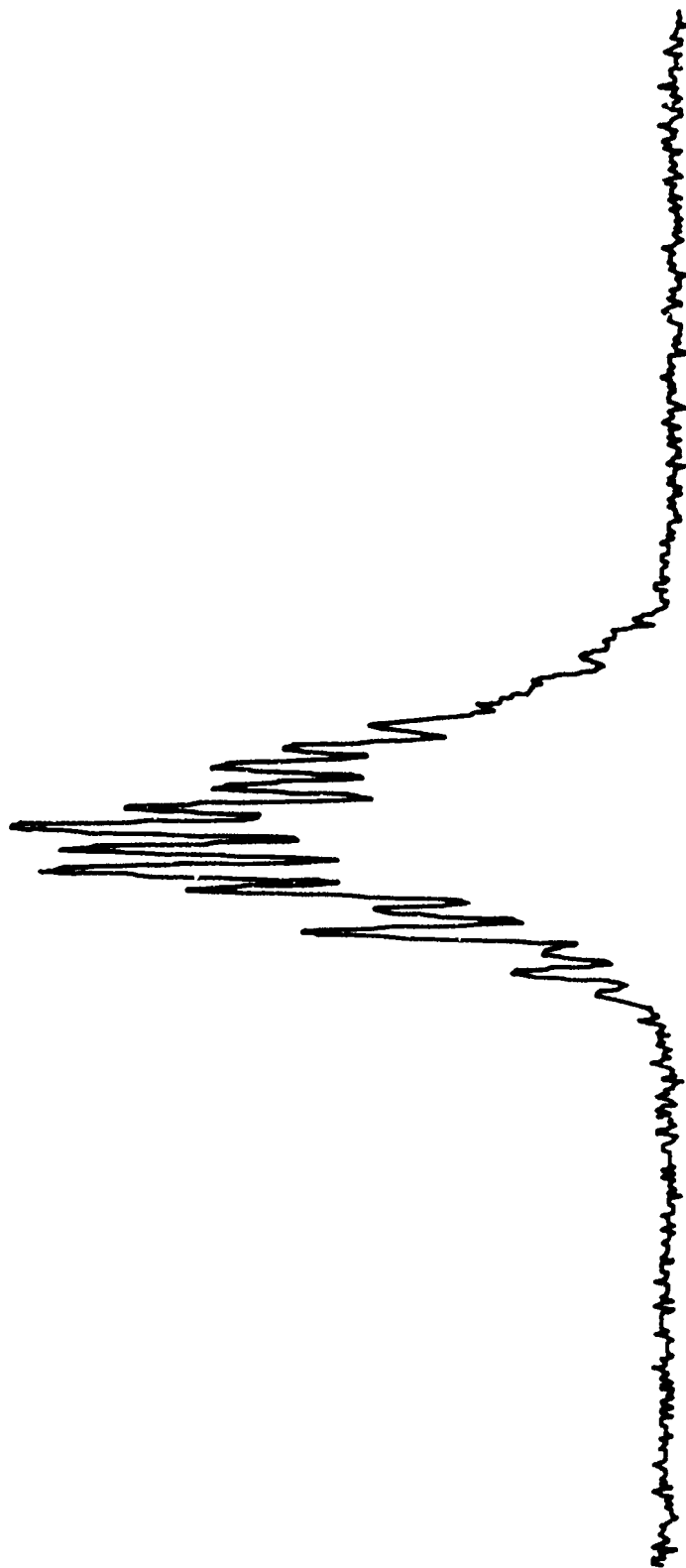
Figure 9. High-Resolution Spectrum of Interference-Filter-Tuned Dye Laser. Etalon-like behavior of the interference filter was confirmed by checking the mode spacing (1.5 cm^{-1}) and the optical thickness of the filter substrate.

the filter was anti-reflection coated. However, these interference filters have a rather high peak transmittance (typically > 92%) and, therefore, even a small reflection from the second surface--say 1%--could be sufficient to cause an etalon effect in connection with the 8% reflection from the first surface.

4. GAS-HANDLING SYSTEM

The gas-handling system was designed in such a way that up to four different gases can be mixed by the "partial-pressure" method or used individually. A schematic diagram of the system is shown in Fig. 10. The system is evacuated with a mechanical/diffusion pump combination prior to any gas-filling processes. The gas-mixing chamber is then filled with a gas to a predetermined pressure to be used by itself or as a component gas in the mixture. If a gas mixture is desired, sufficient time (see Appendix B for a sample diffusion time calculation) should be allowed for the gases to mix thoroughly in the chamber through the diffusion process. The mixing chamber was designed to facilitate this mixing process. The mixture is then transferred to a high-pressure cell and/or a reference cell through a metering valve and to a low-pressure sample cell through a regulator and a metering valve. The pressures can be monitored throughout these steps by means of three pressure gauges logically placed in the system. Bleeding valves are provided to vent the high-pressure gases when gas changeover is required. The system was made as portable as possible by mounting all gauges, the gas-mixing chamber, and most of the valves on a rack. Consequently, the system can be placed adjacent to either the optical table or the operator, depending upon the experimental requirements.

The question of hydrogen embrittlement of valves was investigated quite thoroughly. All the experts consulted agreed that this embrittlement would be no problem at pressures of 1000 psi for Type 316 stainless steel from which the valves are fabricated (300 Series stainless steels are immune to this problem, whereas 400 Series stainless steels are not). The only potential problem area is the valve stem which, because of its composition (17-4 PH stainless steel), might be affected in the long run and develop a slow leak through the valve.

36

Figure 10. Vacuum/Gas-Handling System
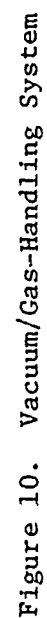
The system was tested several times during various stages of assembly, and has shown satisfactory performance--final tests have shown that the system can be pumped to below 10^{-5} Torr, as measured at the pumping port, and that it exhibits less than 0.5% pressure drop under high-pressure conditions (up to 1000 psi) during a 24-hr test period. Figure 11 shows a front view of the system control rack. An operational instruction sheet along with the parts list has been prepared and is attached to this report as Appendix C. Figure 12 is a photograph of the gas cell. The same cell design was used for both high-pressure and low-pressure applications. The quartz windows on the cell are of good optical quality and have sufficient mechanical strength to withstand pressures of up to 60 atm. The cells were made from Type 304 annealed stainless steel.
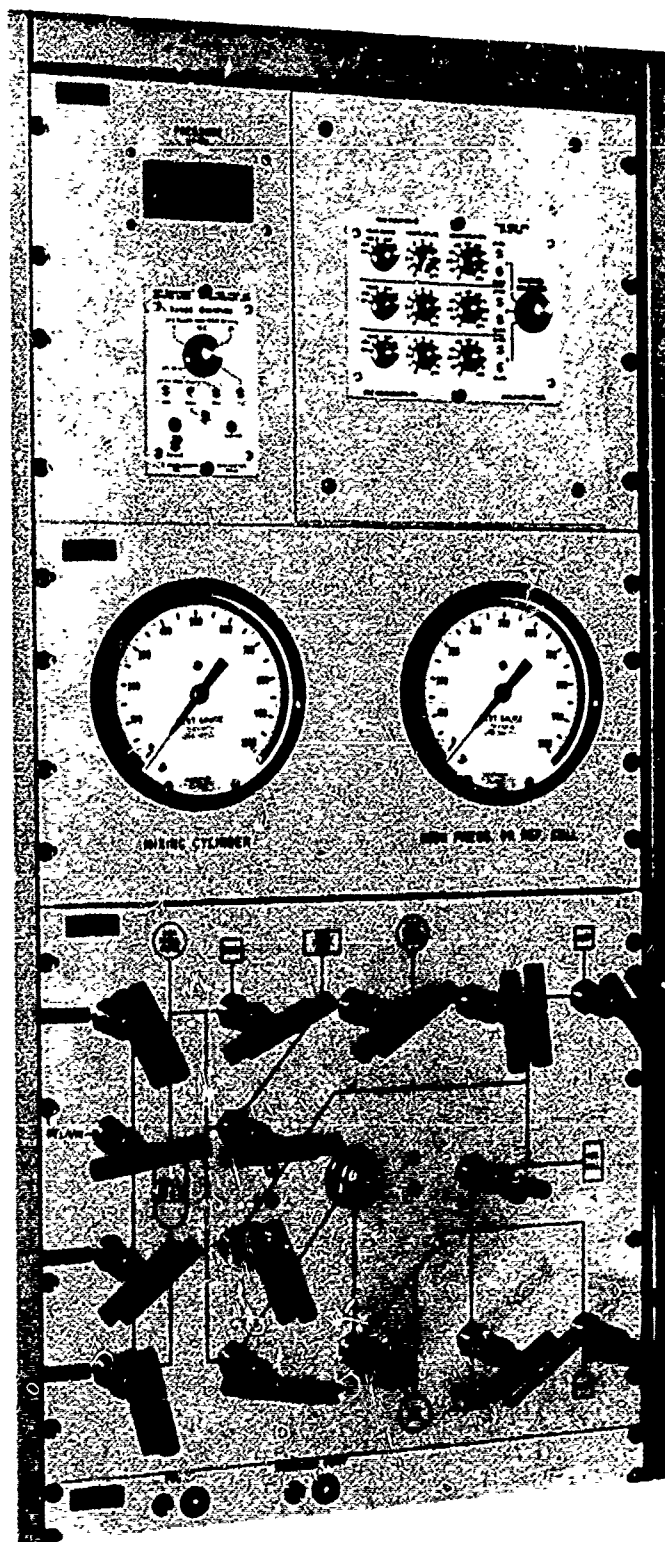
Figure 11.   Front View of Vacuum/Gas-Handling System
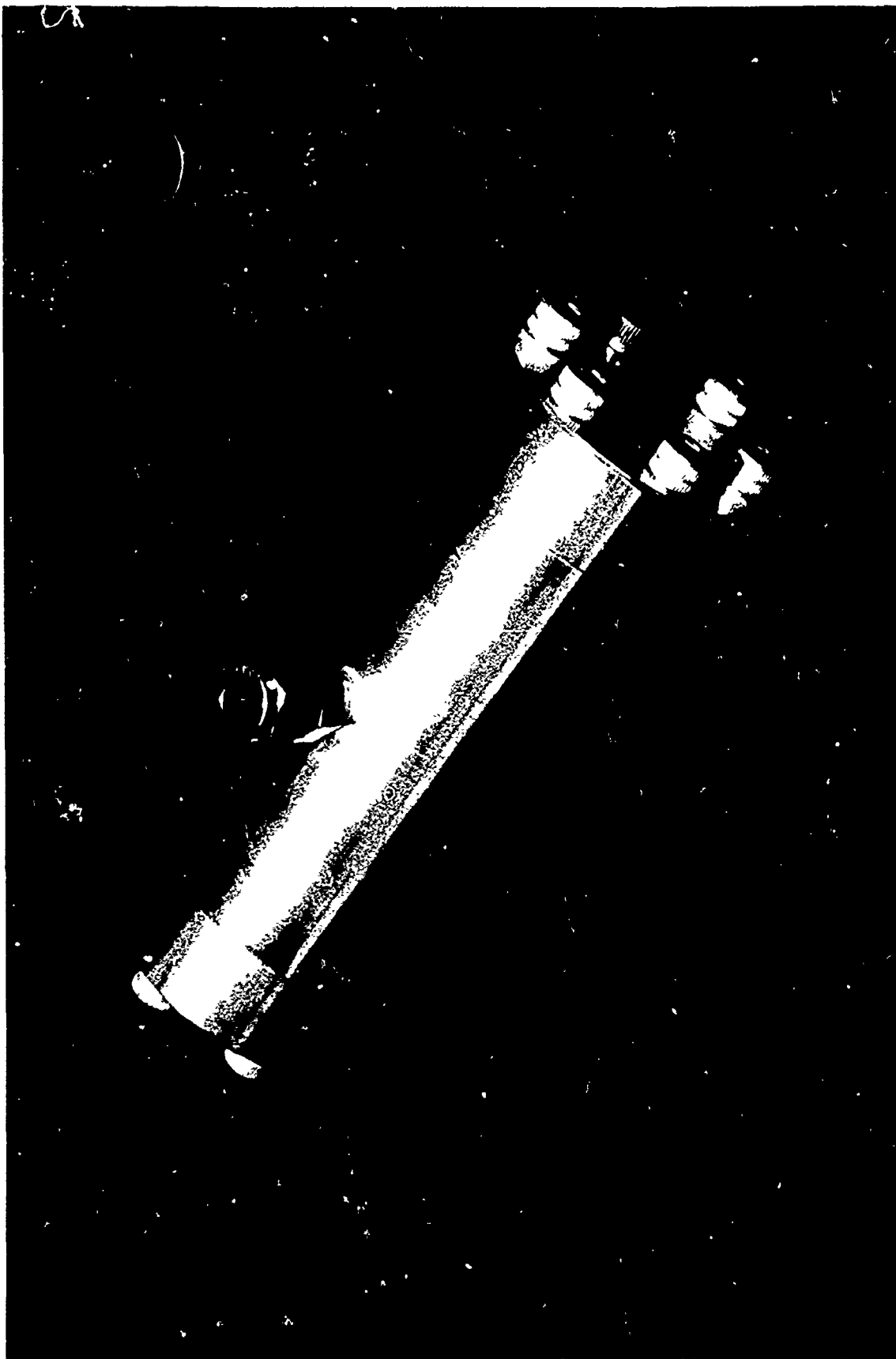Control Rack

Figure 12. Photograph of Gas Cell

SECTION IV

EXPERIMENTAL TECHNIQUES AND RESULTS

1. SINGLE-PULSE CARS SPECTRA AND ROTATIONAL-
   TEMPERATURE ESTIMATION

Single-pulse CARS is a technique by which an entire vibration-rotation band (or bands) of the CARS spectrum of molecular gases can be generated simultaneously using a single laser pulse. Since the laser pulses are only ~ 15 nsec in length, and an entire band spectrum can be generated in such a short time period, one can effectively "freeze" the media and obtain truly time-resolved measurements of such parameters as gas concentration and temperature. This technique is essential in making real-time measurements in nonstationary media, where the information on temporal profiles of the parameters is just as important as information on spatial ones. In stationary media this technique permits measurement of not only the average values of the parameters but also their statistical distribution within the media.

The crucial components in this experiment are a broad-band dye laser which provides uniform excitation of all lines of the anti-Stokes spectrum and a dual-spectrum optical multichannel analyzer which records both sample and reference signals simultaneously. The details of the experimental procedure were given in Section III-1A on broad-band operation.

A. Hydrogen (H_2) Molecule

Figure 13 shows the entire spectrum of Q-branch lines of H_2 gas along with that of the reference gas. The simultaneous recording of the reference spectrum which provides the dye-laser lineshape allows the normalization of the sample-gas (H_2) spectrum according to varying intensity levels at various spectral locations of the sample Stokes lines.

Both sample and reference spectra having been recorded properly, the normalization of the sample spectrum was carried out as follows: First,

(a)

Q(1)

Q(0)   Q(2)   Q(3)
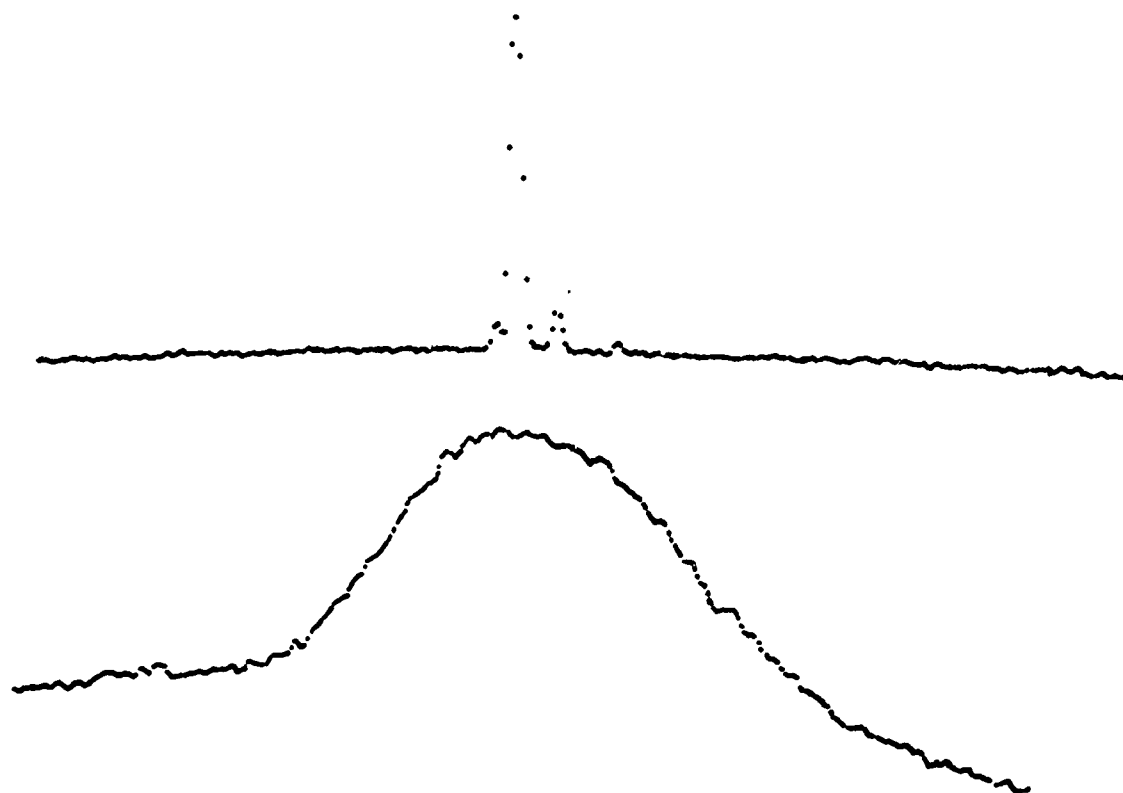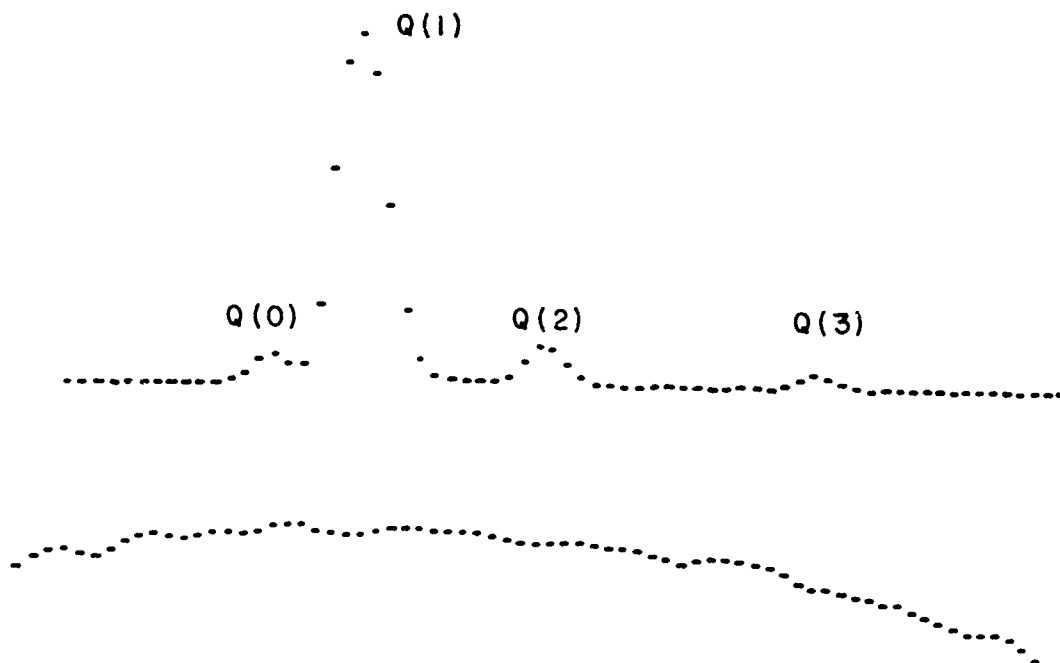
(b)

Figure 13.   Anti-Stokes Spectra as Recorded by an Optical Multichannel
Analyzer for (a) Upper Trace – H_2 Gas, Lower Trace – Reference
Gas; (b) Expanded Spectrum of (a)

the contribution of nonuniform dark current through the detector elements
(of OMA) was eliminated by the subtraction of the background level due to the
dark current from the "signal + dark current." The "dark-current-compensated"
spectra are shown in Fig. 14. By dividing the peak intensity of each H_2 line
[Q(0) through Q(3)] by that of the reference signal at the same spectral
location, the "normalized" H_2 spectrum was obtained. Since in the case of
a monochromatic pumping beam a one-to-one correspondence exists between
every component of the Stokes and anti-Stokes radiation (see Section II for
proof), this point-by-point normalization of the sample anti-Stokes spectrum
is justified. Figure 15 is a "stick diagram" of this normalized spectrum.
The theoretical intensity of each line is also shown for comparison purposes.

In order to estimate the temperature of a sample gas, the formula for the
intensity of individual vibration-rotation lines [as given by Eq. (42)] is
used. With this equation the temperature of a gas can be determined if
intensity measurements are made for two or more lines in a band. If the lines
being measured belong to different vibrational states, then vibrational as
well as rotational temperature can be estimated. Of course, in such a case
measurements on more than two lines will be required.

For an estimate of the rotational temperature, Eq. (42) can be
rewritten as

$$\frac{k}{2hc\,B_v} \cdot \ln\left[\frac{P_a(v,J)}{(2J+1)^2\,g_I^2}\right] = -\left(\frac{1}{T_r}\right) \cdot J(J+1) + K' \quad (54)$$

where all the nonpertinent terms are combined into a new constant K'. It
should be pointed out that in this equation, the expression $B_v J(J+1)$ is
substituted for $F_v(J)$, B_v being the rotational constant, and that the linewidth
is assumed to be constant for all anti-Stokes lines. Equation (54) has the
form $Y = \hat{a}X + \hat{b}$, where X and $\cdot$ are column vectors representing $J(J+1)$ and
the terms containing the logarithmic intensity, respectively, and $\dot{a}$ and $\dot{b}$
are the parameters to be estimated. The problem is now reduced to a simple
polynomial regression which can be solved by means of a least-squares routine.
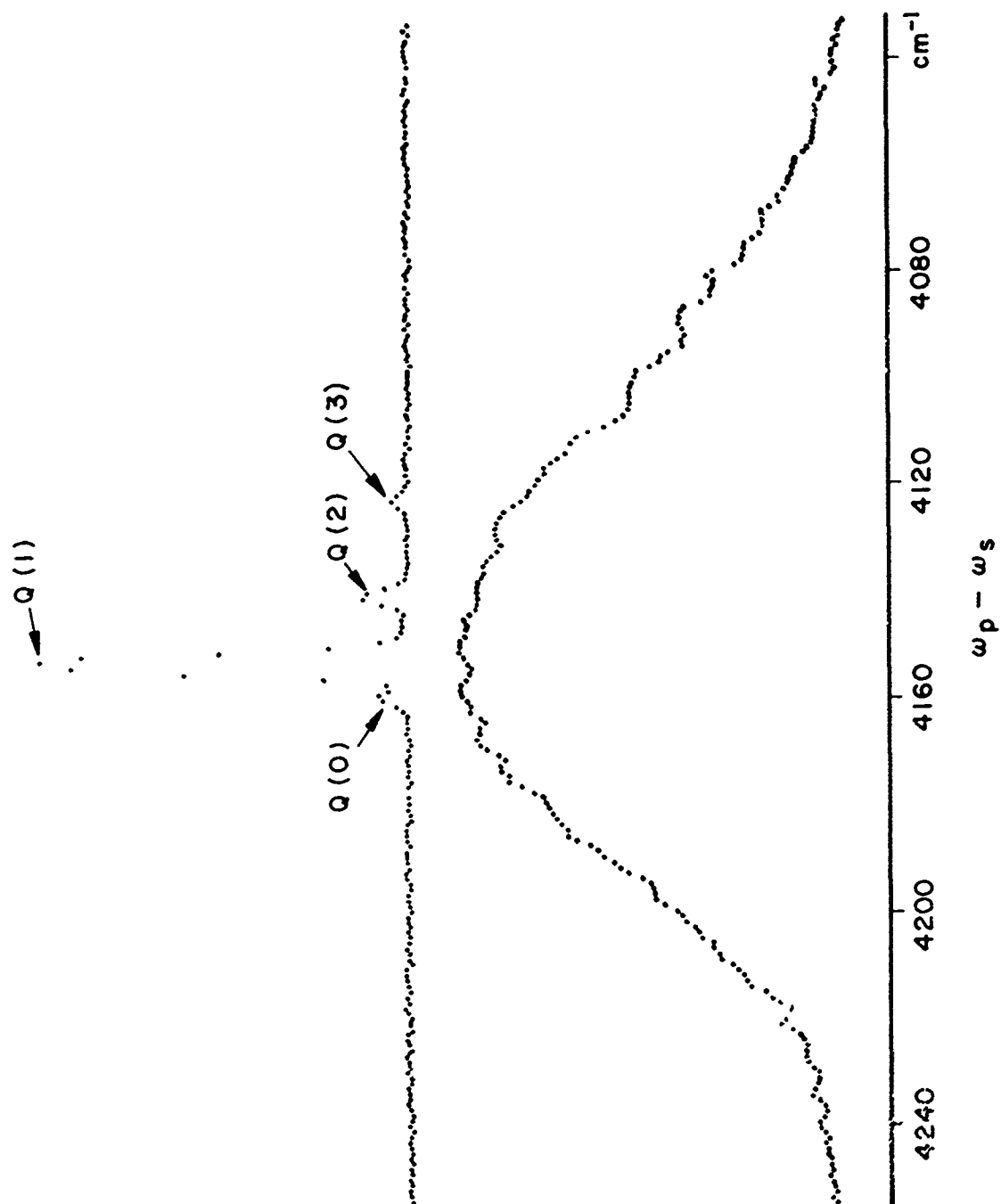The value of $\hat{a}$ is a measure of the rotational temperature ($\hat{a} = -1/T_r$), and

43

Figure 14. Dark-Current-Compensated Anti-Stokes Spectra: Upper Trace - H_2 Gas, Lower Trace - Reference Gas
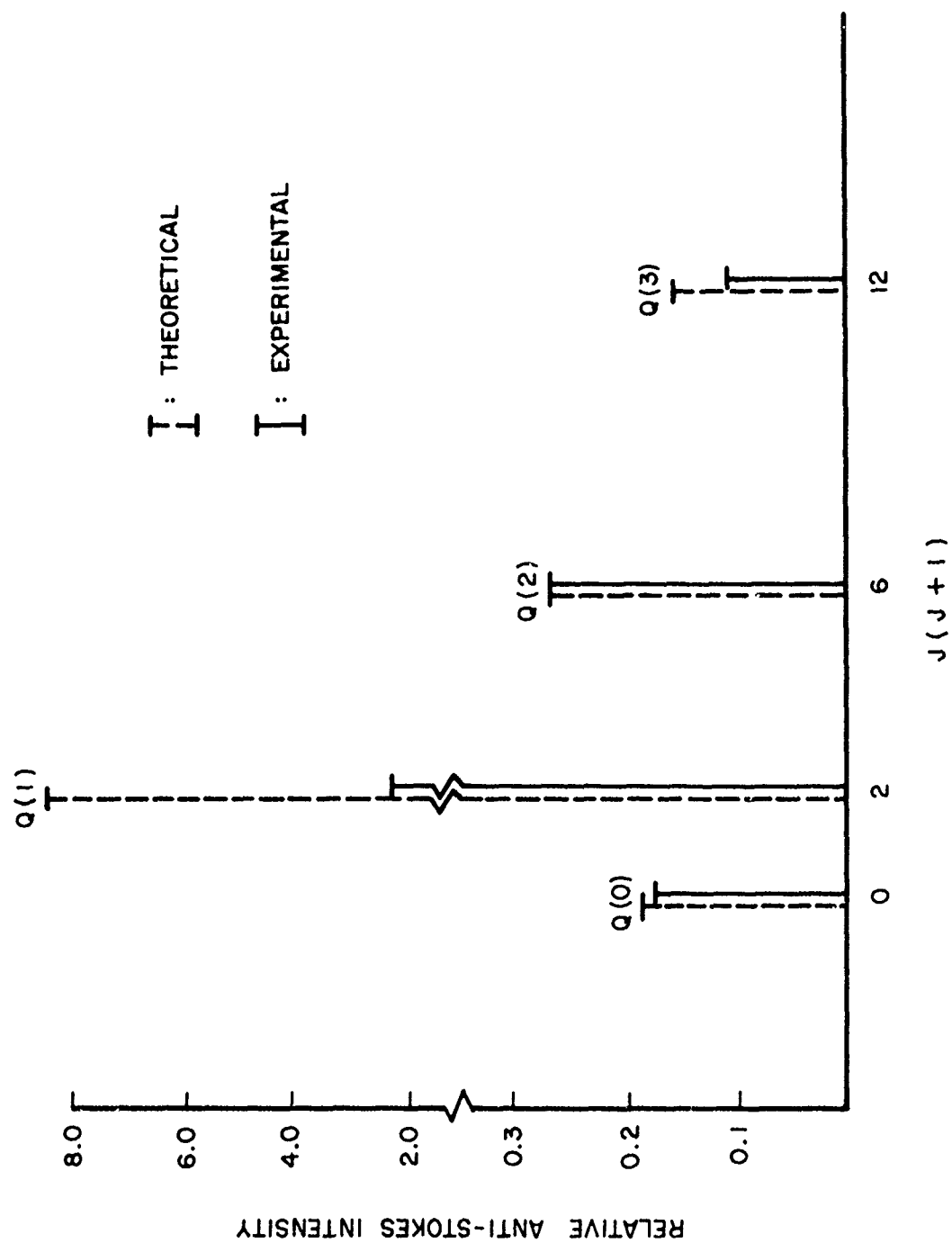
Figure 15. Normalized Anti-Stokes Spectrum of H_2

$\hat{b}$ is a measure of the molecular density. Figure 16 shows what might be called a "modified-Boltzmann plot" represented by Eq. (54). In this plot the absolute value of the slope of the line represents the reciprocal of the rotational temperature calculated by means of a least-squares program. The temperature values calculated in this manner ranged from 283 to 348°K for a set of four measurements made on H_2 at room temperature. Possible sources of error in this measurement are (1) the limited linearity in the dynamic response and cross-talk between adjacent elements of the optical multichannel analyzer, (2) the change in the relative molecular density in the rotational states during the interaction due to saturation, etc., and (3) the assumption of equal linewidth for all rotational lines.

In order to demonstrate the change in the relative intensity of the rotational lines, a spectrum was taken with the sample cell heated to ~ 415°K and compared with another taken at room temperature as shown in Fig. 17. The contrast in the relative intensity, particularly for Q(3) line, is quite dramatic.

B. Hydrogen Fluoride (HF) Molecule

Figure 18 shows a pair of single-pulse anti-Stokes spectra of the HF molecule. The upper spectrum was recorded early in the program using an existing grating (600 gr/mm, 17°-blaze) in the monochromator (Spex 1702). This spectrum has a limited resolution because of the cross-talk between adjacent elements of the optical multichannel analyzer. Since the resolution of the monochromator used was sufficient for the HF lines, it was possible to eliminate the difficulty by simply increasing the spatial dispersion of spectral lines at the detector. This was most easily accomplished by replacing the low-order grating in the monochromator with a high-dispersion eschelle grating. Although spatial dispersion can be increased by other means such as a magnifying lens placed in the detector plane, a number of potential problems associated with such methods made an eschelle grating the optimum solution to the problem. The grating chosen was a 632-g/mm grating having a blaze angle of 51°. Although a grating with a larger blaze angle gives more dispersion, the reduction in useful aperture (larger f number for the monochromator) makes such a grating less desirable.
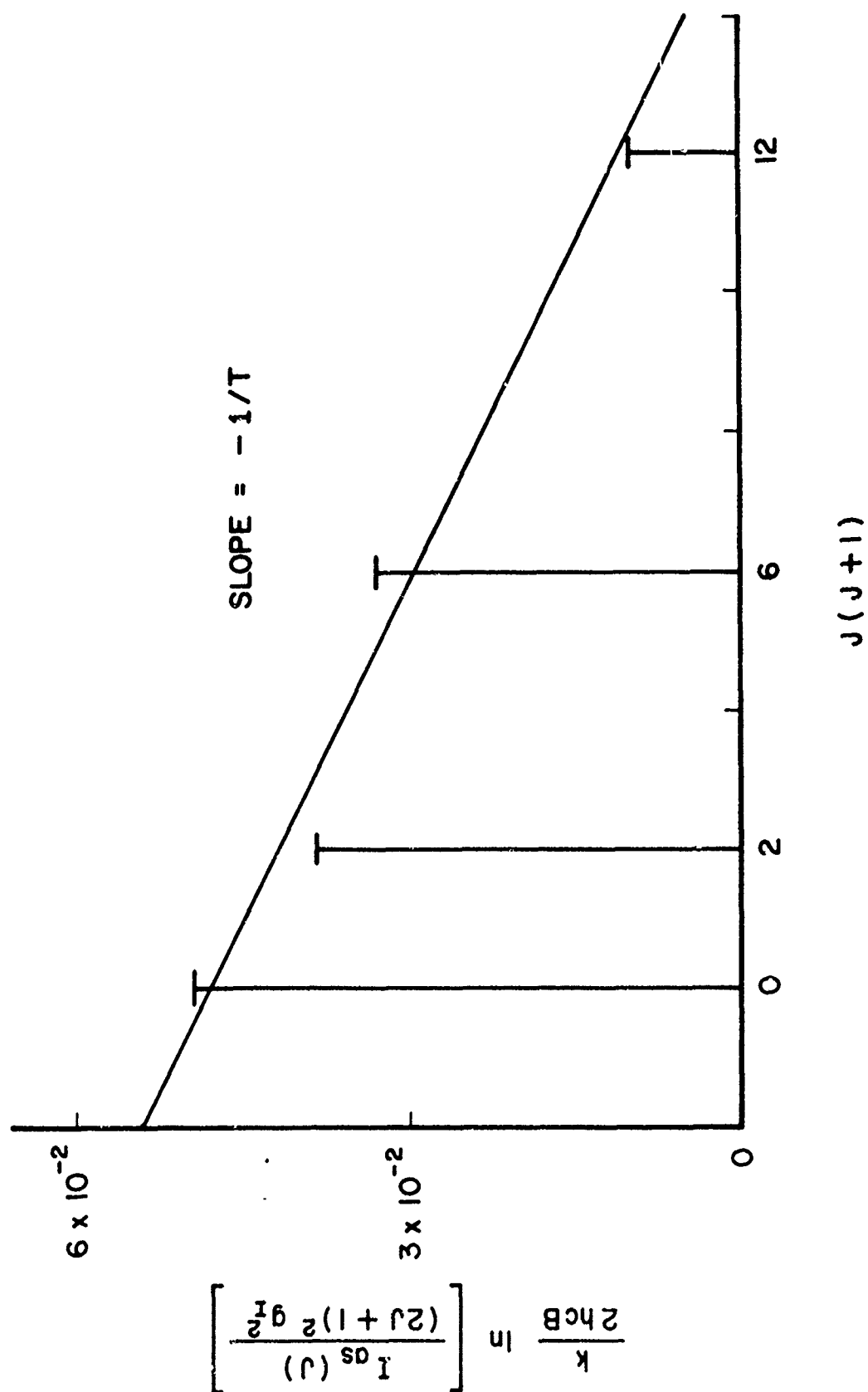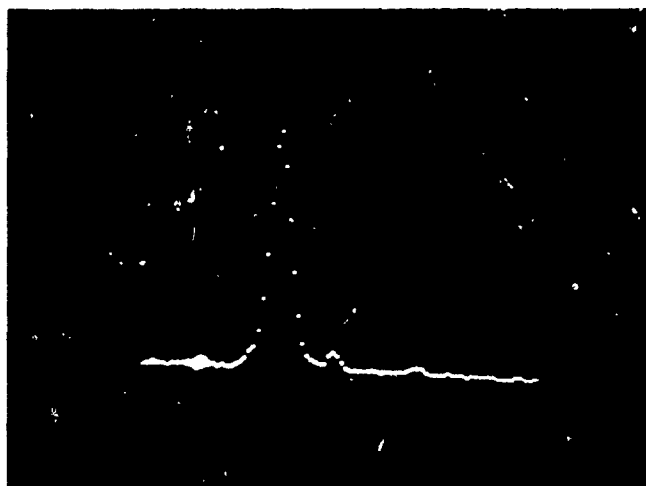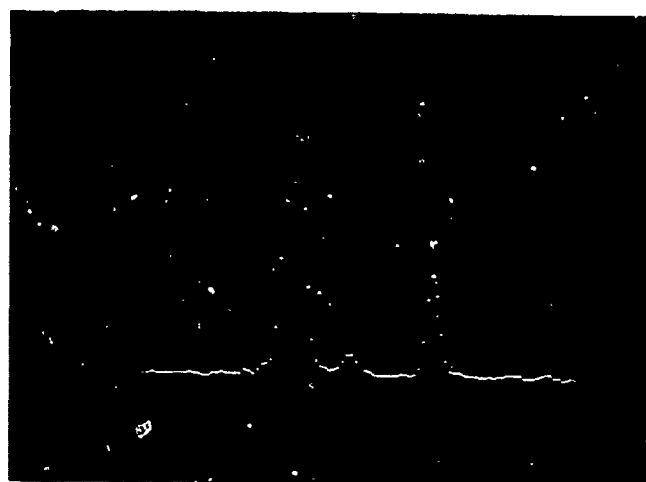
Figure 16. Modified Boltzmann Plot for H_2 Spectrum Shown in Figure 14
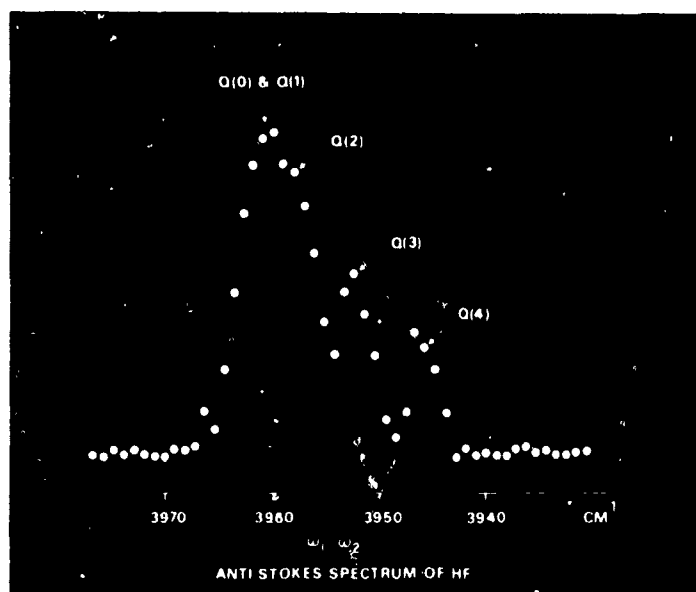
a) $T \approx 295° K$
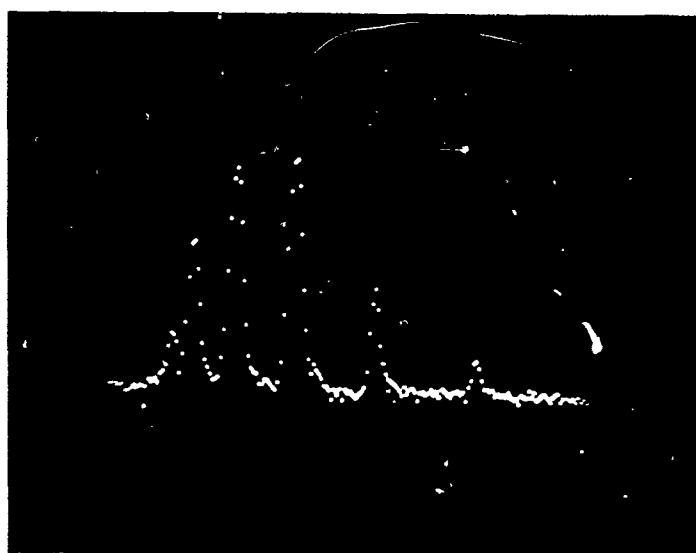

b) $T \approx 415° K$

Figure 17.   Anti-Stokes Spectrum of H_2 Taken
at Two Temperatures

(a)

(b)

Figure 18. Anti-Stokes Spectrum of HF Taken With
(a) Old Grating (600 g/mm Blazed at
17°), and (b) New Grating (632 g/mm
Blazed at 51°)

The lower spectrum (in Fig. 18) is the HF anti-Stokes spectrum taken with the new grating. The marked improvement in resolution in the lower spectrum is quite obvious.

Next, high-resolution anti-Stokes spectra of the HF molecule were generated along with those of the reference gas to permit estimation of gas temperature using the single-pulse CARS technique. A typical set of these spectra is shown in Fig. 19. Because of the difficulty encountered in tuning the dye laser to the appropriate Stokes wavelength for HF either by varying the dye concentration or by mixing dyes, an intracavity prism (made from high-dispersion, dense flint glass) was incorporated into the dye laser as a broad-band tuning element. This arrangement yielded a dye-laser linewidth of ~ 45 Å, which was considered to be sufficiently broad for most of the experimental situations.

The rotational temperature of the HF gas was estimated from these spectra by following the procedure outlined earlier for the hydrogen molecule. The results obtained were rather perplexing, the average value calculated for the gas temperature being 415°K, which is substantially higher than the actual gas temperature (295°K). The reasons for this discrepancy are not yet clear. However, there is a possibility that the mathematical model used for fitting the data is inadequate in the case of the HF molecule, especially if the ordinarily neglected anisotropic contribution to the anti-Stokes signal is significant. This question merits further investigation.

Although many problems remain to be solved and there is still much room for improvement, the results obtained thus far which demonstrate the possibility of temperature measurement with a single laser pulse are very encouraging and, therefore, efforts should be made to perfect the technique.

2. PRESSURE DEPENDENCE OF INTEGRATED CARS INTENSITY

To the first-order approximation, the total intensity of the anti-Stokes radiation generated in a medium is proportional to the square of the number density of the resonant molecular species. However, this relationship holds
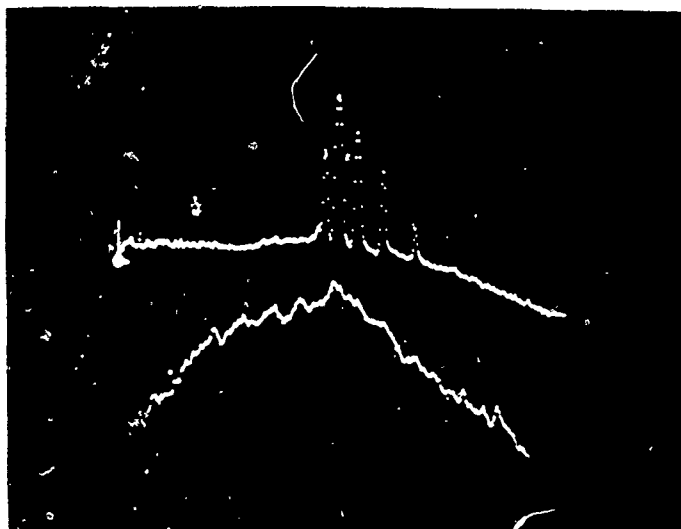
50

Figure 19. Single-Pulse Anti-Stokes Spectra of HF Sample Gas
(Upper Trace) and Reference Gas (Lower Trace)

51

only under a very restrictive set of conditions which are, more often than not, incompatible with the real environment in which the measurements must be made. Some of the factors which influence these conditions are: (1) media pressure and temperature, both of which affect the intensity through their influence upon the anti-Stokes linewidth; (2) laser-power level which perturbs the population distribution through the stimulated Raman process, etc. [21]; and (3) the contribution of the host gases of the media through their nonresonant third-order susceptibility. Since the exact manner in which these factors affect CARS intensity varies from one molecule to another, experimental determination of the parameters involved for all molecular species of interest is essential for the application of the CARS process to gas diagnostics.

Of the factors mentioned, the media pressure--both total and partial-- and the nonresonant contribution of the host gases are most prominent in their impact; consequently, these factors were investigated first in this program. For these investigations, the CARS system was operated in the narrow-band mode, the dye laser being tuned and line-narrowed by means of an interference filter (and sometimes a solid Fabry-Perot etalon also) as described in Section II-1. Since the dye-laser linewidth in this configuration is $\sim$ 15 cm^{-1} or 2 cm^{-1}, depending upon whether the etalon is used, it was generally possible to excite--according to the particular experimental objectives--all or some of the rotational levels that are thermally populated at room temperature.

Of the molecules studied in this program, all except hydrogen were excited by a 15-cm^{-1}-wide dye-laser line in order to ensure that the molecules in all rotational levels would contribute. In the case of hydrogen, a 2-cm^{-1}-wide dye-laser line exciting only the J=1 rotational level proved to be more practical in view of the wide separation between rotational levels. The anti-Stokes signals generated were detected by a photomultiplier, the output of which was integrated, amplified, and recorded. Because of the limited dynamic range of the detection electronics employed, it was necessary to attenuate the anti-Stokes signals properly by means of neutral-density filters prior to detection. The insertion of these filters in front of the

sample cell to attenuate the pumping laser beams rather than the generated anti-Stokes beam led to a rather poor measurement with large scatter in the data. It was concluded that the poor surface figures of the neutral-density filters (~ 5 λ as quoted by the manufacturer) "scramble" the laser beams and destroy the spatial coherence which is so necessary for predictable beam behavior.

The slits of the monochromator were maintained sufficiently wide to permit a complete collection of desired anti-Stokes lines (or a band). The use of an exciting Stokes linewidth which is broader than that of the anti-Stokes lines, coupled with wide-band detection, ensures the measurement of integrated intensity of the lines.

In the following paragraphs, the results of the investigations on methane (CH_4), nitrogen (N_2), carbon monoxide (CO), and hydrogen (H_2) molecules are presented.

A. Methane

Figure 20 shows the partial-pressure dependence of the anti-Stokes intensity of methane gas obtained in the manner described above. The data represented by the upper line were obtained for pure methane and those represented by the lower line were for a mixture with nitrogen gas under a fixed total pressure of 700 Torr. It should be noted that the data can be represented by a straight line. A least-squares fit of these data to $\log I_t = a_1 \log p_r + \log a_0$ (where p_r is the gas pressure and I_t is the integrated CARS intensity) yielded for the slope (a_1) a value of 1.82 and 1.97 for the pure and the mixed gas, respectively. The value of 1.97 for the mixed gas is well within the experimental error of the theoretical value (= 2.0). However, in the case of the pure gas, the slope is considerably smaller. This decrease in slope is due to pressure broadening of the anti-Stokes linewidth. Because of the severe overlap among all Q-branch rotational lines of the methane anti-Stokes spectrum, the usual linear pressure dependence of the linewidth for pressure-broadened isolated lines does not hold in the case of methane gas, although the linewidth still increases monotonically with pressure.

53
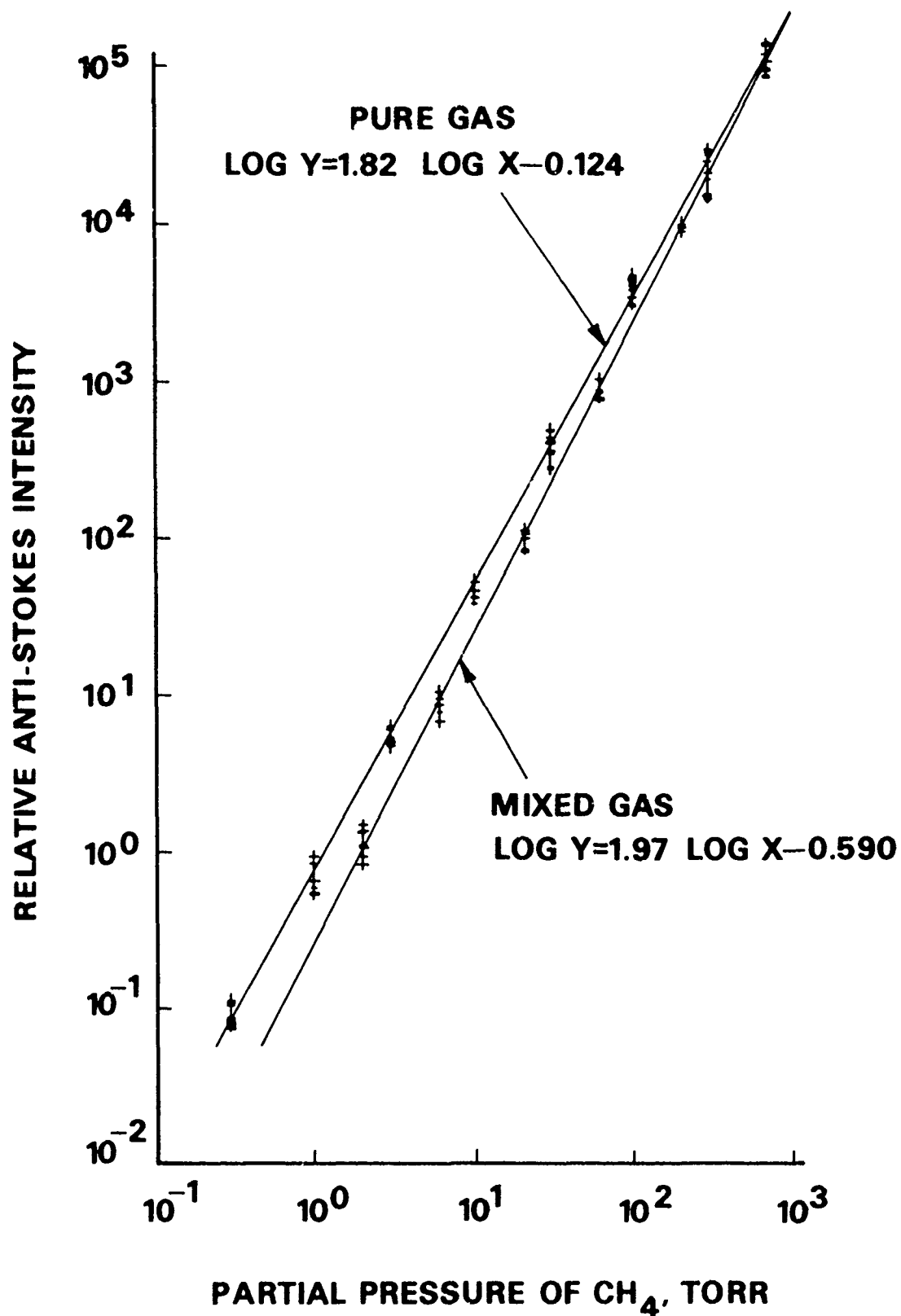
Figure 20. Partial-pressure Dependence of Anti-Stokes Intensity of
Gas: Upper Line for Pure Methane; Lower Line for a Mixture
with Nitrogen under a Constant Total Pressure

54

From experimental results such as those in Fig. 20, a measure of the effect of pressure upon linewidth can be calculated. Since the linewidth is a function of the pressure, Eq. (52) can be written

$$I_t = K_1 F(T) \frac{p_r^2}{\Gamma_{eff}(p_t)} \tag{55}$$

where the dependence of Γ_{eff} upon the total pressure, p_t, is explicitly indicated.

In order for Eq. (55) to represent the experimental data given by

$$\log I_t = a_1 \log p_t + \log a_o \tag{56}$$

the effective linewidth must be given by

$$\Gamma_{eff}(p_t) = \frac{K_1 F(T)}{a_o} p_t^{2-a_1} \tag{57}$$

Since the parameter a_1 generally depends upon gas temperature as well as molecular species, a "pressure-broadening parameter" $\eta(T)$ can be defined such that

$$\eta(T) = 2 - a_1 \tag{58}$$

For gases with $\eta(T) = 0$, there is no broadening at all; if $\eta(T) = 1$, the lines undergo ordinary pressure broadening that is proportional to the total gas pressure. For methane η (300°K) is calculated to be 0.18. Substitution of Eqs. (57) and (58) into Eq. (55) yields

$$I_t = a_o p_t^{-\eta(T)} p_r^2 \tag{59}$$

55

Equation (59) can be used for determining gas concentrations through integrated CARS-intensity measurements, once the parameter $\eta(T)$ is known. Although the temperature dependence of $\eta(T)$ has not been investigated experimentally during this program, it has been shown that the Raman linewidth of H_2 molecule increases with temperature [25]; therefore, it is important to determine the temperature dependence of $\eta(T)$ for all molecules of interest for the application of CARS to combustion diagnostics.

B. Nitrogen

Figure 21 shows the pressure-dependence of the CARS intensity of nitrogen gas. As in the case of methane, measurements were made for both pure and mixed gas. The calculated values of the slope of the lines shown in the figure were 1.16 and 1.95 for the pure gas and the mixture with helium gas, respectively. The value of the broadening parameters is

$$\eta(300°K) = 0.84 \text{ for } N_2$$

The fact that the broadening parameter of nitrogen is greater than that of methane is consistent with the fact that the line-spacing of nitrogen is greater than that of methane. This can be more readily understood by observing that as the degree of overlap of rotational lines increases, the net effect of pressure broadening upon linewidth decreases.

C. Carbon Monoxide

The pressure dependence of the anti-Stokes radiation of the CO molecule was measured in both the pure gas and in a mixture with other gases. In Section II, it was shown that the integrated intensity is given by

$$I_t = K_1 \left\{ P_r^2 \frac{F(T)}{\Gamma_{eff}} + P_r P_{or} \left[\sum_J \sum_K \frac{\Gamma H_{JK}(T)}{(\omega_J - \omega_K)^2} \right] + K_2 \right. \tag{60}$$
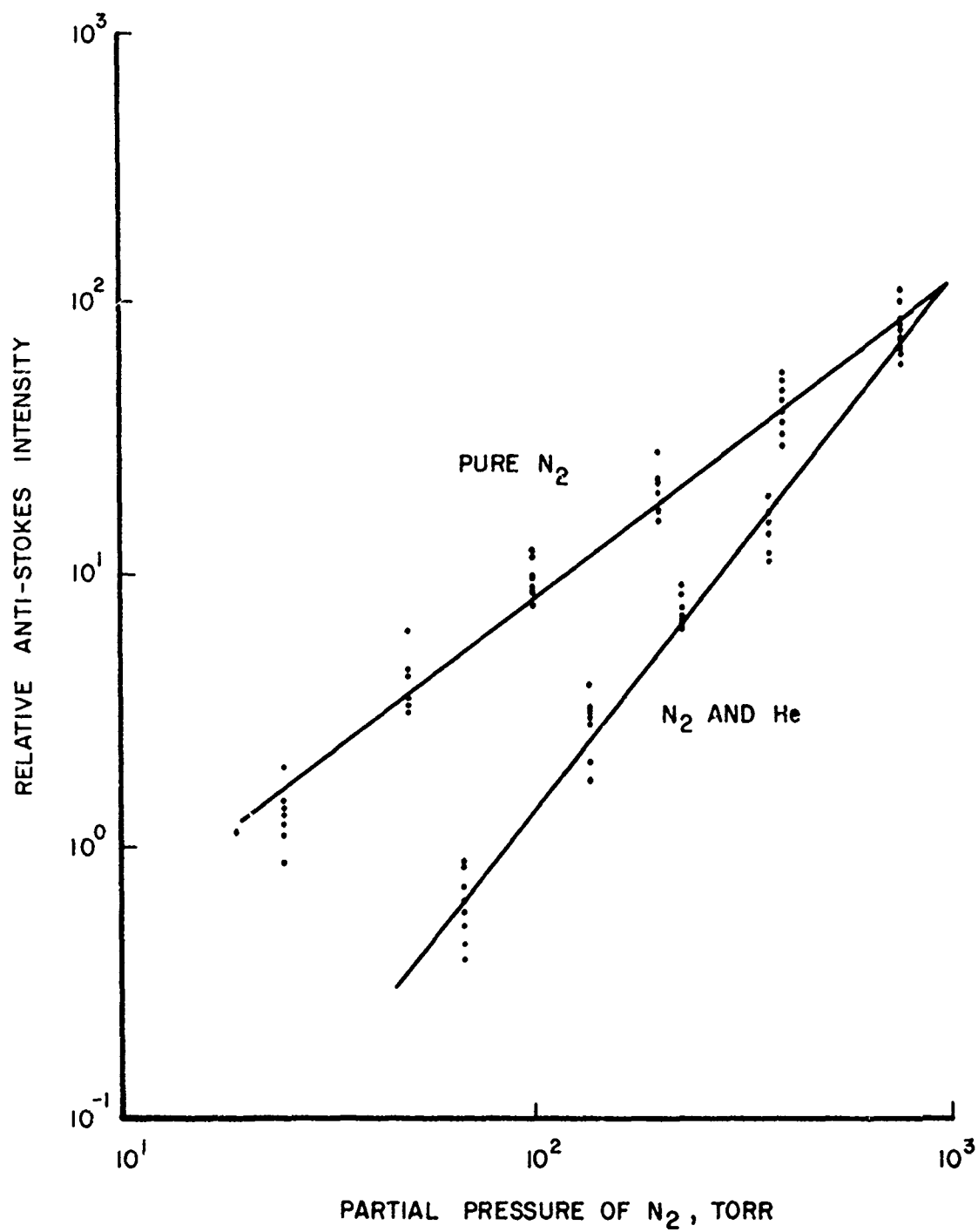
Figure 21. Pressure Dependence of Anti-Stokes Intensity of N_2

In the case of the pure gas, the second and third terms in Eq. (60) are negligible as compared to the first; thus, only the resonant term in the equation contributes to the anti-Stokes intensity. The result of the measurements for this case are shown in Fig. 22 (Line A). The slope of the line was calculated to be 1.21 (least-squares fit), which yields

$$\eta(300°K) = 0.79 \text{ for CO}.$$

This value for CO may be compared to 0.84 for N_2 and 0.18 for CH_4.

On the other hand, a mixture with helium gas under a fixed total pressure (760 Torr) yielded 1.96 for the slope of the line, as shown in Fig. 22 (Line D). In this case, the anti-Stokes intensity follows the square-law dependence more rigorously since the fixed total pressure keeps the linewidth constant, while the contribution from the nonresonant susceptibility of helium is negligibly small.

A good example of the manner in which the three terms in Eq. (60) contribute to the anti-Stokes intensity can be seen in the measurements made with the mixture of CO and N_2 shown in Fig. 22 (Line B). In the partial-pressure region approximately above 100 Torr, the experimental data can be represented by a straight line having a slope of 1.96. This is the region in which the first term in Eq. (60) is predominant and, therefore, the square law holds in this region. For CO partial pressures below 3 Torr, the third term is predominant and, thus, the anti-Stokes intensity is more or less independent of CO partial pressure. At intermediate pressures, the second term is the main contributing factor, and the anti-Stokes power is directly proportional to CO partial pressure.

When H_2 was used as the buffer gas for a mixture with CO, results were similar to those obtained for the CO + N_2 mixture, except for the difference in magnitude of the nonresonant contribution (Line C in Fig. 22). The difference in the level of nonresonant contribution from the N_2 gas and H_2 gas can be understood by recognizing that the vibrational frequency of CO is much closer to that of N_2 than to that of H_2.
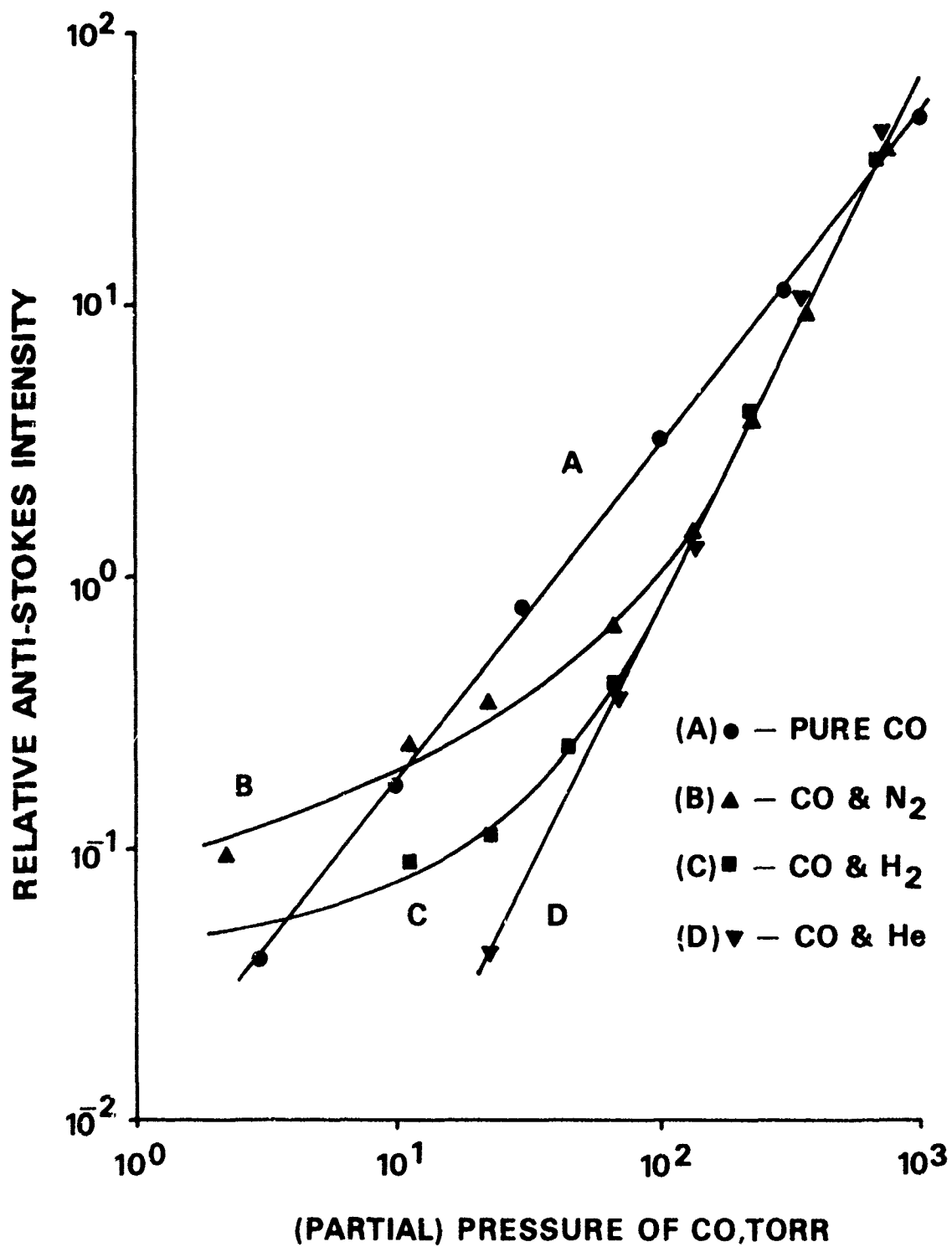
Figure 22. Partial-pressure Dependence of Anti-Stokes Intensity of CO

In order to verify the dependence of the anti-Stokes power upon the total pressure of the medium, a slightly different experiment was carried out using a mixture of CO and N_2. In this experiment, the partial pressure of CO was kept constant at 75 Torr, and the total pressure was varied from 75 to 500 Torr by adding N_2 gas to the CO cell. The anti-Stokes power was measured as a function of total pressure. As expected, the power decreased as the total pressure was increased as shown in Fig. 23. This result is consistent with the value of the broadening parameter $\eta(T)$ obtained from the measurements shown in Fig. 22.

Up to this point, the discussion has been limited to the pressure range in which pressure broadening is the primary line-broadening mechanism. In order to investigate the pressure-intensity relationship in the Doppler-broadened region, measurements on pure CO gas were extended to include a lower-pressure region than that covered in previous measurements. The results of these measurements are shown in Fig. 24. As can be seen from the figure, the anti-Stokes radiation was measured at pressures as low as 0.1 Torr of CO as a result of the increased ruby power and other improvements made in the system. Previously the lowest pressure measured was ~ 10 Torr. A feature in this figure that had not been observed in our earlier measurement is the change in slope of the line representing the data at ~ 20 Torr. Furthermore, the slope for the region from 1 to 20 Torr is ~ 2.0, with the exception of the extreme lower end.

The data for the region from 1 to 10 Torr can be represented by a line having a slope of 2.0, as indicated in the figure. This is the manifestation of the Doppler nature of the line broadening in this region. The measurements at pressures below 1 Torr do not follow the same line although, in principle, they should. This deviation could be attributed mainly to the nonresonant contribution from the sample cell windows and the air outside the cell.

D.   Hydrogen

The hydrogen molecule is one of the most extensively investigated molecules in Raman scattering experiments, particularly in connection with
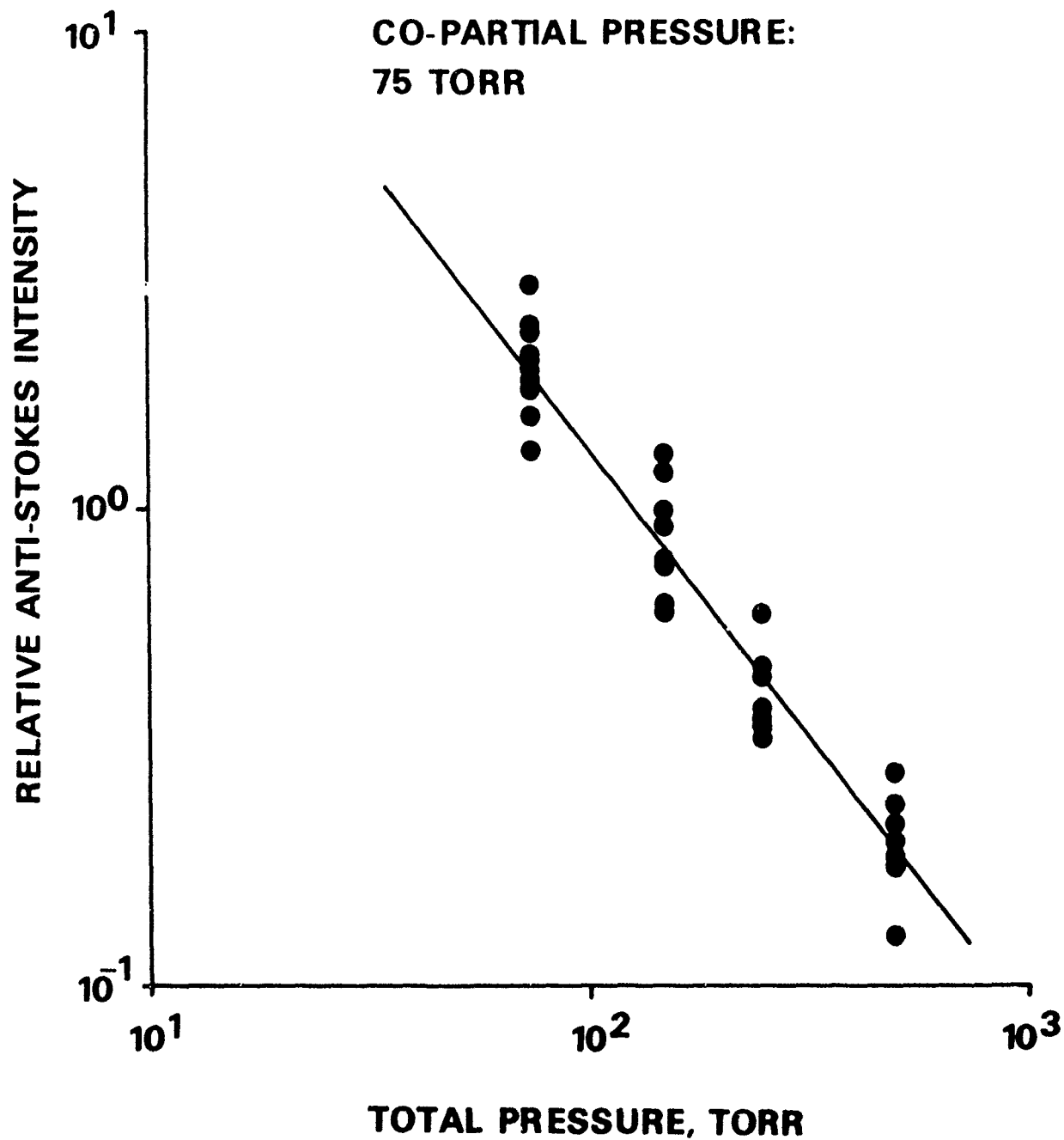
Figure 23. Total-Pressure Dependence of Anti-Stokes Intensity of CO. Partial pressure of CO was kept constant at 75 Torr.
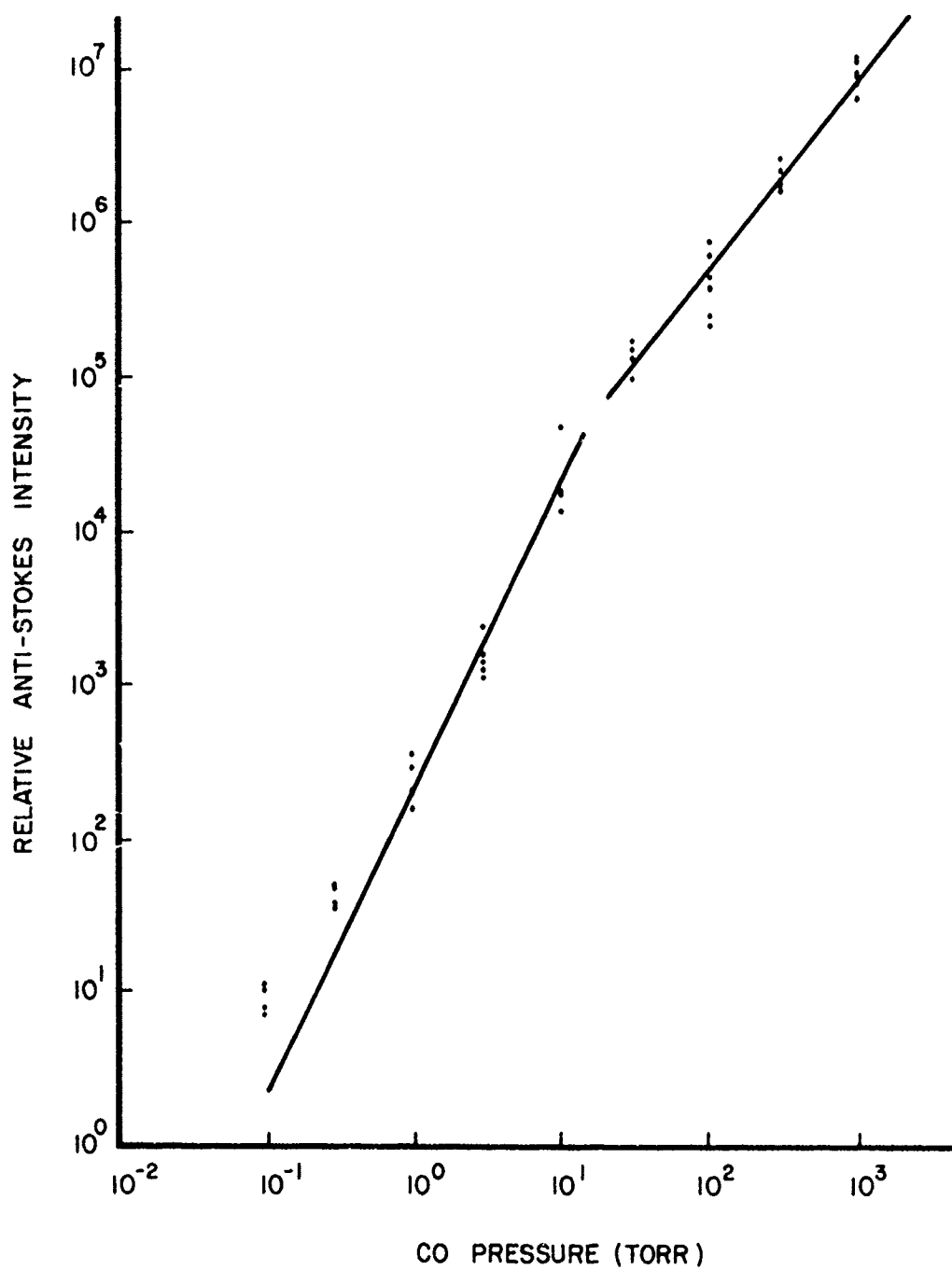
Figure 24.   Pressure Dependence of Anti-Stokes Intensity of CO

the stimulated Raman effect. It is also one of the most interesting molecules because its spectral lines exhibit a strong collisional-narrowing effect [26]. The CARS intensity is affected accordingly, and the experimental results bear out this fact. Figure 25 shows the pressure dependence of the CARS intensity of a pure hydrogen gas. As pointed out earlier, the integrated intensity of only the $Q(1)$ line rather than the whole Q-branch was used in this experiment. In the low-density region below $\sim 1/2$ amagat, the intensity obeys the square law quite rigorously, demonstrating the Doppler nature of the lineshape. In the high-density region above ~ 10 amagat, the intensity becomes directly proportional to the density, signifying the pressure-broadened linewidth. In the intermediate density region, however, the intensity has a cubic dependence upon density preceding the monotonic transition to a linear dependence. It is in this region where the collisional narrowing of the anti-Stokes lines takes place.

A similar measurement using mixtures of H_2 and He was also made, and the results are shown in Fig. 26. Although the partial pressure of H_2 remains fixed at 20 Torr, the integrated CARS intensity exhibits an anomalous increase in the mid-pressure region.

In order to investigate the effects of different buffer gases upon the line-narrowing phenomenon, the measurement was repeated using other buffer gases (N_2, CH_4, and He) in the pressure region where the line was narrowest (~ 5 amagat). The results showed that there is no significant difference among the various buffer gases.

Since the integrated intensity of an anti-Stokes line is inversely proportional to the linewidth and the linewidth at low pressures can be approximated by a Doppler linewidth, the intensity data can be converted into linewidth data at various pressures. Figure 27 shows the result of this type of calculation. In calculating the linewidth, a Lorentzian lineshape was assumed throughout the entire pressure range, although this assumption is, in fact, valid only in the pressure-broadened region above ~ 20 atm. At pressures below ~ 0.1 atm, it is indeed a Gaussian; and in the mid-pressure range, it is neither Lorentzian nor Gaussian [27,28], despite the initial theoretical predictions of a Lorentzian lineshape [26]. For these
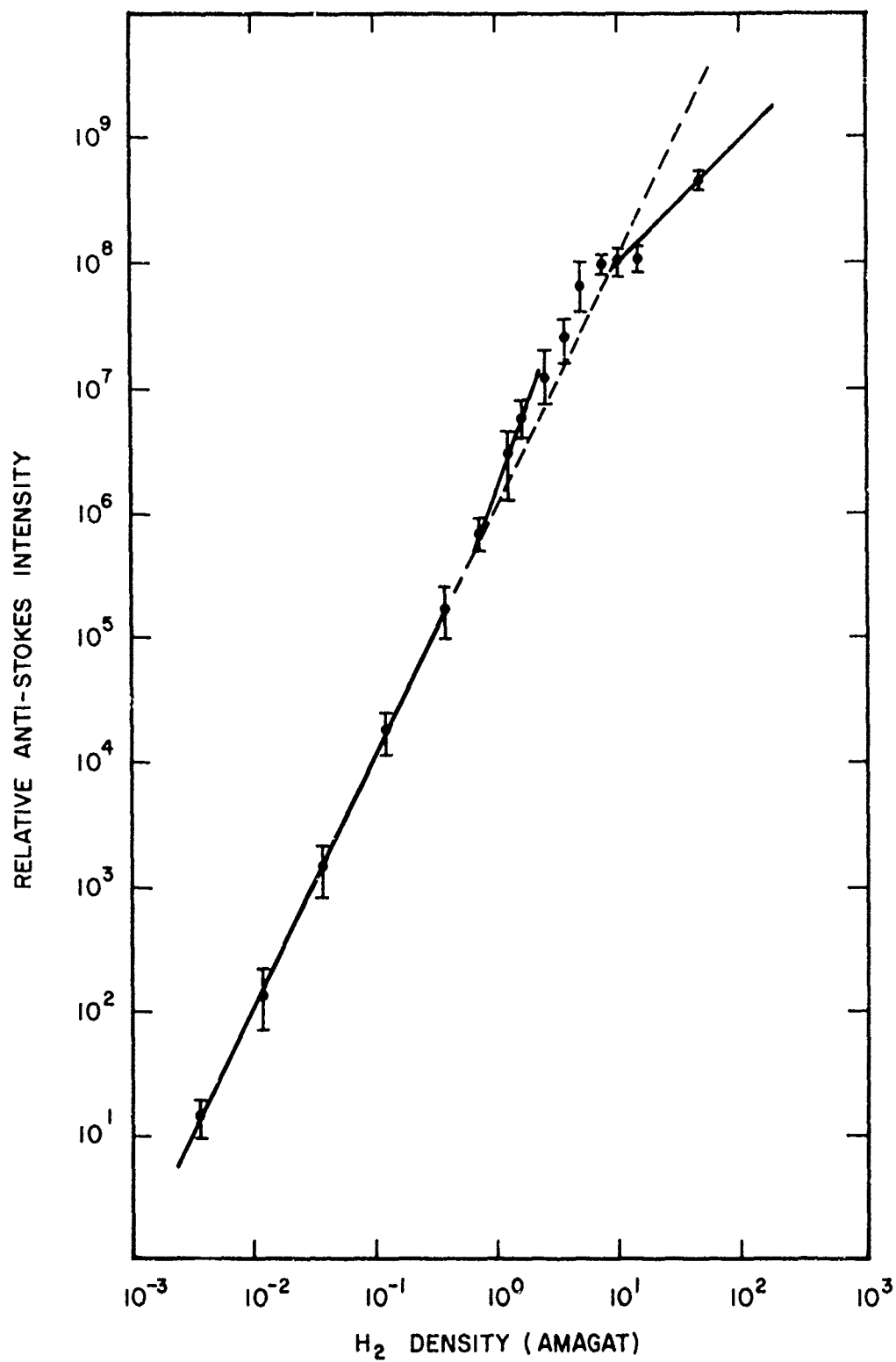
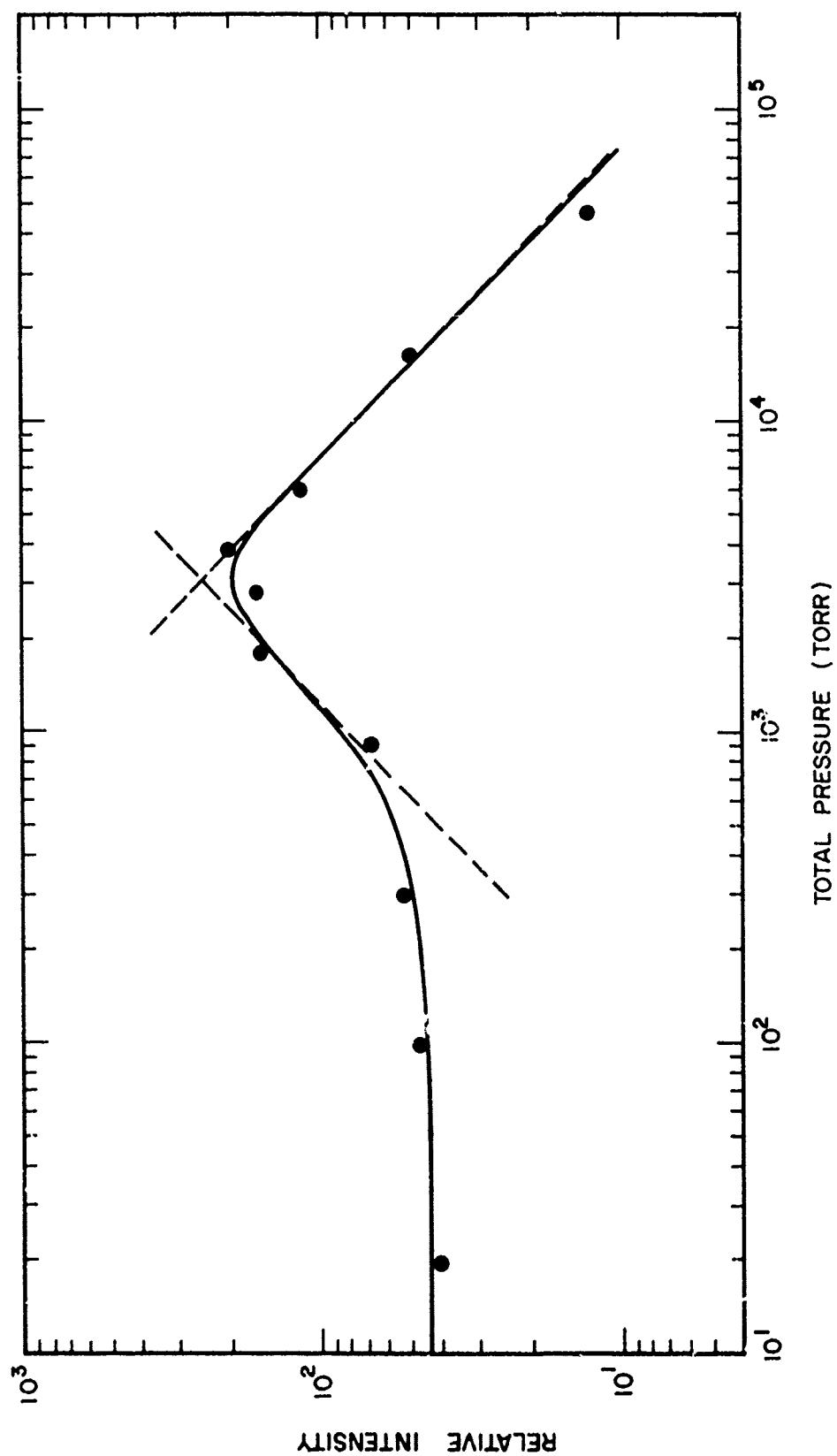Figure 25. Pressure Dependence of Anti-Stokes Intensity of Q(1) Line of Hydrogen Molecule

Figure 26. Integrated Anti-Stokes Intensity of Q(1) Line of H_2 as a Function of Total Gas Pressure (Pressure was varied by adding He gas while maintaining the H_2 partial pressure constant at 20 Torr.)
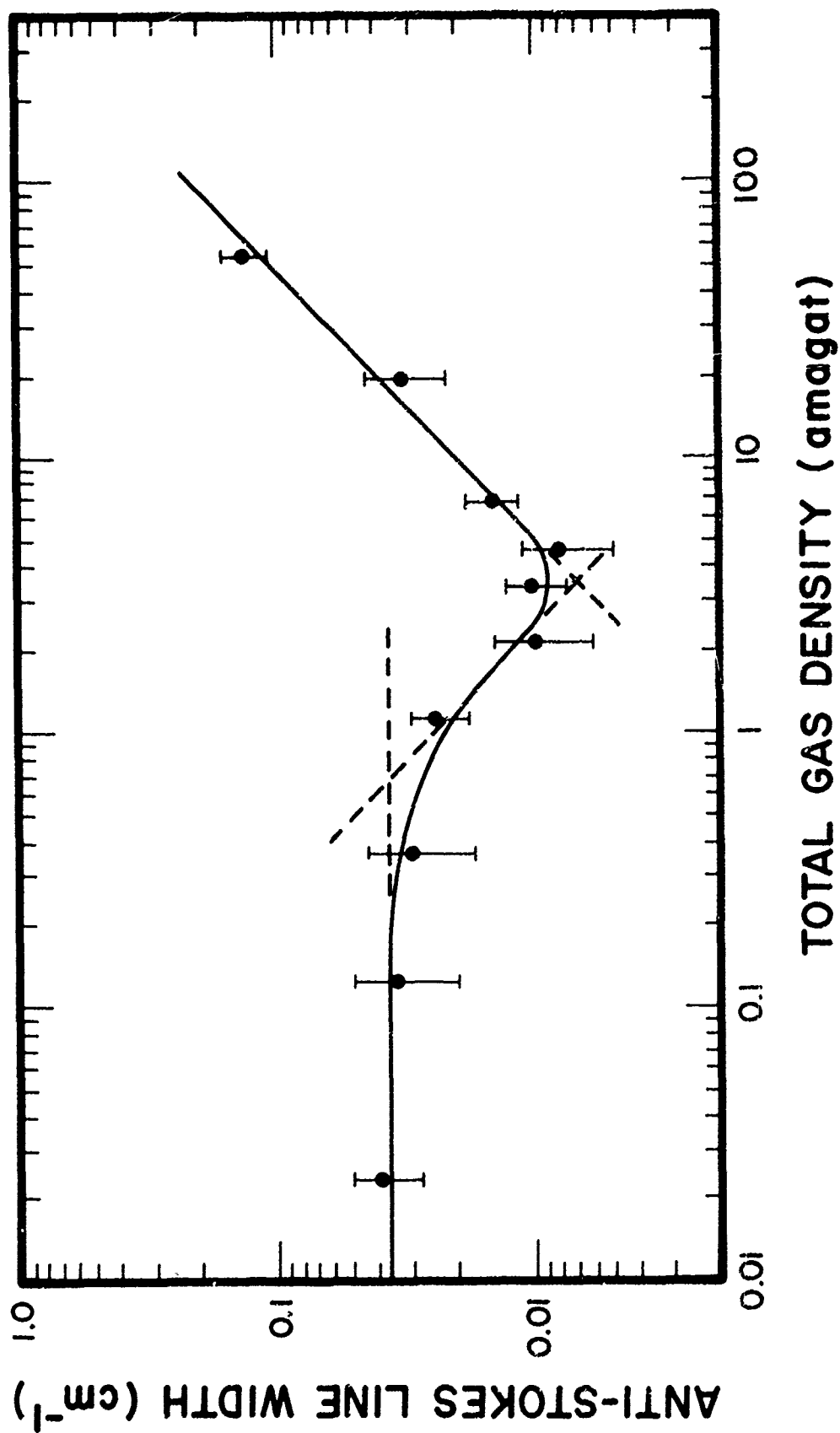
Figure 27. Linewidth of Q(1) Line of H_2 as Function of Density as Determined through Anti-Stokes Intensity Measurements Shown in Fig. 26

reasons, the linewidth calculations in Fig. 27 represent only tentative results and should be interpreted accordingly. In a rigorous treatment, the effect of lineshape as well as linewidth in various pressure regions should be included. It is interesting to note that the calculated linewidth is in good agreement with the values directly measured through backward-stimulated Raman scattering [29]. The experimental data available on the pressure at which the minimum linewidth occurs are only marginally consistent. The present results compare favorably with those of DeMartini, et al. [27] and less well with those of Lallemand, et al. [29].

3. TWO-WAVELENGTH DYE LASER AND SIMULTANEOUS
    DETECTION OF CO AND N_2

A two-wavelength dye laser was designed and fabricated on a trial basis. Figure 28 is a schematic diagram of two slightly different cavity configurations that were used to generate two colinear independently tunable laser lines from a single dye laser.

Although the first and second configurations utilize three and four mirrors, respectively, they operate in a similar manner. Common to these configurations is the employment of one "leg" in the cavity consisting of a mirror (M3) and a dye cell containing an active medium and two other "legs" in the cavity consisting of a mirror and an intra-cavity interference filter (M1 + IF1 and M2 + IF2). The two "legs" containing interference filters are coupled to the "leg" containing the dye cell by means of a 50/50 beamsplitter; this forms a semi-independent laser cavity for each wavelength. Wavelength tuning is accomplished independently by tilting individual interference filters with respect to the optic axis of the dye laser. The only difference between the two configurations shown in Fig. 28--except for the obvious difference in the relative beam directions between the pump and the dye laser--is the presence of a fourth mirror (M4) in the second configuration. This mirror (M4) provides an additional feedback of photons within the cavity and thus is expected to increase the cavity-quality factor.

M2 (100% R)

IF2 (λ_2)

M3 (100% R)

BS (50/50)

PUMP

MI (100% R)

IFI (λ_i)

DYE CELL

DYE LASER (λ_1 AND λ_2)

(a)

M2 (100% R)

IF2 (λ_2)

M3 (35% R)

BS (50/50)

PUMP

MI (100% R)

DYE LASER

(λ_1 AND λ_2)
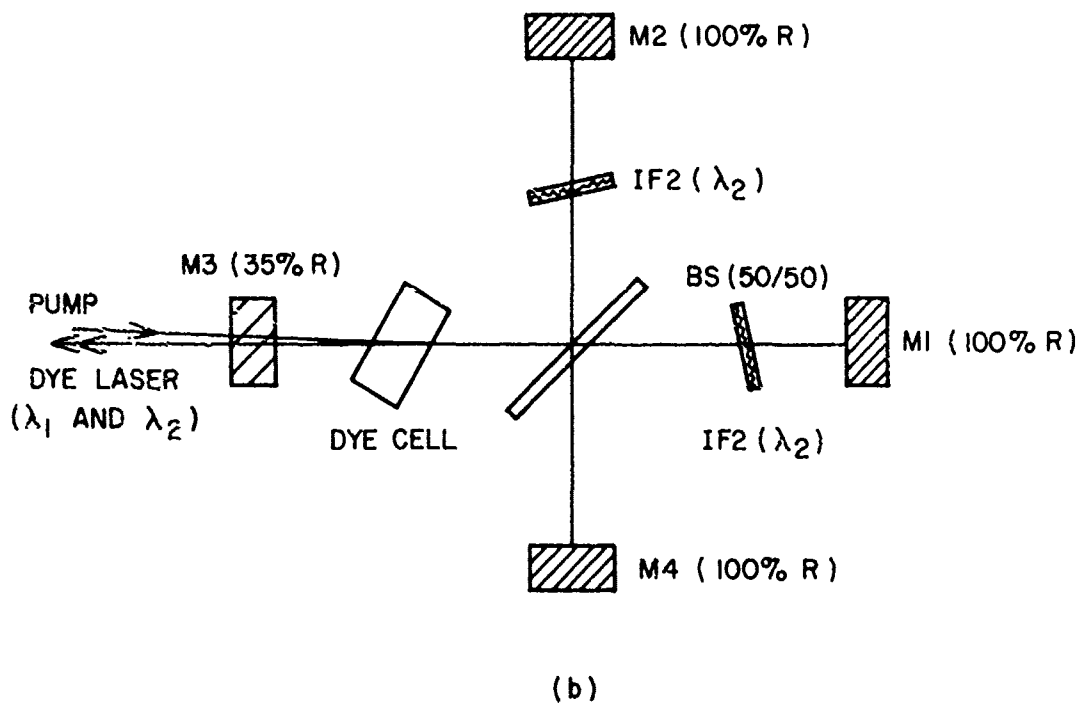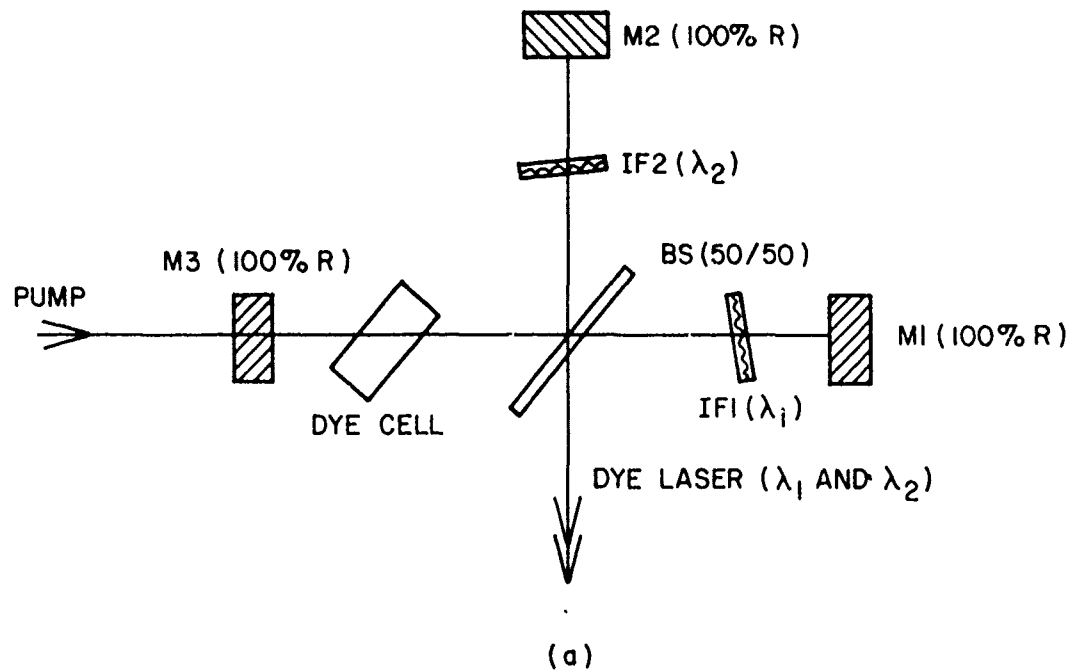
DYE CELL

IF2 (λ_2)

M4 (100% R)

(b)

Figure 28. Schematic Diagram of Two-line Dye-laser Design (a) Three-mirror Cavity Configuration; (b) Four-mirror Cavity Configuration

In reality, it was found that these configurations work equally well. This is not to say that there are no shortcomings with these designs. One of the shortcomings lies in the fact that approximately one-half of the dye-laser power is lost within the cavity when one wavelength component, say λ_1, enters the "leg" tuned to λ_2 and vice versa. Although this loss can be prevented through the use of polarization-sensitive beamsplitters, as was the case in Ref. [30], the output beams at λ_1 and λ_2 become cross-polarized. Since the Raman effect is most efficient for parallel polarization, the cross-polarization was judged to be unacceptable. Another problem lies in the competition between the two laser lines. This competition arises because both laser lines deplete the molecular population of the laser dye in the common upper level. The competition was a problem even with a design that incorporated spatial separation in the active medium between two wavelength components [15]. As a result of this competition, the relative intensities of the lines become critically dependent upon the round-trip gain of each laser line. Despite these shortcomings, the dye laser was operated simultaneously at two wavelengths, and the lines were tuned independently. The maximum spectral separation between the two lines was ~ 200 Å using Dye No. 17 (Candella Corp.), and the minimum was as small as two times the linewidth (~ 20 Å with interference filters only).

Figure 29 shows the anti-Stokes spectra of CO at 6044 Å and N_2 at 5976 Å (upper trace) along with the reference spectrum (lower trace) detected simultaneously using the two-line dye laser described above. This is a demonstration of only one of the potential applications of the two-wavelength dye laser. Another possibility is the simultaneous detection of two vibration-rotation Raman bands of a single molecule. This type of experiment would allow the temperature measurement of gases in which the rotational structure of the Raman bands is not resolved. Since most molecules—with the exception of a few light ones (H_2, D_2, and HF)—fall into this category, simultaneous detection of two vibration-rotation bands may prove to be the most practical means of temperature measurement.
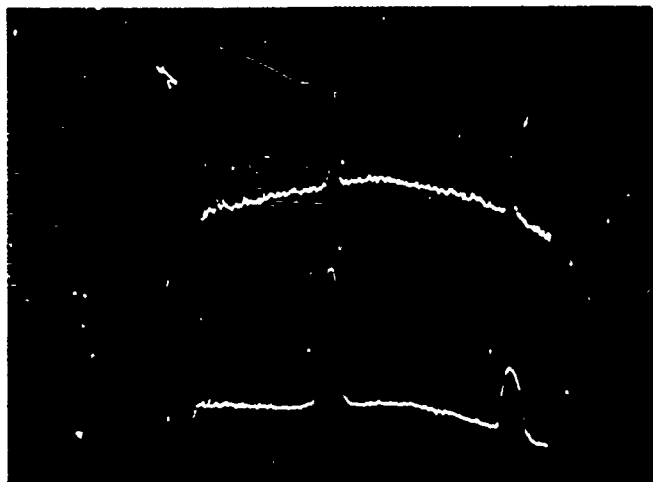
Figure 29.   Anti-Stokes Spectra of CO at 6044 Å
             (Right) and N_2 at 5976 Å (Left)
             Detected Simultaneously Using the
             Two-Line Dye Laser Shown in Fig. 28.
             Upper trace is for the sample, and
             lower trace is for the reference.

4. EFFECT OF MEDIA TURBULENCE*

In developing the CARS technique for applications to the diagnostics of
combustion and other processes, the turbulence of the media and its impact
upon the CARS process in general is of great concern. Thus, it is important
to understand the effect of media turbulence and to control the experimental
conditions so as to minimize the adverse impact which the media turbulence
might have for the CARS technique. Experiments were designed and carried
out in order to investigate the effect of media turbulence upon laser-beam
propagation and the CARS process.

For these investigations, a cold jet of helium and air was used as
a turbulence generator. The cold-jet apparatus consisted of two concentric
stainless steel tubes having 1/16-in. wall thickness, one having 1/4 in. ID
and the other, 7/8 in. ID. A turbulent gas mixture was formed by flowing
helium gas and compressed air through the inner and outer tube, respectively,
and letting the gases mix upon exit from the jet. The flow rate of the
gases was controlled by incorporating a sonic nozzle into each of the gas
lines and maintaining a constant pressure head across the nozzle.

Figure 30 shows a typical CARS intensity profile of the nitrogen gas
from the jet taken diametrically 3.5 cm above the jet. The gas pressures
used for this measurement and all subsequent experiments were 50 psi for
air and 39 psi for helium. As expected, the fluctuation in intensity is
greatest in the central region of the jet stream where turbulence is
expected to be greatest. Although the mass-spectrometer measurement was
made for oxygen, it was tacitly assumed that the relative nitrogen-
concentration profile was the same as that of oxygen in air for the
comparison of the data obtained in these two experiments.

---

*This portion of the work on turbulence effects was carried out
in cooperation with Dr. F. Chen of the Southeastern Center for
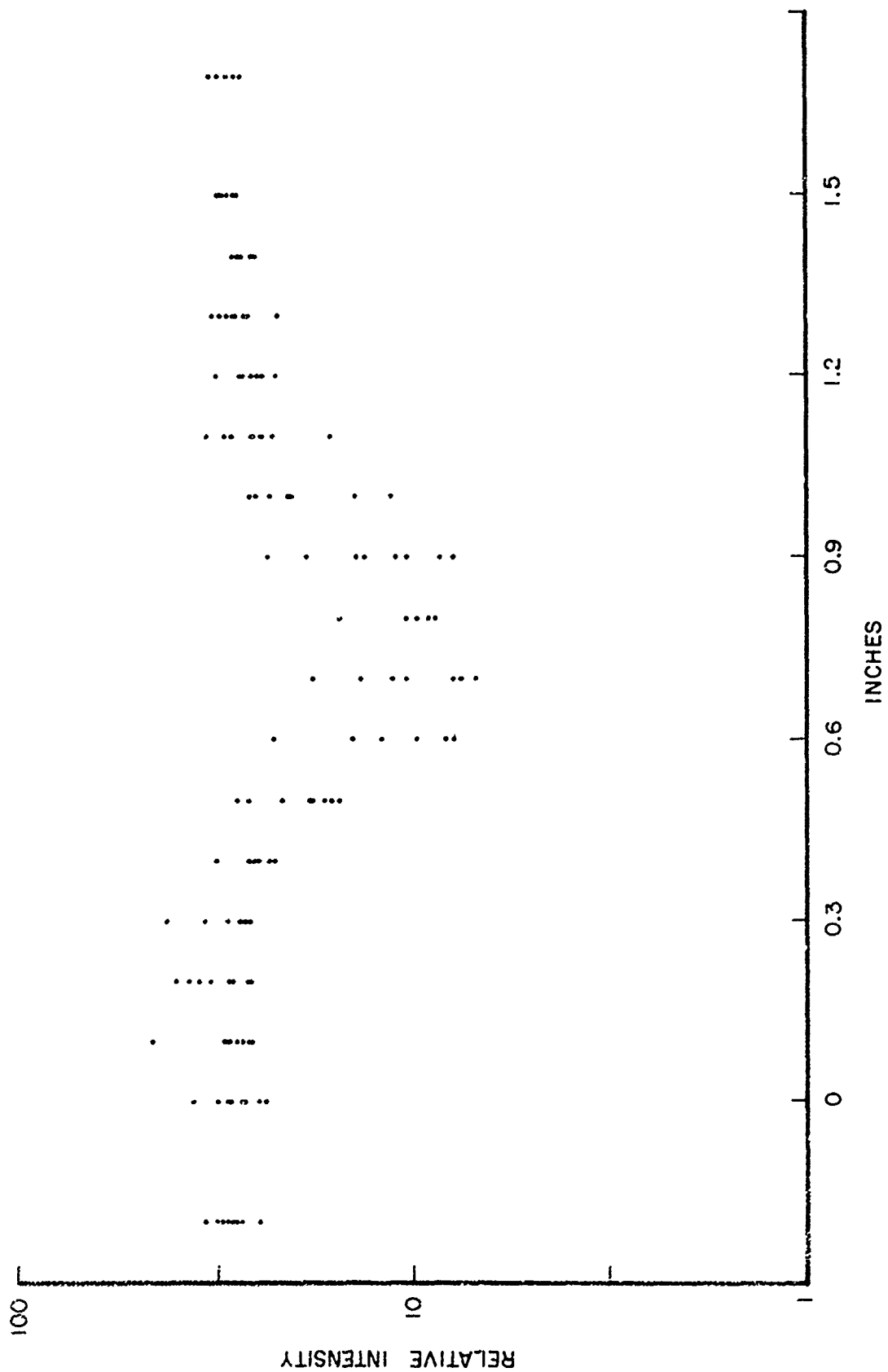Electrical Engineering Education, Inc.

Figure 30. CARS Intensity Profile of N_2 Gas from a Helium-Air Jet

Figure 31 shows the profile of the average nitrogen concentration calculated from the results shown in Fig. 30, along with a mass-spectrometer recording of the oxygen-concentration profile for the same jet. It should be pointed out that the CARS data were properly averaged, normalized, and fitted to the mass-spectrometer recording. The overall agreement between the two sets of data is quite good.

Because of suspicion that turbulence may cause defocusing of the laser beams--in which case the CARS intensity would be greatly affected--the CARS measurements were repeated with the positions of the reference cell and the jet interchanged (See Fig. 1 for the schematic of the experimental system. The jet was used in place of the sample cell in these experiments.). The nitrogen profile obtained in this configuration was exactly the same as that obtained in the previous measurement. These results indicate that the presence of turbulence in the focal region of the laser beams does not cause a reduction of the intensity of the anti-Stokes radiation generated in a cell placed subsequent to the turbulence-generating He-air jet. On the other hand, the placement of the jet in a collimated section of the laser beams greatly reduced the CARS intensity generated in the subsequent stages. One significant conclusion that can be drawn here is that the turbulence generated from the jet affects the CARS process when such turbulence is placed in a collimated beam path but not when it is placed in the focused region, at least in the configuration used for the present measurements.

In an attempt to characterize the turbulence effects in a more systematic manner, a series of experiments was carried out on the helium-air jet using a He-Ne laser. Schematic diagrams of the experimental setup used are shown in Fig. 32. In the first experiment the He-Ne laser beam (3 mm in diam.) was chopped (1 kHz) and directed through the region of turbulence in collimation before being detected by a PIN diode and displayed on an oscilloscope (Fig. 33(a)]. When the He-air jet was shut off (i.e., no turbulence), the signal waveform was nearly sinusoidal, as shown in Fig. 33(a). However, when the jet was turned on, the signal fluctuated randomly, as shown in Fig. 33(b). This clearly demonstrates the susceptibility of collimated beams to media turbulence. In the second experiment, the He-Ne laser beam
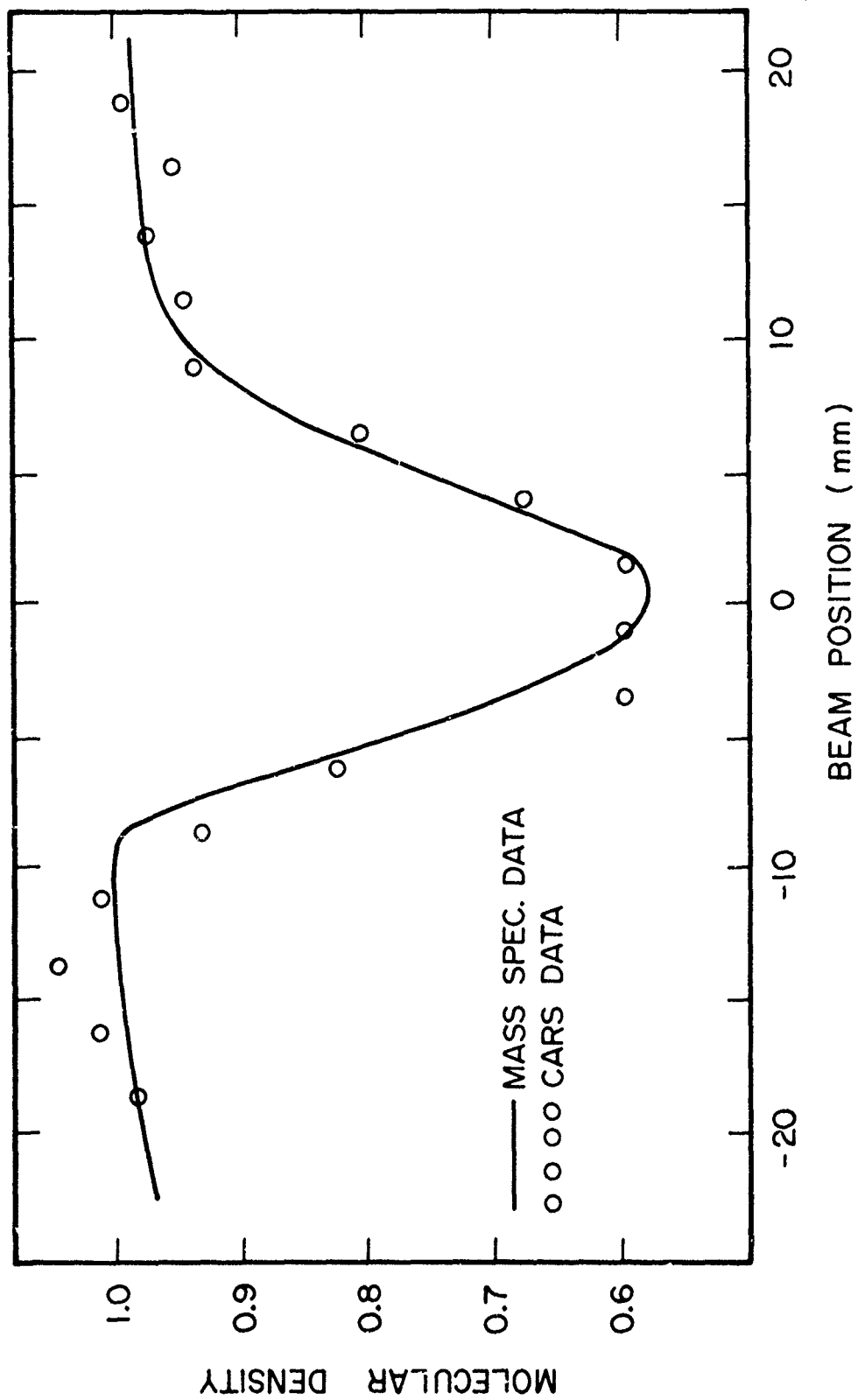
Figure 31. Comparison of Density Profile Calculated from the CARS Data (Circles) With That Obtained from the Mass-Spectrometer Measurement (Solid Curve)
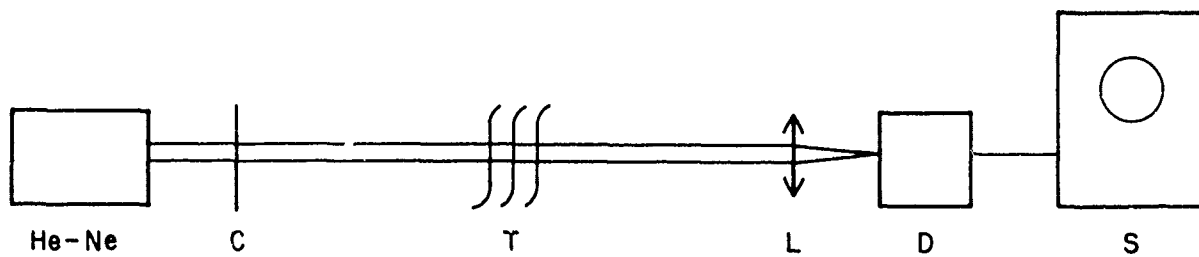
(a)
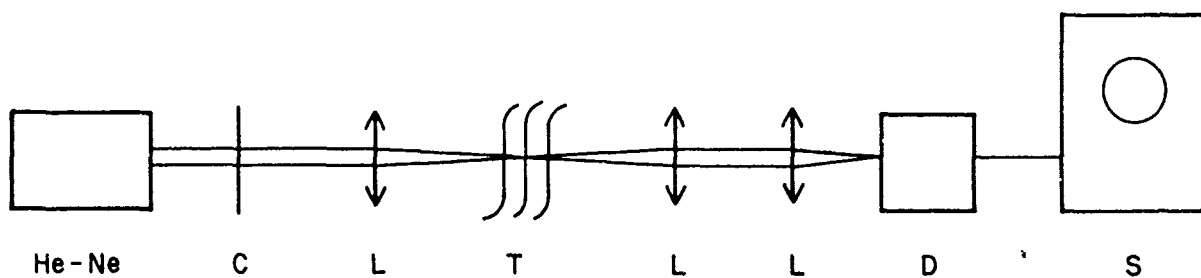
(b)
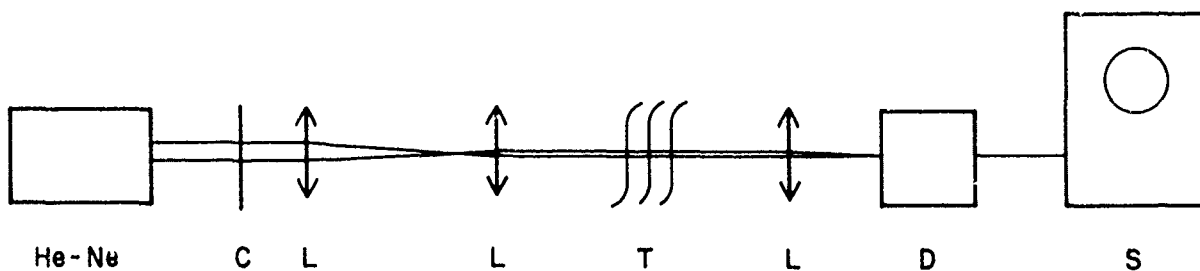
(c)

Figure 32. Schematic Diagram of Experimental Systems for Study of
Effect of Turbulence Upon Laser-Beam Propagation
(C ≡ Chopper, T ≡ Turbulent Jet; L ≡ Lens, D ≡ PIN-Diode
Detector, and S ≡ Scope)

75
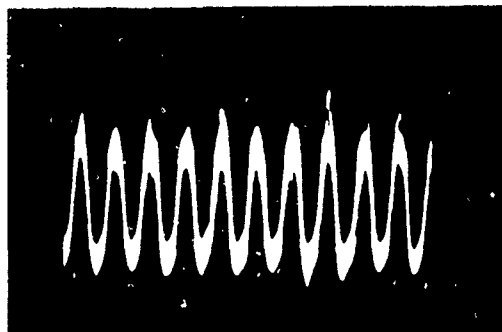
(a)
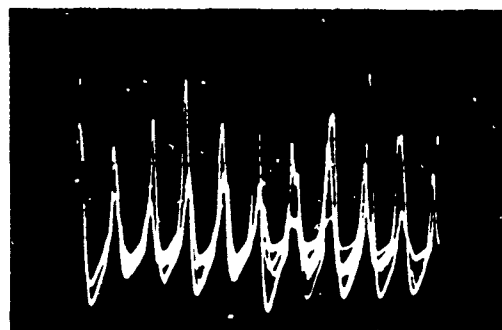
(b)

Figure 33. Oscilloscope Trace of Collimated He-Ne Laser
Beam Intensity as Monitored by a PIN-Diode
Detector, Without (a) and With (b) Turbulence
in the Beam Path.

76

was focused into the turbulent region by means of a simple lens (f.l. = 12.5 cm) and was collimated afterward. In this case the beam was observed to be unaffected by the turbulence, maintaining the near sinusoidal waveform even while the jet was on. In order to explore the possibility that the smaller beam size within the turbulent region might have been the critical factor in minimizing (or eliminating) the effect of turbulence, the third experiment was performed. The He-Ne laser beam was reduced to ~ 500 μ in diam. by means of a pair of lenses (f.l. = 70 and 12.5 cm) and directed through the turbulent region in collimation as in the first experiment. Despite the reduction in beam size, the laser beam was observed to have been affected by the turbulence in the same manner as the collimated beam having a larger spot size.

These results are consistent with those obtained from the CARS measurement and thus confirm our earlier conclusion that focused beams are affected very little by turbulence in the media, whereas collimated beams--regardless of their beam size--are affected. This is a very significant conclusion for the application of CARS to combustion diagnostics because insensitivity of the focused laser beams to media turbulence would eliminate many problems and associated uncertainties in CARS measurements.

It is a generally accepted fact that the media turbulence manifests itself in two ways--beam wandering and beam spreading. In order to investigate the degree to which these occur in a turbulent medium, the following experiment was performed using the system shown schematically in Fig. 34. An expanded He-Ne laser beam was directed through the cold He-air jet, beam size being variable by means of an adjustable aperture. The beam was then focused onto a 2-D optical multichannel analyzer through a long-focal-length lens. For the measurement the laser beam was switched on for ~ 2 msec by means of an electro-optic shutter, and the beam profile was monitored on the optical-multichannel-analyzer display unit. In order to reduce the leakage light through the electro-optic switch during the "off" time, a mechanical shutter was also employed to limit the background exposure to ~ 5 msec.
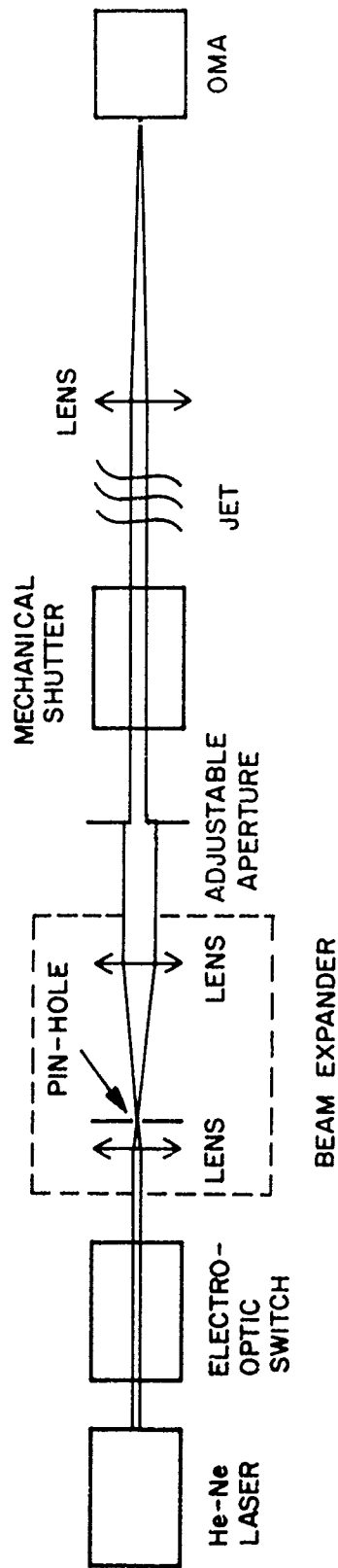
77

Figure 34. Schematic Diagram of an Experimental System for Studies of the Effect of Turbulence Upon Laser-Beam Propagation

Figure 35 is a series of laser-pulse photographs showing the beam profile taken on a random basis. The first picture was taken with the jet off, while the others were taken with the jet on. It can be seen clearly that the beam undergoes both spreading and displacement when media turbulence is present. However, quantitative measurements on the beam wandering and spreading were not possible because of the limited linearity of and the cross-talk between the optical-multichannel-analyzer elements coupled with the relatively small beam-spot size in the detector plane.

This proved to be an effective method of demonstrating these effects; however, since the results were only qualitative, alternative approaches must be sought to provide a more quantitative data-acquisition technique. Ultimately this technique will require the incorporation of a light switch or light source into the system which is sufficiently fast to permit a truly "frozen" picture of turbulent media which is believed to have a fluctuation frequency of ~ 10 kHz.

5. ROCKET-ENGINE-PLUME DIAGNOSTICS

As one of the first steps toward the eventual development of the CARS technique for diagnostics of practical combustors, a research rocket engine which operates on a kerosene-oxygen mixture was installed in a specially erected rocket chamber. This rocket engine was made available to the Air Force Aero Propulsion Laboratory for tests using the CARS technique by the Air Force Armament Laboratory where it was developed. The CARS system was moved to the rocket-engine site, and some preliminary measurements were made on the rocket-engine plume.

While the ultimate objectives of these studies were the practical application of the CARS technique to plume diagnostics, the immediate goal was the adaptation of the CARS system to the harsh environment surrounding the rocket engine in operation. Much-feared sonic noise was found to be at a relatively tolerable level of ~ 90 dBa in the immediate vicinity of the rocket chamber, and the vibration did not seem to have an adverse effect upon the CARS system. Figure 36 is a photograph of the rocket engine in operation, and a photograph of the CARS system probing the engine plume is shown in Fig. 37.

79
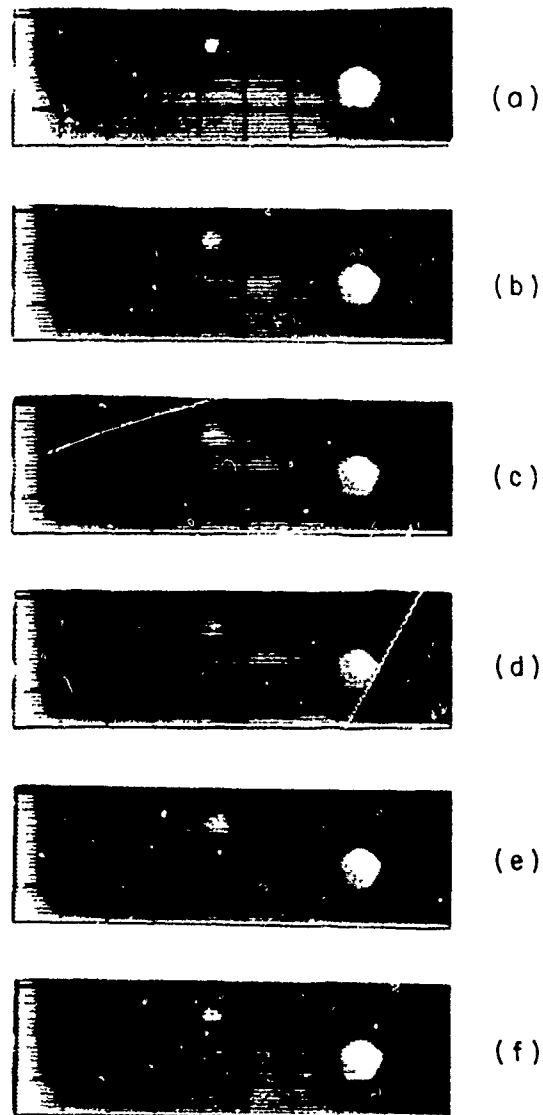
Figure 35. Photographs of Laser-Beam Profile Taken with the System Shown
in Fig. 34. (a) was taken with the jet off, and (b) through
(f) with the jet on. The turbulence-caused beam spread and
displacement are clearly visible. The pentagonal images on
the right-hand side were caused by exposure-control light
bulb in the camera and have no relation to this experiment.

Figure 36.   Photograph of Rocket Engine in Operation

Figure 37. Photograph of the CARS System Probing Rocket-Engine Plume

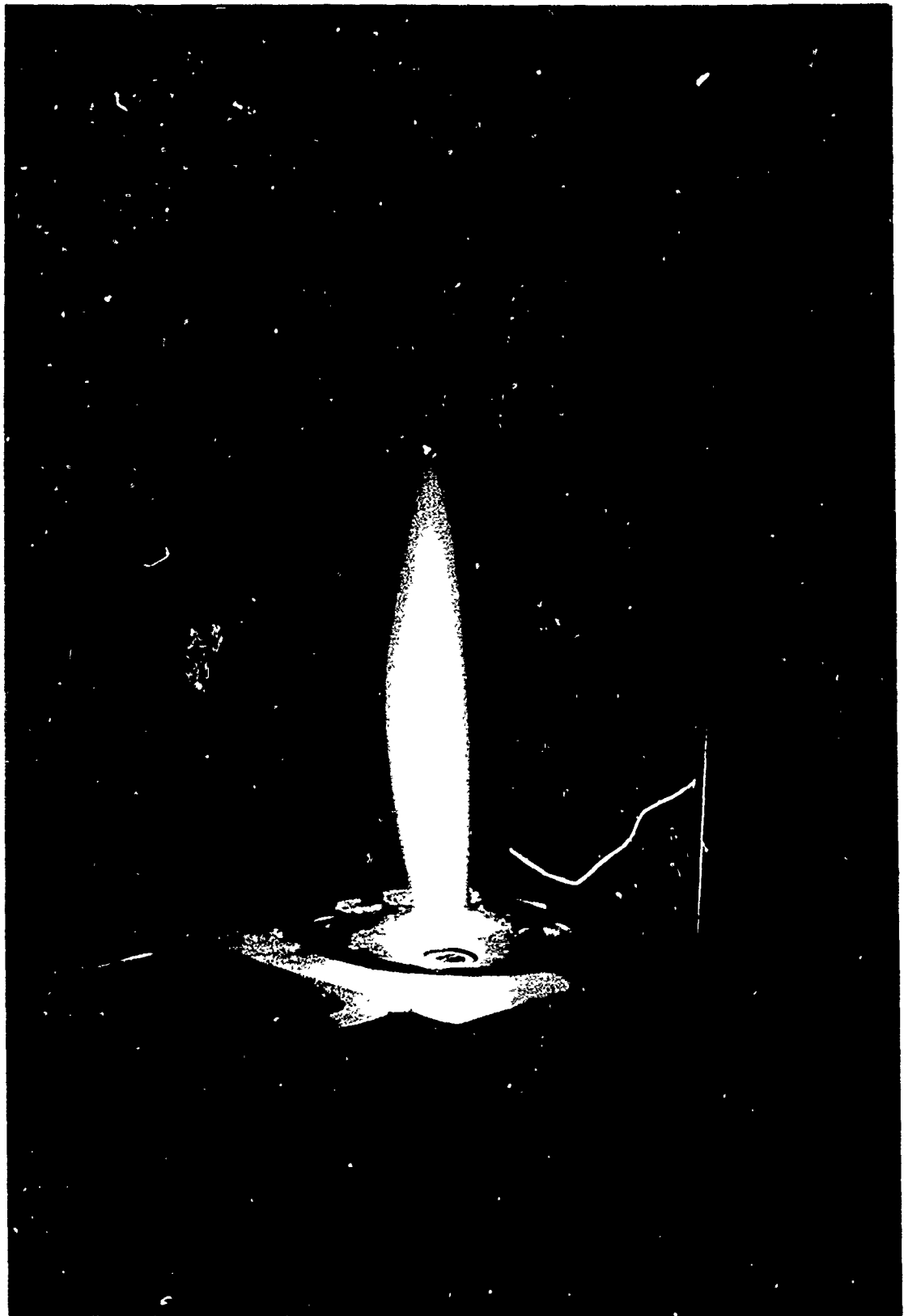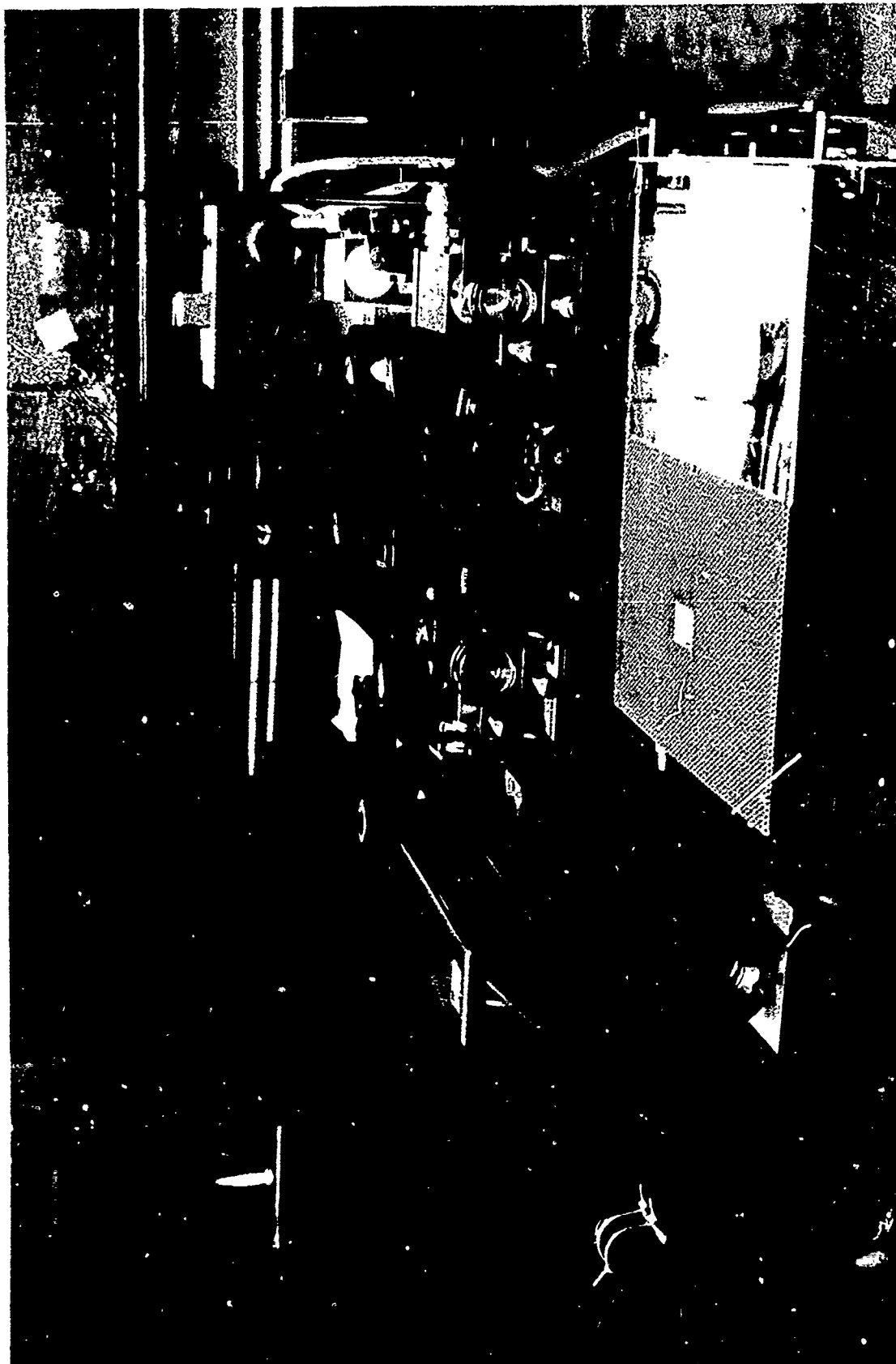One of the problems encountered during the preliminary measurement was the interference of the intense emission from the visible plume with the anti-Stokes signal. Because of this interference, the probing of the visible plume with the optical multichannel analyzer being used was practically impossible. It was believed that a gated optical multichannel analyzer might provide a solution to this problem. Problems in obtaining CARS spectra of hot N_2 in the plume involved the relatively low N_2 density in the plume and the overwhelming contribution of . ~~spheric (cold) N_2 surrounding the plume. The difficulties were removea ..t least in part by placing the focusing lens closer to the plume, thereby permitting the use of a shorter focal-length lens. In addition, the long-pass filter was moved to another location--just behind the focusing lens--to eliminate the contribution of atmospheric N_2 in the optical path prior to the filter.

The spectra recorded after these measures had been taken indicate the presence of hot N_2 as expected. Fig. 38 shows one set of such CARS spectra taken at the center of the rocket-engine plume, 4.5 in. above the nozzle. The bottom spectrum (d) was obtained from the N_2 in air before the rocket was fired up, and the lineshape represents the rotational structure of N_2 at room temperature. The other three spectra (a, b and c) were recorded while the rocket engine was operating and, thus, their line profile represents the rotational structure of N_2 at local plume temperature. It can be observed easily that the three spectra (a-c) have a broader profile than the last spectrum, indicating a higher level of rotational excitation in the plume.

In obtaining these spectra, the dye laser was tuned by means of an intra-cavity interference filter rather than dye-concentration adjustment because of the insufficient laser-power density obtainable with the latter method for signal detection with an optical multichannel analyzer. However, due to this procedure the etalon-like behavior of the interference filter (as described in Section III) could not be avoided, and as a result the analyses of spectra became hopelessly complicated. The effect of the etalon-like behavior upon the spectra was clearly demonstrated by the pronounced change observed in the spectral profile as the interference filter was

83
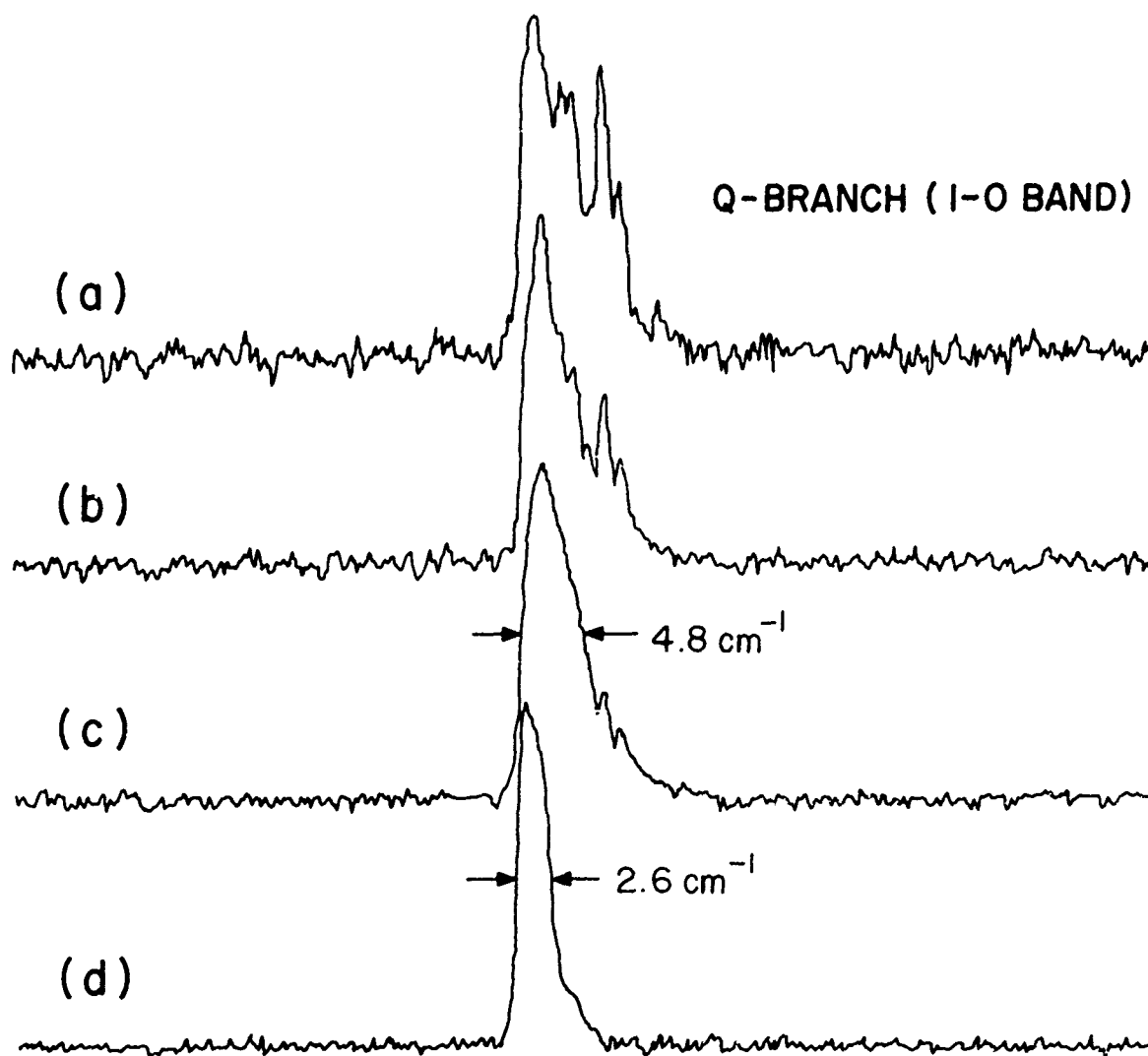
Figure 38. CARS Spectra of N_2. Spectra (a), (b), and (c) were obtained from the rocket plume, while spectrum (d) was taken from atmospheric N_2 at room temperature.

rotated in small steps. The first three spectra in Fig. 38 were obtained
in this manner, with the interference filter set at three slightly different
positions. Whenever one of the comb-structured laser lines coincided with
a rotational line, the particular rotational line exhibited an unusual
enhancement in intensity. An example of this can be seen in Fig. 38(a).

Because of the complicated structure of the exciting-dye-laser line,
it was not possible to obtain a quantitative measurement of the plume
temperature from these spectra in a simple manner. (In order to accomplish
this, a dye laser having a simple lineshape such as that obtainable from
a double-prism-tuned dye laser would be required.) Despite these irregu-
larities in the data, the Q-branch lines of anti-Stokes radiation from the
rocket-engine plume were recorded as a function of position. The results
as shown in Figs. 39 and 40 represent the lineshape profile for elevations
of 4 in. and 2 in., respectively, from the nozzle of the rocket engine.

Although the local temperature of the plume cannot be calculated
directly from the spectra for the reasons mentioned above, some qualitative
interpretations can be obtained from them. For instance, the increase in
linewidth due to higher rotational excitation within the plume is quite
obvious in both figures. In addition, it can further be observed that the
linewidth of the anti-Stokes radiation from the center of the plume (see
the lower inset spectrum in respective figures) is smaller for the measure-
ment made at the 2-in. elevation (4.2 cm^{-1}) than for that made at the 4-in.
level (4.8 cm^{-1}); however, the opposite should be the case because the
actual temperature is higher at the 2-in. level. This apparent contradiction
is the result of the interference of atmospheric N_2 in the immediate vicinity
of the plume. Since the plume diameter is smaller at the 2-in. level than
at the 4-in. level while the CARS interaction length is approximately of
the same order of magnitude as the plume diameter, the anti-Stokes signal
generated at the 2-in. level suffers more from the interference of
atmospheric (cold) N_2. This is a common problem with the major molecular
species in air--namely, N_2 and O_2--in a medium whose dimensions are
comparable to or smaller than the interaction length for the CARS process.
This also places an effective upper limit on the spatial resolution which
the CARS technique can be expected to yield in similar situations.

Figure 39. Profile of Lineshapes of N_2 Anti-Stokes Radiation as a Function of Horizontal Position at an Elevation of 4 in. from the Nozzle of the Rocket Engine. (Numbers in parentheses represent relative distance (inches) from an arbitrarily chosen point in the plume.)
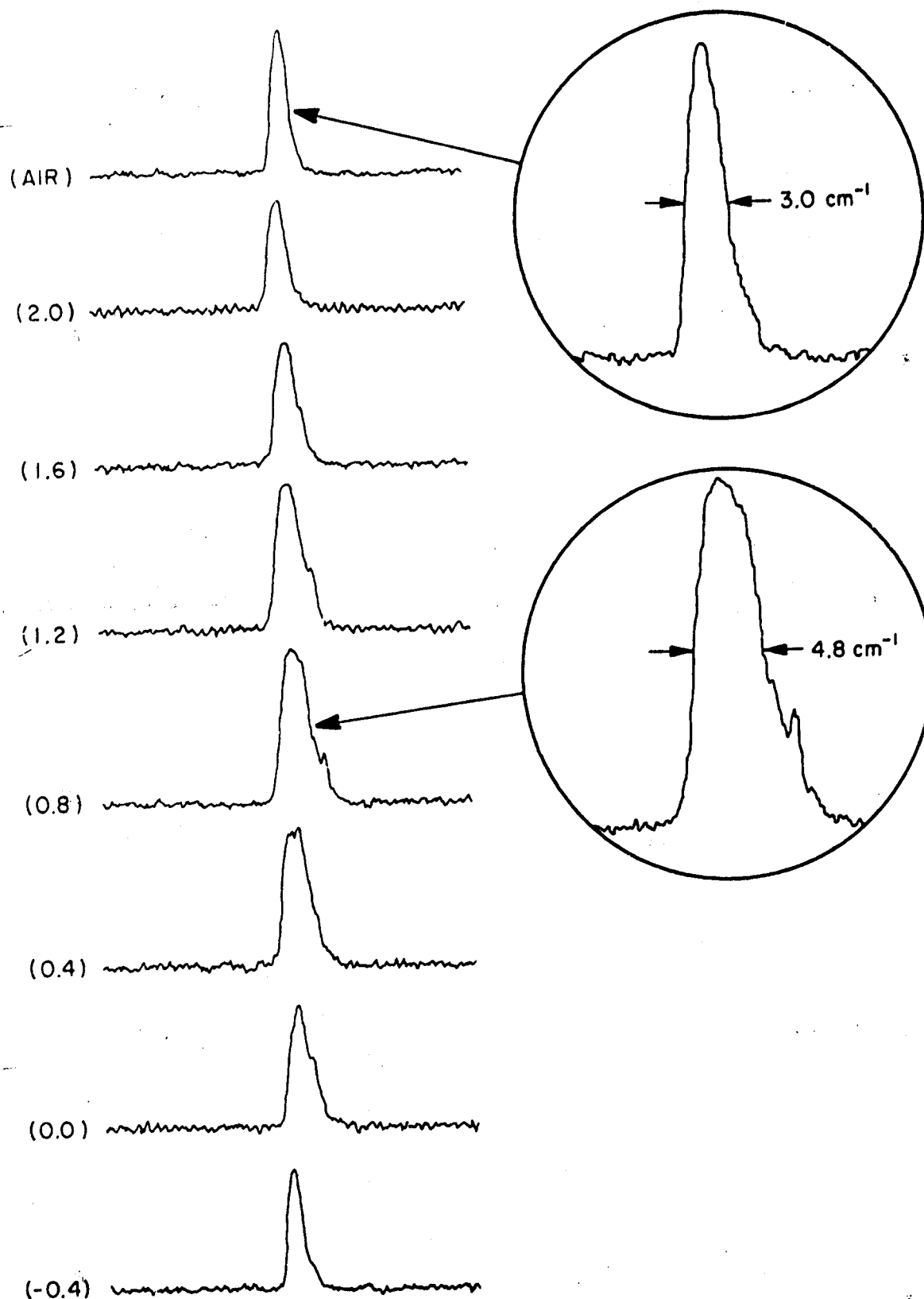
Figure 40.   Profile of Lineshapes of N_2 Anti-Stokes Radiation as a Function of Horizontal Position at an Elevation of 2 in. from the Nozzle of the Rocket Engine. (Numbers in parentheses represent relative distance (inches) from an arbitrarily chosen point in the plume.)
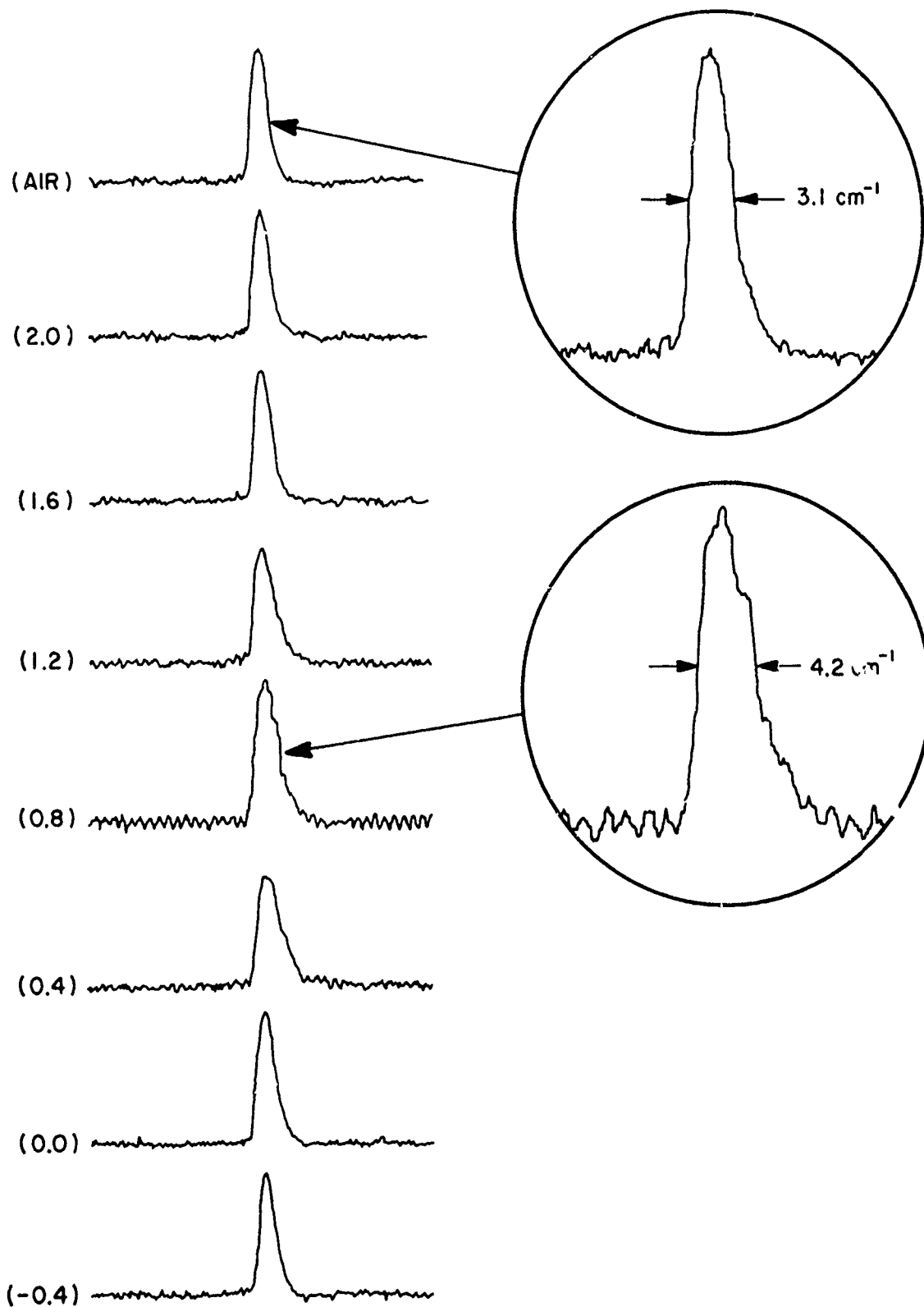
The N_2-concentration profile of the rocket plume was determined through CARS measurement of the integrated anti-Stokes intensity, scanning occurring across the plume at several elevations. The results are shown in Fig. 41. As long as the temperature dependence of Raman linewidth is ignored (although this is not a very safe practice), the intensity profile can be translated into that of relative concentrations in a straightforward manner. The employment of photomultipliers and transient recorders in the detection chain of the CARS system completely eliminated the signal interference of the background emission from the visible plume. Each point in the figure represents an average of eight measurements, and the two end points on each trace represent the measurements in static air just before and after rocket-engine operation lasting ~ 1.5 hr. It may be observed that a rather well-defined narrow dip in N_2 concentration just above the nozzle (top trace) becomes broader as the exhaust plume travels away from the nozzle, correctly indicating a diverging plume. Greater uncertainties in the measurement can also be observed in and near the plume as shown by error bars.

Although the results are reasonably good, they represent only an "apparent" N_2-concentration profile because the anti-Stokes intensity measurements also contain contributions from nitrogen gas outside the plume. This is the result of a large N_2 concentration in the immediate vicinity of the plume, despite the fact that the generation of the anti-Stokes radiation is weighted very heavily for the few-millimeters-long focal zone. Since the plume diameter is smallest at the tip of the nozzle of the rocket, the contribution of atmospheric nitrogen is greatest there. This accounts for the peak-to-valley ratio of anti-Stokes intensity appearing to be smallest here when, in fact, the opposite should be the case.

Efforts to detect the OH molecules in the plume were not very fruitful. For this experiment the dye laser was tuned by an interference filter only, and a spectral as well as a spatial scan within the plume was made. Moreover, a moderate increase in the fuel-oxygen ratio was made in order to enhance the OH concentration in the plume. Despite these measures, no conclusive resonant enhancement of the CARS signal could be observed as the dye laser was tuned through the Stokes region of the molecule. Further narrowing of the dye-laser line coupled with the use of a better laser dye for enhanced dye-laser output power might be sufficient to suppress the nonresonant contribution from other gases and bring out the resonant feature in the CARS spectrum.
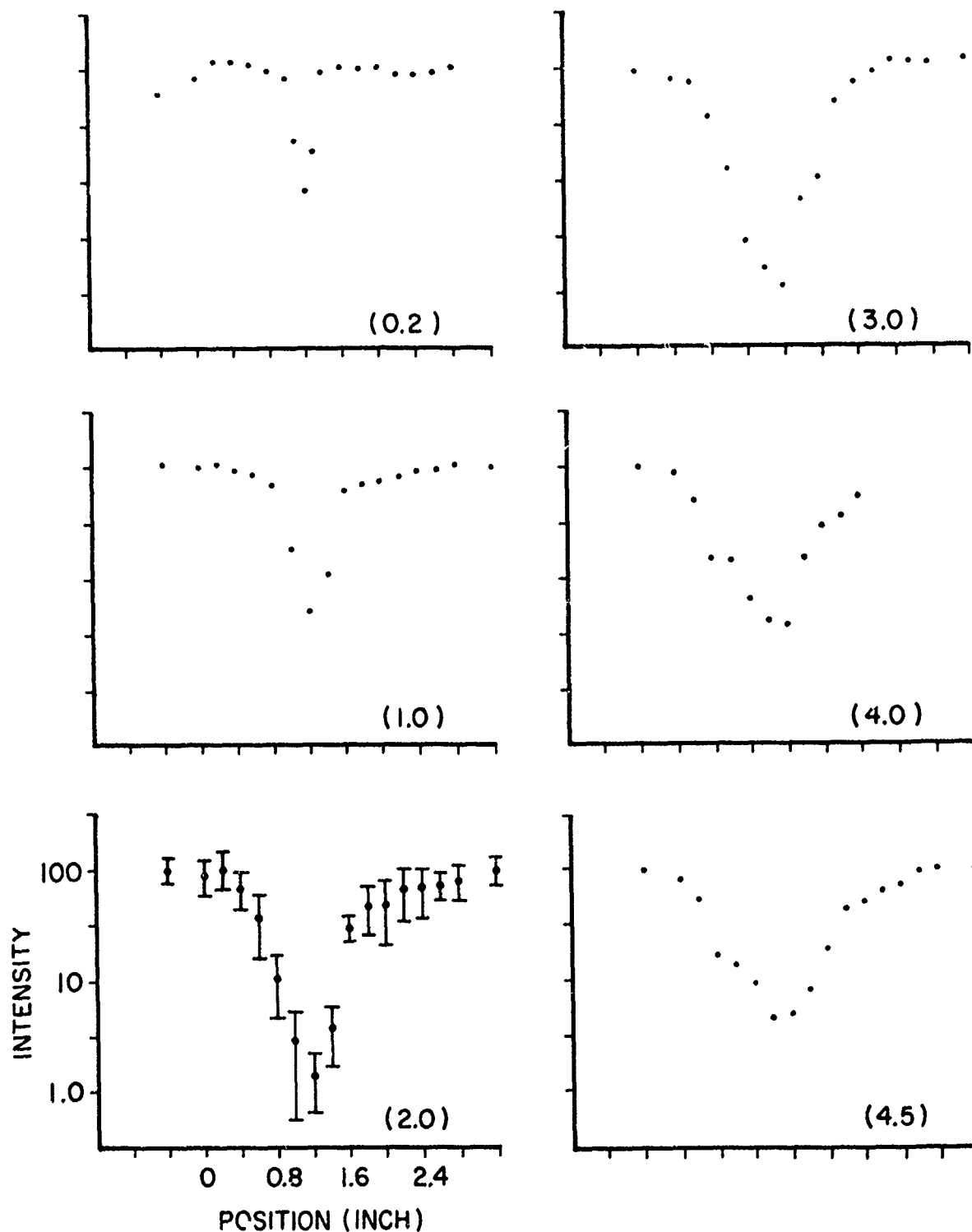
Figure 41. N_2-Concentration Profile as Determined Through CARS Measurement at Various Elevations in the Rocket-Engine Plume. Adjacent measurement points are spaced 0.2-in. apart, and the numbers in parentheses indicate the elevation from the rocket-nozzle where the measurements were made. (Error bars represent ± 1 standard deviation in measurement.)

SECTION V

CONCLUSIONS

In this report the development of an experimental CARS system has been described along with the results of theoretical and experimental investigations of the CARS of molecular gases. Although much work remains to be done on perfecting the CARS technique as a combustion-diagnostic tool, it has been amply demonstrated that the technique has great potential as an effective, real-time, remote diagnostic tool for combustion media.

The overall performance of the CARS system based upon a ruby laser and an infrared dye laser has been found to be reasonably good. However, the low pulse-repetition rate associated with the ruby laser and the rarity of efficient and stable infrared laser dyes are two of the most important shortcomings of such a system. Improvements on both fronts would be very desirable for practical diagnostic system development. The theory has been extended to describe broad-band excitation of the CARS process and integrated CARS intensity. This extension is directly applicable to the single-pulse CARS technique and its real-time measurement capability.

Results of the developmental effort on the experimental techniques to permit the application of the CARS process to real-time gas diagnostics such as the single-pulse CARS technique and the simultaneous detection of more than one gas species using a two-wavelength dye laser have been described.

Investigations on the pressure dependence of integrated CARS intensity have revealed that a critical functional relationship exists between the media pressure and intensity for each gas and that it is essential that this relationship be determined for all gases of interest.

Studies on the effects of media turbulence upon laser-beam propagation and the CARS process have shown that the turbulence effect is quite severe for beam propagation and CARS in the case of collimated beams but that it is minimal in the case of focused beams.

Important subjects not investigated during this program include
techniques of reducing nonresonant background signal, the effect of
media saturation, the effect of the Doppler broadening, the temperature
dependence of the linewidth, and electronic-resonance enhancement of the
CARS process. Research in these and related areas will be extremely
valuable to the understanding of the basic processes involved and to
efforts on the development of this technique into a practical combustion
diagnostic tool.

APPENDIX A

CIRCUIT DIAGRAMS FOR ELECTRONIC ACCESSORIES
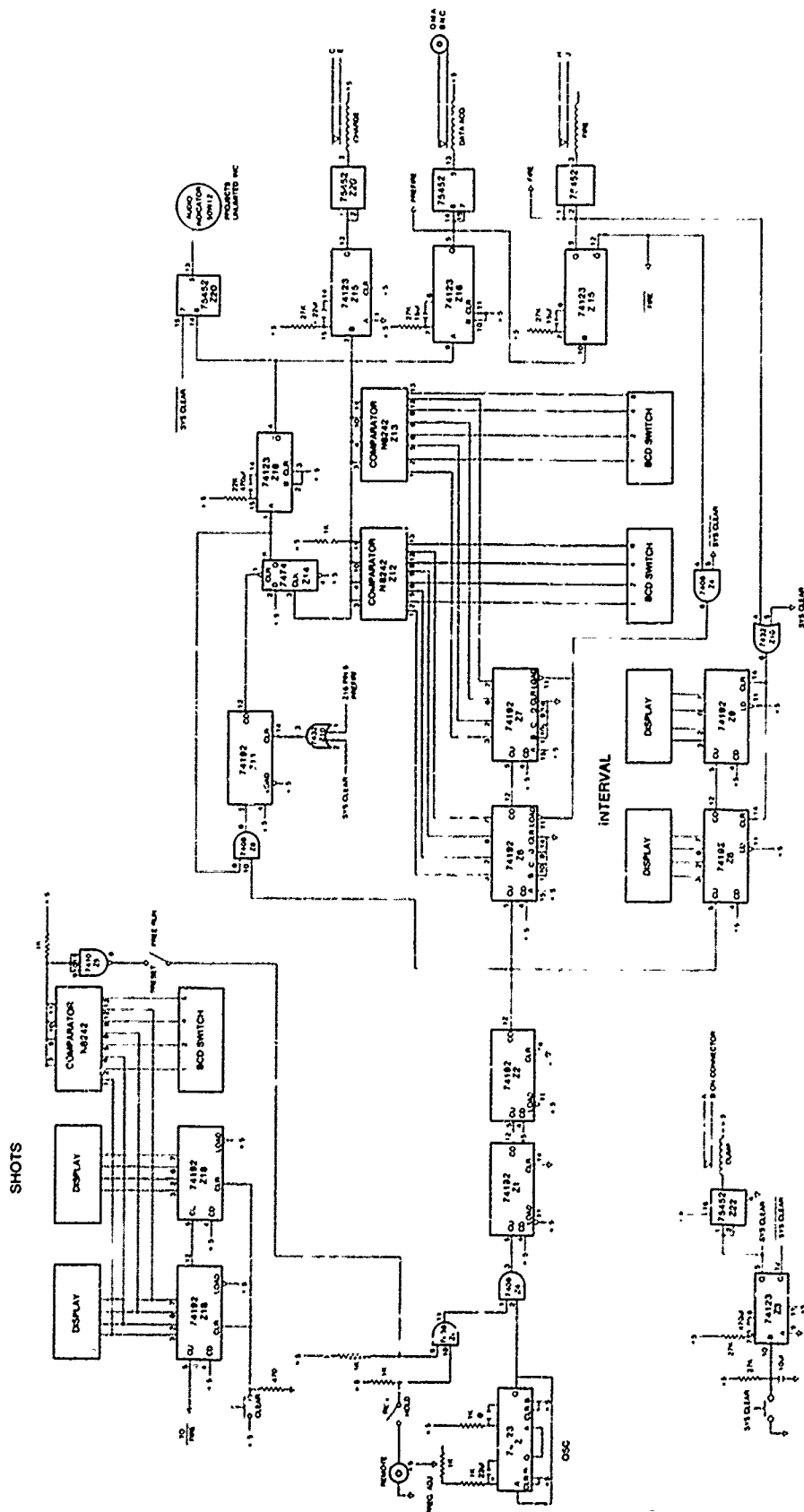DEVELOPED FOR THE CARS SYSTEM

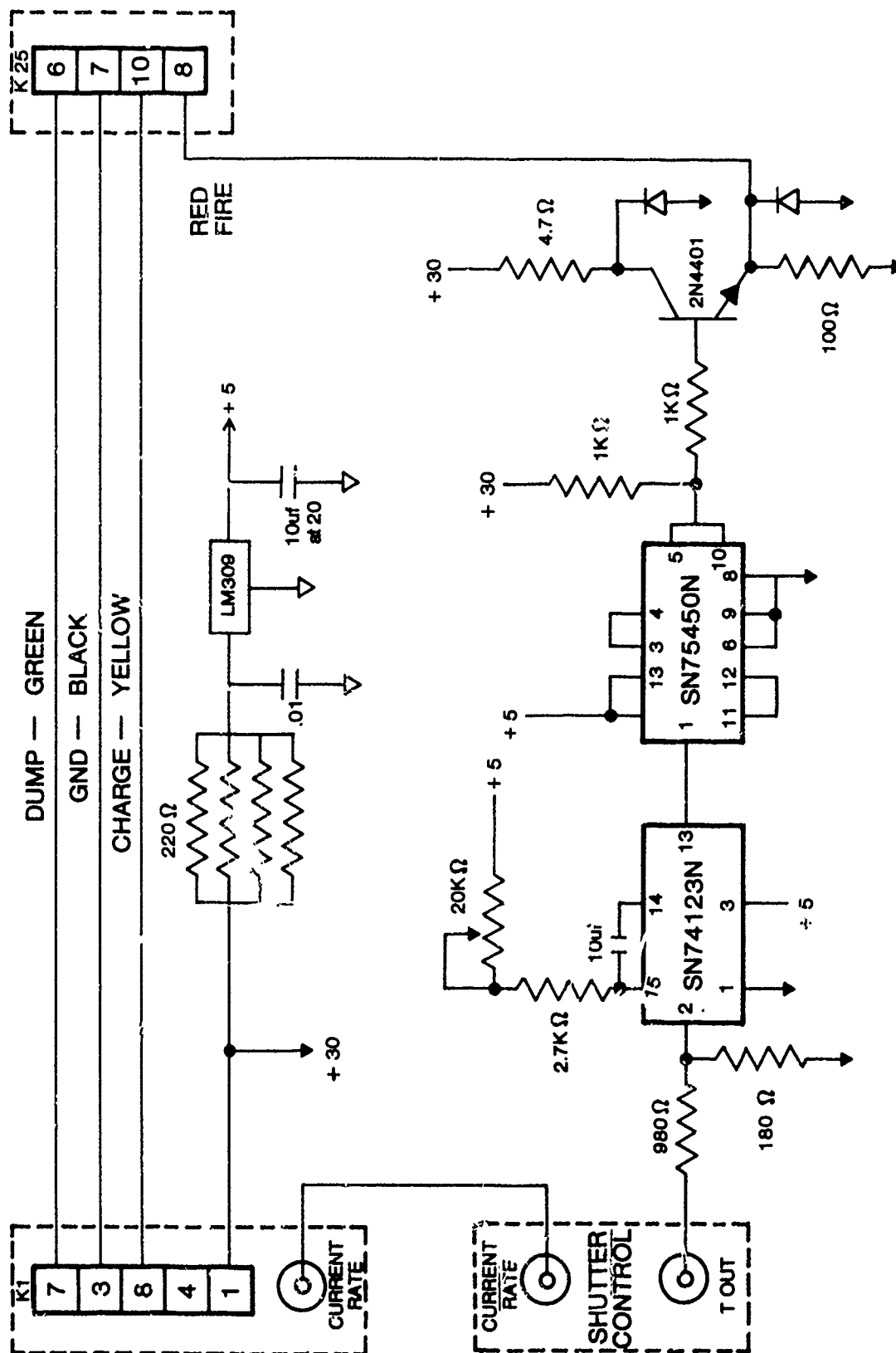Figure A-1. Circuit Diagram for Automatic Laser-Fire Control Unit

94

Figure A-2. Circuit Diagram for the Buffer Network Between Korad K-25 Laser Power Supply and Korad Shutter Control Unit

APPENDIX B

SAMPLE CALCULATION OF DIFFUSION TIME

APPENDIX B

SAMPLE CALCULATION OF DIFFUSION TIME

Let us assume an idealized situation in which a component gas is filled to 30 atm of pressure and another component gas is introduced into the mixing chamber to 60 atm from the nozzle that extends to the center of the chamber; now, the time required for the two component gases to diffuse into each other can be calculated. Let us further assume that the second gas introduced displaces the first gas at the central portion of the chamber, as indicated by line ① in the figure below. The solution of a diffusion equation,

$$\frac{\partial c}{\partial t} = D \frac{\partial^2 c}{\partial x^2} \quad , \tag{B1}$$

having the initial and boundary conditions shown in the figure, is given by

$$c(x,t) = \frac{c_o}{2} \left[erf\left(\frac{x_o + x}{2\sqrt{Dt}}\right) - erf\left(\frac{x_o - x}{2\sqrt{Dt}}\right) \right]$$

$$+ \frac{c_o}{2} \left[erf\left(\frac{x_o + 2\ell - x}{2\sqrt{Dt}}\right) - erf\left(\frac{x_o - 2\ell + x}{2\sqrt{Dt}}\right) \right] \tag{B2}$$

+ other reflection terms,

98
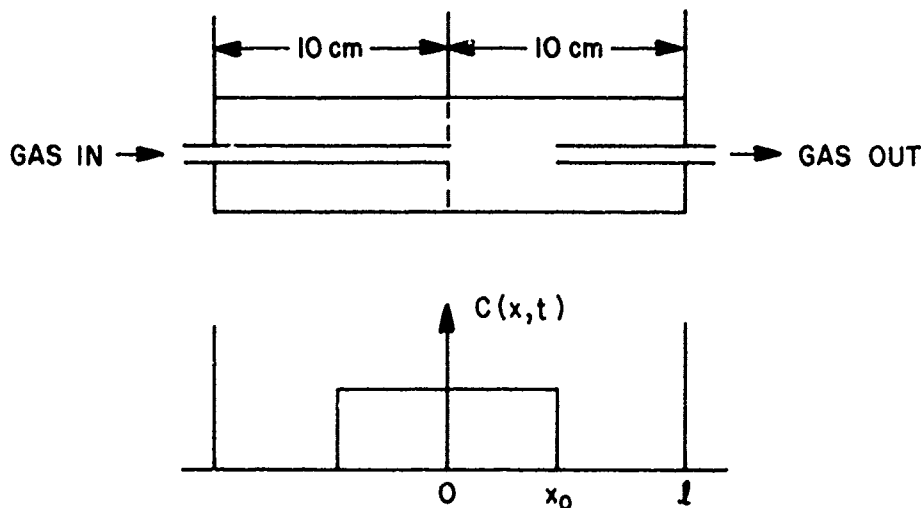
where c is the concentration of the diffusing gas,

  c_0 is the initial concentration of the diffusing gas,

  x is the distance as measured from the center of the chamber,

  t is the time from the moment the diffusion process begins, and

  D is the diffusion coefficient for the pair of gases under consideration.

The reflection terms are the terms in the top line of the equation, with x replaced by $2\ell - x$ and $2\ell + x$ for the first and second reflections, respectively. In the case of the example considered here, the inclusion of the first two or three reflections turns out to be sufficiently accurate for the time frame of interest.

A simpler solution can be obtained by solving the diffusion equation by a "separation of variables" technique. It can be shown that the solution is given by

$$c(x,t) = \frac{c_0}{2}\left[1 + \frac{4}{\pi}\sum_{n=0}^{\infty}\frac{(-1)^n}{(2n+1)}\cos\frac{(2n+1)\pi}{\ell}x \cdot \right.$$

(B3)

$$\left. \exp\left(-\frac{(2n+1)^2\pi^2 D}{\ell^2}t\right)\right]$$

For a large t, at $x = \ell$,

$$c(\ell,t) \approx \frac{c_0}{2}\left[1 - \frac{4}{\pi}\exp\left(-\frac{\pi^2 D}{\ell^2}t\right)\right]$$

(B4)

The diffusion coefficient depends upon temperature and pressure in the following manner:

$$D \propto \frac{T^\alpha}{P}$$

(B5)

where T and P are the temperature and pressure of the gases, respectively, and α is a constant which depends upon the component gases ($\alpha = 1.75$ or 2.0). The table[*] below gives the values of D and α for some combinations of gases under standard conditions (273°K and 760 mm Hg).

Gases	D (cm^2/sec)	α
H_2-N_2	0.674	1.75
He-Ar	0.641	1.75
O_2-N_2	0.181	1.75

*[*]AIP Handbook (3rd ed.)(American Institute of Physics, NY, NY, 1972), pp. 2-250.

Solving for t after setting $c(\ell,t)$ equal to $0.95\ c(\ell,\infty)$ yields the time required to reach 95% uniformity in the gas mixture. In the case of hydrogen and nitrogen, this time was found to be approximately 45 minutes, which is also consistent with the results obtained from Eq. (B2).

The time requirement seems unreasonably long according to these simplistic calculations; however, it should be remembered that in practice it would be much shorter because several important facts have been neglected in this simple model, all of which would help to reduce the diffusion time. These are (1) the neglect of initial velocity of the diffusing gas in the chamber, (2) an idealized initial distribution of the gases, and (3) the fact that the transfer point of the gas mixture is not at the end of the mixing chamber where uniformity of gas concentration is expected to be the worst.

APPENDIX C

OPERATIONAL INSTRUCTIONS FOR VACUUM/GAS-HANDLING SYSTEM

APPENDIX C

OPERATIONAL INSTRUCTIONS FOR VACUUM/GAS-HANDLING SYSTEM

The system should be evacuated prior to any gas-filling procedure.

1. Pumping Procedure

   Open all valves in the system with the exception of vents V5 and V8 which must remain closed. After the system has reached the desired vacuum, all valves must be closed. The system is now ready for filling.

2. Mixing Procedure

   The mixing cell may be filled with any combination of up to four gases by opening V1- V4. The pressure in the mixing cell can be monitored by observing the 0-1000 PSIG gauge labeled mixing cylinder which is located directly above the control panel. When the desired pressure has been reached in the mixing cell, valves used to admit the gases into the mixing cell must be closed. The gases in the mixing cell must then be allowed to diffuse into each other for at least 1 hr in order to achieve a uniform mixture. If only one gas is involved, this diffusion time is not required and one can proceed directly to fill any or all of the cells from the mixing cell according to the instructions outlined below.

3. Filling High-Pressure Cell

   Close V10 and open V9--this permits the operator to observe the pressure during the filling of the cell. The gauge that measures the pressure is labeled high pressure or reference cell and is located directly above the control panel. Open V6 and fill the high-pressure cell to the desired value. After filling, close V6.

4. Filling Sample Cell

   Open V11 and V13. The regulator R1 has been preset and locked in a position that will supply 4 PSIG to V12. This is done to protect the capacitance-manometer head which is rated at 1000 torr maximum. Slowly open V12 which is a micrometer metering valve. Fill the cell to the desired pressure. This pressure is measured in torr and is displayed on the digital readout in the upper-left corner of the equipment rack. After filling the cell to the desired pressure, close V11- V13.

   Depending upon the pressure of the sample cell, either head (1000 Torr or 10 Torr) of the capacitance manometer can be used by the head selector (C2) for monitoring the exact pressure.

5. Filling Reference Cell

    (a) To fill the reference cell to a high pressure, close V9 and
open V10. This enables the operator to observe the pressure during filling.
Open V7 and fill to the desired pressure. After filling, close V7.

    (b) To fill the reference cell to a low pressure, install the handle
on V15. This is located in a plastic bag on the side of the equipment rack.
Make a positive check to insure that both V7 and V10 are closed and that
the reference cell is not under high pressure. After these precautions
have been taken, open V15 and proceed to fill the reference cell in the
same manner as that described for the sample cell. When filling is com-
plete, close V15 and remove the handle and replace in the plastic bag.

<u>CAUTION</u>

Failure on the part of the operator to follow instructions relative to
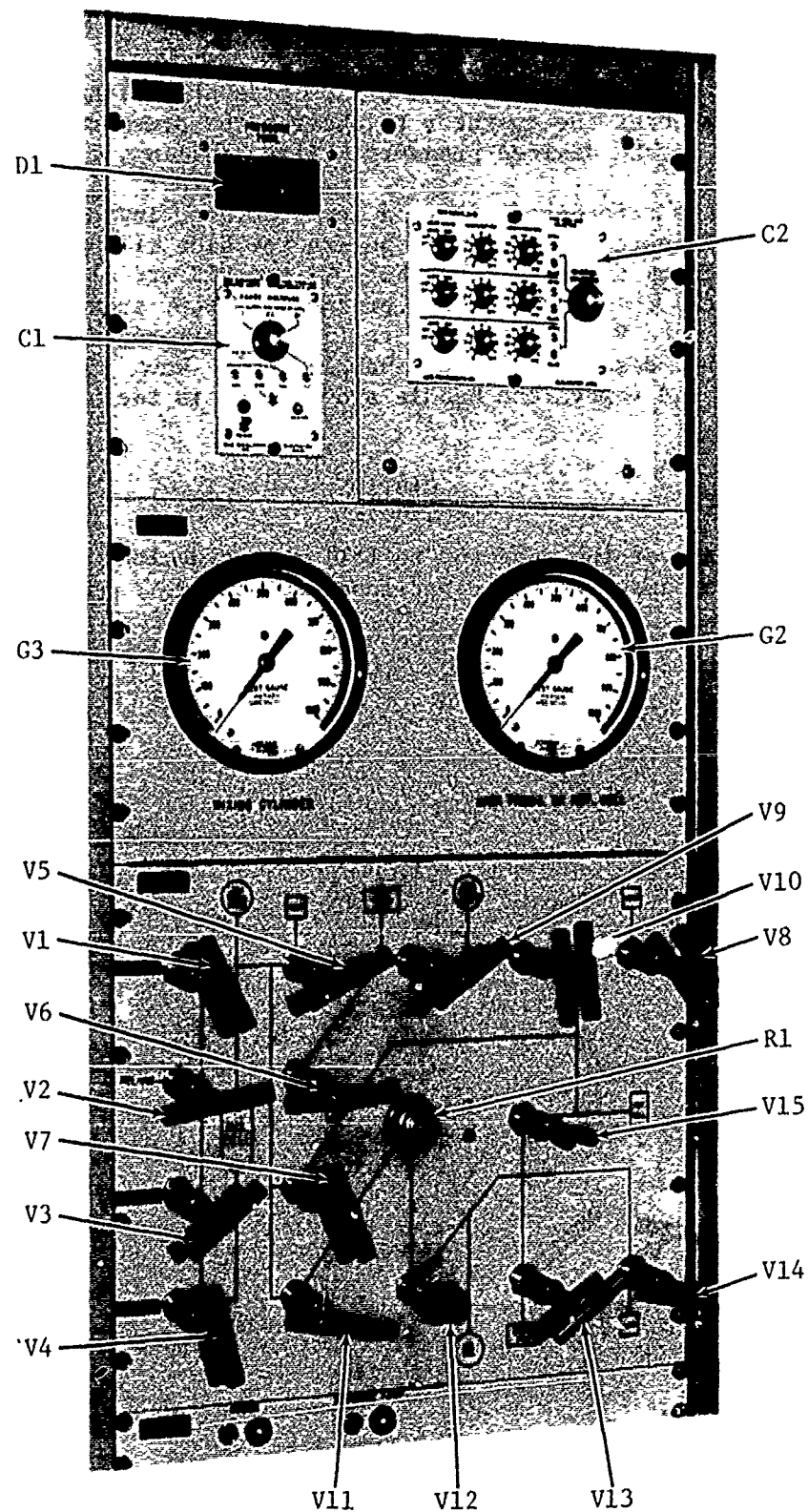<u>V15</u> may result in damage to the capacitance manometer.

Figure C-1.   Front View of Vacuum/Gas-Handling System Control Rack.
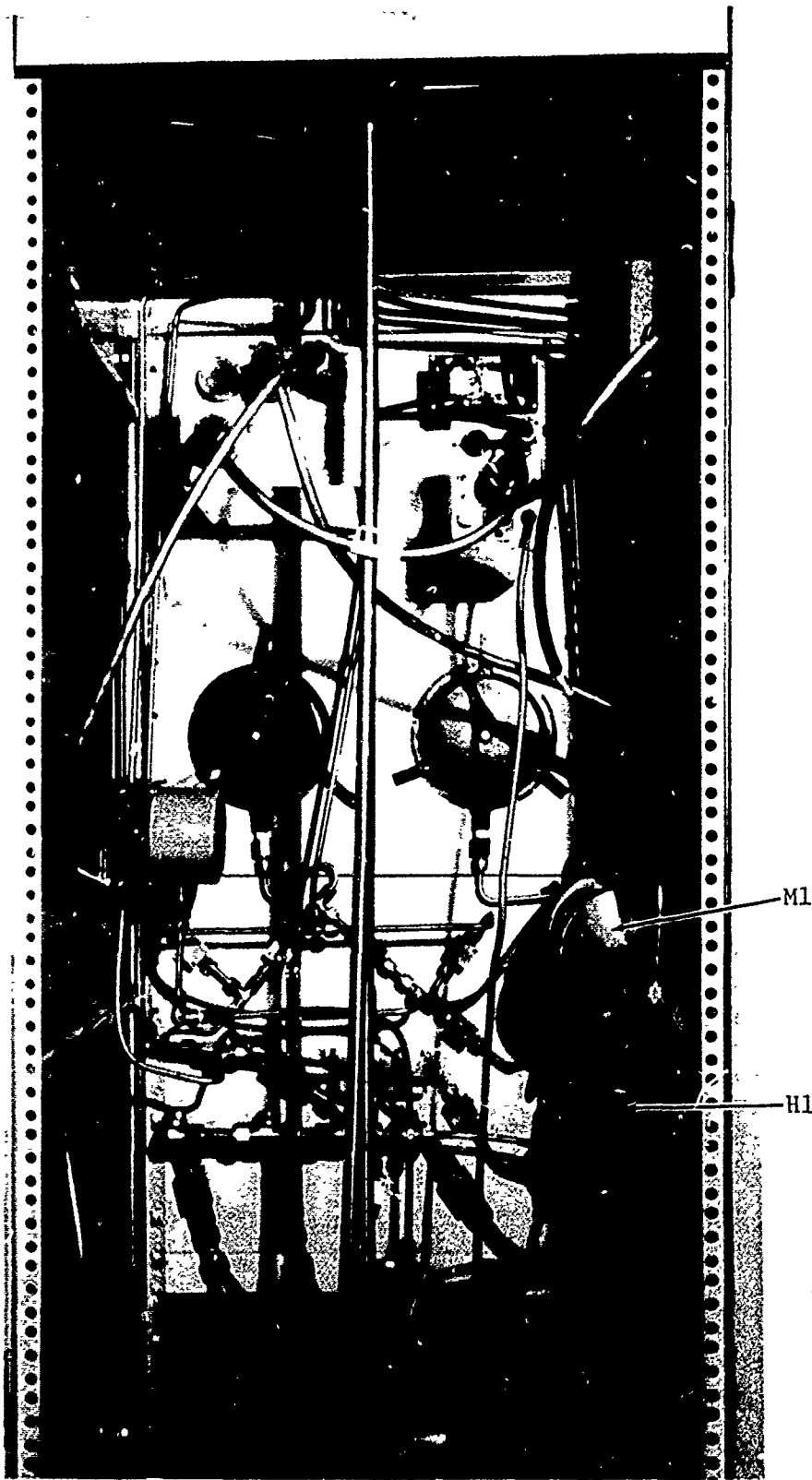
Figure C-2. Rear View of Vacuum/Gas-Handling System Control Rack

PARTS LIST

Ref	Manufacturer	Part Number	Description
V1	NUPRO	SS-4TG	1/4-in. Bellows Valve
V2	"	"	"
V3	"	"	"
V4	"	"	"
V5	"	"	"
V6	"	SS-4TRG	1/4-in. Bellows Regulating Stem Valve
V7	"	"	"
V8	"	SS-4TG	1/4-in. Bellows Valve
V9	"	"	"
V10	"	"	"
V11	"	SS-8TG	1/2-in. Bellows Valve
V12	"	SS-4BMG	1/4-in. Bellows Metering Valve
V13	"	SS-8TG	1/2-in. Bellows Valve
V14	"	"	"
V15	"	"	"
R1	MATHESON	3500	4-75 PSIG Regulator
C2	MKS INSTRUM.	170M-36B	Capacitance Manometer Head Selector
G2	MATHESON	63-5613	0-1000 PSIG Pressure Gauge
G3	"	"	"
C1	MKS INSTRUM.	170M-6A	Control Unit - Capacitance Manometer
D1	NEWPORT	200 AS	Display Unit - Capacitance Manometer
H1	MKS INSTRUM.	315-AHS-1000	0-1000 torr Capacitance Manometer Head
M1	WHITEY	304-HDF4-1000	1000 cc Mixing Cylinder

REFERENCES

1. R. W. Minck, R. W. Terhune, and W. G. Rado, Appl. Phys. Lett. $\underline{3}$, 181 (1963).

2. P. D. Maker and R. W. Terhune, Phys. Rev. $\underline{137}$, A801 (1965).

3. W. G. Rado, Appl. Phys. Lett. $\underline{11}$, 123 (1967).

4. P. R. Regnier and J. F. E. Taran, Appl. Phys. Lett. $\underline{23}$, 240 (1973).

5. P. R. Regnier and J. P. E. Taran, in Laser Raman Gas Diagnostics (M. Lapp and C. M. Penney, eds.)(Plenum Press, New York, 1974).

6. F. Moya, S. A. J. Druet, and J. P. E. Taran, Optics Comm. $\underline{13}$, 169 (1975).

7. F. Moya, S. Druet, M. Pealat, and J. P. E. Taran, AIAA Paper 76-29, Presented at 14th Annual AIAA Conference on Aerospace Science, Washington, D.C., 26-28 January 1976.

8. J. W. Nibler, J. R. McDonald, and A. B. Harvey, Optics Comm. $\underline{18}$, 371 (1976).

9. J. J. Barrett and R. F. Begley, Appl. Phys. Lett. $\underline{27}$, 129 (1975).

10. J. J. Barret, Appl. Phys. Lett. $\underline{29}$, 722 (1976).

11. R. B. Miles, G. Laufer, and G. C. Bjorklund, Appl. Phys. Lett. $\underline{30}$, 417 (1977).

12. A. B. Harvey, J. R. McDonald, and W. M. Tolles, Progress in Analytical Chemistry (Plenum Press, New York, in press).

13. J. J. Song, G. L. Easley, and M. D. Levenson, Appl. Phys. Lett. $\underline{29}$, 567 (1976).

14. R. T. Lynch, Jr., S. D. Kramer, H. Lotem, and N. Bloembergen, Optics Comm. $\underline{16}$, 372 (1976).

15. H. Lotem, R. T. Lynch, Jr., and N. Bloembergen, Phys. Rev. A $\underline{14}$, 1748 (1976).

16. P. Regnier, Application of Coherent Anti-Stokes Raman Scattering to the Measurement of Gas Concentration and Flow Visualization, Technical Report No. 215, Office National D'etudes et de Recherches Aerospatiales, 92320 Chatillon, France.

17. R. N. DeWitt, A. B. Harvey, and W. M. Tolles, Theoretical Development of Third-Order Susceptibility as Related to Coherent Anti-Stokes Raman Spectroscopy, NRL Memorandum No. 3260 (Naval Research Laboratory, Washington, D. C., 1976).

18. P. N. Butcher, <u>Nonlinear Optical Phenomena</u>, Engineering Experiment Station Bulletin 200, The Ohio State University, Columbus, Ohio (1965).

19. G. Placzek, <u>The Rayleigh and Raman Scattering</u>, UCRL-TRANS-526(L), University of California, Livermore, California (1959).

20. J. A. Giordmaine and W. Kaiser, Phys. Rev. <u>144</u>, 676 (1966).

21. M. Maier, W. Kaiser, and J. A. Giordmaine, Phys. Rev. <u>177</u>, 580 (1969).

22. Y. Miyazoe and M. Maeda, Appl. Phys. Lett. <u>12</u>, 206 (1968).

23. P. E. Oettinger and C. F. Dewey, Jr., IEEE J. Quant. Electr. <u>12</u>, 95 (1976).

24. J. P. Webb, F. G. Webster, and B. E. Plourde, IEEE J. Quant. Electr. <u>11</u>, 114 (1975); Kodak Organic Chemical Bull. <u>46</u>, 3 (1974).

25. P. Lallemand and P. Simova, J. Mol. Spectry <u>26</u>, 262 (1968).

26. R. H. Dicke, Phys. Rev. <u>89</u>, 472 (1953).

27. F. DeMartini, G. P. Guiliani, and E. Santamato, Optics Comm. <u>5</u>, 126 (1972).

28. L. Galatry, Phys. Rev. <u>122</u>, 1218 (1961).

29. P. Lallemand, P. Simova, and G. Bret, Phys. Rev. Lett. <u>17</u>, 1239 (1966).

30. H. S. Pilloff, U. S. Patent 3,857,109 (1974).